The Study of Astronomical Transients in the Infrared

by

Robert Strausbaugh

A Dissertation Presented in Partial Fulfillment
of the Requirements for the Degree
Doctor of Philosophy

Approved May 2019 by the
Graduate Supervisory Committee:

Nathaniel Butler, Chair
Rolf Jansen
Phillip Mauskopf
Rogier Windhorst

ARIZONA STATE UNIVERSITY

August 2019

ABSTRACT

Several key, open questions in astrophysics can be tackled by searching for and mining large datasets for transient phenomena. The evolution of massive stars and compact objects can be studied over cosmic time by identifying supernovae (SNe) and gamma-ray bursts (GRBs) in other galaxies and determining their redshifts. Modeling GRBs and their afterglows to probe the jets of GRBs can shed light on the emission mechanism, rate, and energetics of these events.

In Chapter 1, I discuss the current state of astronomical transient study, including sources of interest, instrumentation, and data reduction techniques, with a focus on work in the infrared. In Chapter 2, I present original, work published in the Proceedings of the Astronomical Society of the Pacific, testing InGaAs infrared detectors for astronomical use (Strausbaugh, Jackson, and Butler 2018); highlights of this work include observing the exoplanet transit of HD189773B, and detecting the nearby supernova SN2016adj with an InGaAs detector mounted on a small telescope at ASU. In Chapter 3, I discuss my work on GRB jets published in the Astrophysical Journal Letters, highlighting the interesting case of GRB 160625B (Strausbaugh et al. 2019), where I interpret a late-time bump in the GRB afterglow lightcurve as evidence for a bright-edged jet. In Chapter 4, I present a look back at previous years of RATIR (Re-ionization And Transient Infra-Red Camera) data, with an emphasis on the efficiency of following up GRBs detected by the *Fermi* Space Telescope, before some final remarks and brief discussion of future work in Chapter 5.

DEDICATION

To everyone who has a passion for science, keep going until you fail, and then pick yourself up and go at it again. You never know how far you'll go.

ACKNOWLEDGMENTS

I would like to thank my mom and dad, as without their support and encouragement, I wouldn't be where I am today. My heartfelt appreciation goes to Natalya, who has been my girlfriend, fiancée, and wife during the ups and downs of my PhD, and who has helped me not lose sight of the world outside of physics.

I couldn't have completed my research without the tremendous contributions by my advisor, Dr. Nat Butler; he has given me invaluable guidance and a platform to succeed. The efforts of my fellow grad students, Becky Jackson, Ian Chute, and Zach Golkhou have also been crucial in the completion of this dissertation. Becky, Ian, and I have spent countless hours over too many nights on the roof of PSF trying to get telescopes to work so that we could collect data.

A special mention is reserved for Glenn Randall and Andrew Shevchuk (aka Charlie) who I wouldn't have met were it not for grad school, and who have become some of my best friends. To other mentors, Dr. Zaniewski, and friends, Francis Duplessis, Cole Mathis, Ryan Brosch, Mark Wirth, Alyssa Adams, Varda Faghir, and others I may have missed, you all made my time at ASU worthwhile, and I am a better person for having known you. I would also like to thank my soccer friends, who gave me a physical outlet for all the frustrations that can come from grad school.

TABLE OF CONTENTS

CHAPTER Page

APPENDIX Page

LIST OF TABLES

Table Page

LIST OF FIGURES

Figure Page

Chapter 1

INTRODUCTION

Transient phenomena offer unique ways to study topics ranging from planetary formation, to the life cycles of stars, and beyond, to the evolution of the universe. As the natural end to the life cycle of massive stars, supernovae (SNe) and gamma-ray bursts (GRBs) can tell us about stellar evolution, and the progenitors of these events. Observing and modeling GRBs and their afterglows can shed light on the emission mechanism, rate, and energetics of these events. Transient phenomena are set to become even more important with recent detection of gravitational waves. Different transient phenomena can be used as a confirmation for the progenitor of gravitational waves; each of supernovae, GRBs, or kilonovae can be useful in this respect. In the realm of planetary science, exoplanet transits are an interesting transient phenomenon with unique insights into stellar and planetary system formation, and offer an avenue towards finding the signs of life on other planets. Studying transient sources in the infrared (IR) offers unique advantages over other wavelengths.

In this introduction I will discuss various transient phenomena, including GRBs, SNe, kilonovae, and exoplanet transits, particularly focusing on those sources that will appear in later chapters. I will then describe the instrumentation used to study these phenomena, in particular the Re-ionization and Transients InfraRed camera (RATIR) and several small telescopes at ASU. An emphasis will be placed on the benefits of studying transient phenomena in the IR and the challenges in instrumentation working in this regime. Finally, I will discuss current and future data analysis software and techniques that are used to identify and study transient sources.

1.1 Transient Phenomena

While on the main sequence, a star's brightness remains fairly constant for the majority of its life. A sudden or periodic change in brightness is indicative of interesting physics. These changes could be intrinsic to the star itself, or caused by its environment (extrinsic).

Intrinsic changes to a star can happen naturally due to its life cycle. The violent deaths of massive stars result in some of the biggest explosions in the universe. These explosions can be detected as supernovae and/or GRBs depending on the orientation of the observer and the source.

Certain variable stars exhibit changes in brightness throughout their life cycles. As stars age, outer layers of the stellar atmosphere can expelled from the star. These stars can then pulsate, due to changes in the opacity of different layers, or due to the radius of the star expanding and contracting.

Companions in a binary system can be responsible for novae, supernovae, and GRBs as an example of extrinsic transients. Type Ia supernovae, used as standard candles in cosmology, are caused by accretion from a companion star onto a white dwarf. Short duration GRBs can be generated by the collision of two dense objects, such as binary neutron stars, or neutron star-black hole pair. These compact object mergers (COMs) are interesting for their generation of gravitational waves, in addition to the electromagnetic signal from a GRB.

Another example of extrinsic transient phenomena caused by a companion is an exoplanet transit. With the correct geometric orientation, an exoplanet can pass in front of its host star. With the exoplanet between its host star and the Earth, the brightness of the star will decrease, by an amount proportional to the ratio of the star's surface area to the planet's surface area.

Transient phenomena can shed light on important open questions in physics. As the natural end to the life cycle of massive stars, SNe and GRBs can tell us about stellar evolution, and the progenitors of these events (e.g., Hirschi, Meynet, and Maeder 2005). Studying SNe and GRBs can help in determining what type of galaxies their progenitors are located in (Sullivan et al. 2010; Perley et al. 2016; Berger 2009) and at what redshifts (e.g., Le and Mehta 2017). GRBs provide information about their host galaxies and the environments of the interstellar and intergalactic mediums (e.g., Chen, Prochaska, and Bloom 2006). We can detect GRBs at high red-shifts due to their intrinsic brightness, making them useful probes of the early universe (Paradijs et al. 1997), especially the epoch of re-ionization (e.g., Ghirlanda, Ghisellini, and Firmani 2006). Transient phenomena are also important as possible electromagnetic counterparts to gravitational waves (e.g., Abbott and al. 2017).

1.1.1 Gamma-ray Bursts

Gamma-ray bursts (GRBs) are the most violent and energetic explosions in the universe, characterized by the large amount of gamma ray radiation produced. Due to their high energies, GRBs are some of the most distant objects detected in the universe, can be used to study the first generation of stars, and probe the epoch of re-ionization.

GRBs were initially discovered by Klebesadel, Strong, and Olson 1973, who stumbled upon them while using satellites to ensure countries were complying with a nuclear weapons testing ban. Much later, they were determined to be of cosmological origin after the discovery of their afterglows (e.g., Paradijs et al. 1997; Gehrels et al. 2005).

GRBs were first divided into two categories based on the duration of the emission of gamma-rays (prompt emission), as shown in Figure 1: short bursts, where the prompt emission lasts less than two seconds, and long bursts, lasting more than two seconds (e.g., Kouveliotou et al. 1993). We now think that these two types of GRBs have different progenitors. Short-hard GRBs (SHBs,sGRBs) are formed during COMs, such as two neutron stars, or a neutron star and a black hole (e.g., Belczynski et al. 2006; Nakar 2007). sGRBs are important to the field of gravitational wave (GW) astronomy, as COMs are a strong source of GWs. The progenitors of long-duration GRBs are massive stars at the end of their life cycle; during the violent deaths of massive stars, SNe and GRBs can form (e.g., Woosley 1993; Hjorth and Bloom 2012); a supernova is not always associated with a GRB, due to the beaming of GRB jets into very narrow angles (Paczynski and Rhoads 1993).

1.1.1.1 Prompt Emission and Jetting

Regardless of progenitor, GRB energy release during the prompt emission occurs when material is ejected outward at relativistic speeds in highly collimated jets (e.g., Paczynski and Rhoads 1993; Rhoads 1997). The material is not all ejected at once, with shells of material being expelled at various Lorentz factors at different times. The shells of material moving at different speeds can collide; the collision of these relativistic shells of material are called the internal shock (IS) (e.g., Rees and Meszaros 1994). The interaction of the relativistic shells of material causes acceleration of charged particles within the shell, leading to the emission of γ-rays. The prompt

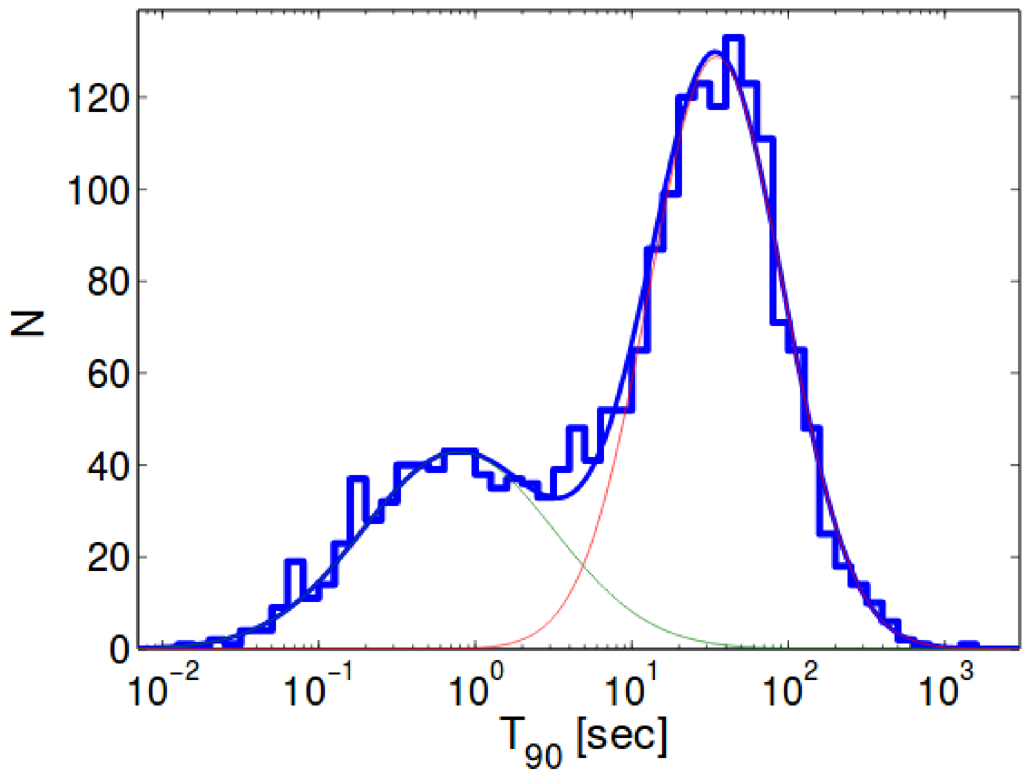

Figure 1. Bimodal distribution of GRB prompt emission durations

The bimodal distribution of the duration of the prompt emission of GRBs studied by BATSE, showing one population of bursts lasting less than 2 seconds (sGRBs), and another larger population lasting longer than 2 seconds (long GRBs). Image adopted from Nakar 2007. GRBs studied with *Swift* show a similar relationship (e.g., Zhang and Choi 2008; Gomboc and Kopac 2010).

emission from a GRB is caused by the IS which emits gamma-ray radiation through synchrotron emission (Meszaros, Rees, and Papathanassiou 1994).

The source of the highly collimated relativistic jets emanating from GRBs is not well understood. Studying GRB jets, and especially their polarization (e.g., Troja et al. 2017), can describe the magnetic fields around the central engines that could be the source of the collimated outflows (e.g., Piran 2005).

The rate of GRBs is dependent upon the nature of the jet (e.g., Rhoads 1999), as

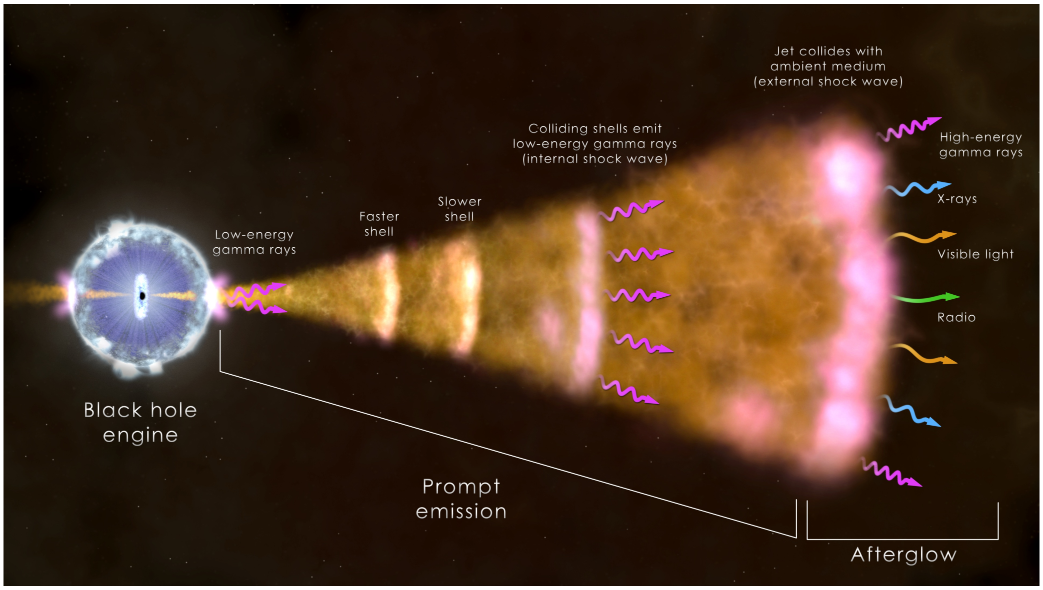

Figure 2. At then end of a massive star's life, a GRB can be formed. Following collapse, charged particles are ejected, as shells of material, into narrow jets moving at relativistic speeds. Different shells can be emitted at different velocities; these shells of material can collide, and it is this interaction that creates the emission of γ radiation during the prompt emission phase. The interaction of the shells with an external medium generates an afterglow, visible across a wide range of wavelengths. Image adopted from NASA's Goddard Space Flight Center website[1].

the prompt emission of γ-rays is only detected if Earth is within the opening angle of the jet. The sGRB rate is expected to follow the formation of compact object binaries (e.g., Narayan, Piran, and Shemi 1991; Coward et al. 2012; Nakar 2007), and as such is expected to be delayed when compared to the star formation rate (e.g., Guetta, D. and Piran, T. 2006; Nakar 2007). The supernova rate is about 1000 times greater than that for long GRBs due to the jetted nature of the latter's emission (e.g Yoon, Langer, and Norman 2006; Guetta, Piran, and Waxman 2005; Priddey et al. 2007).

Understanding GRB jets will help determine their energetics (i.e. the isotropic energy (E_{iso}) versus the collimated energy Freedman and Waxman 2001; Wygoda et al.

[1] https://www.nasa.gov/feature/goddard/nasas-swift-spots-its-thousandth-gamma-ray-burst

2016; Sari, Piran, and Halpern 1999; Kocevski and Butler 2008; Ghirlanda, Ghisellini, and Lazzati 2004; Ghirlanda et al. 2013; Amati, L. et al. 2002).

The energy and velocity structure of GRB jets has been previously explored (e.g., Granot and Kumar 2003; Rossi et al. 2002; Kumar and Granot 2003; Lipunov, Postnov, and Prokhorov 2001), and is a main focus of Chapter 3.

At ignition, the central part of the jet is causally disconnected from the outer regions of the jet. Over time, these regions will become causally connected, at which point information about the lack of pressure at the jet edge can reach the center; the jet can then potentially begin spreading laterally outward (see, e.g., Wygoda, Waxman, and Frail 2011; Eerten and MacFadyen 2012; Granot and Piran 2012). If the jet spreads, it can effectively halt the blast wave expansion and further decrease the afterglow flux (Rhoads 1999; Sari, Piran, and Halpern 1999; Granot et al. 2001; Wygoda, Waxman, and Frail 2011). Hydrodynamical processes that potentially lead to a spreading jet are explored in e.g., Sari, Piran, and Halpern 1999; Granot et al. 2001; Mao and Wang 2001; Zhang et al. 2006.

Due to the finite travel time of light, the synchrotron emission from material in the part of the jet closest to the observer is visible before the rest of the jet. As time passes, more of the jet becomes visible to the observer (e.g., Rhoads 1999). This relativistic effect occurs simultaneously to the widening of the jet angle.

1.1.1.2 Gamma-ray Burst Afterglows

It is not only the initial wave of gamma rays in the prompt emission that allow for the study of GRBs. An afterglow caused by the interaction of relativistic outflow from the burst interacting with the inter-stellar medium (ISM) or circum-burst medium

(CBM) can also be detected (e.g., van Eerten 2013); this external shock (ES) produces a forward shock (FS) on the CBM and a reverse shock (RS) on the jet itself (e.g., Mészáros and Rees 1997). As in the case of prompt emission, the emission mechanism for GRB afterglows is synchrotron radiation. GRB afterglows peak in the IR about 10 days after the prompt emission (Rau et al. 2004).

GRB afterglows are not as highly collimated as the prompt emission in γ-rays. Therefore afterglows are detectable through a wider angle than the prompt emission. An orphan afterglow (e.g., Totani and Panaitescu 2002) occurs when the afterglow is detected, but the prompt emission is not; an orphan afterglow has been detected in the radio (C. J. Law et al. 2018), and searches are ongoing for the first optical orphan afterglows.

Following the prompt emission, different phenomena shape the light curve of a GRB afterglow over time. At early times, the ES (FS and RS) creates a wide peak in brightness before the afterglow slowly loses energy at later times. The afterglow lightcurve behavior is modeled by a broken power law. The decreasing light curve behavior is modeled by a power-law function, $F \propto t^{-\alpha}$, where F is the flux, t is the time since the burst, and α is the power-law index.

The relativistic nature of the GRB jet, as described in the Prompt Emission and Jetting Section (1.1.1.1), will have consequences on the afterglow light curve. Eventually, the entirety of the jet is visible to the observer, and the jet edges and center become causally connected; the confluence of these two events results in a sharp decrease in the luminosity of the jet. This sharp decrease in luminosity is known as the jet-break; the jet-break time can be used to determine the bulk Lorentz factor, Γ, of the jet, and the jet opening angle, θ_j (e.g., Sari, Piran, and Halpern 1999; Frail et al. 2001). Therefore, the late-time behavior of the light curve of a GRB afterglow will be a superposition of these features: the overall decreasing trend as the afterglow loses energy, and information about the jet structure, as more of the jet becomes visible.

To see, mathematically, the relativistic effects on jetting and GRB afterglows, consider GRB photons emitted by shells, moving at velocity, v, with respect to an observer located at a distance, D, from the GRB. The first photon is emitted at time, t_1, in the moving frame. It arrives at the observer at a later time, $T_1 = t_1 + D/c$. A second photon is emitted at t_2. It arrives at the observer at $T_2 = t_2 + (D - v(t_2 - t_1))/c$, because the shell has moved by distance $v(t_2 - t_1)$ since t_1.

Thus $T_2 - T_1 = (t_2 - t_1) - \frac{v}{c}(t_2 - t_1)$, or $dT = dt(1 - \beta) \sim dt/(2\Gamma^2)$. Here, $\Gamma^{-2} \approx (1 - \beta)(1 + \beta) \sim 2(1 - \beta)$ in the limit where $\beta \approx 1$ (see Equations B.9-B.11 for a detailed proof). The observer-frame time is compressed relative to the emitter frame time; Γ is typically very large.

Thus, if we consider a blast wave expanding from radius 0 to radius R over an observed time T, we have:

$$R = tc = 2\Gamma^2 Tc. \tag{1.1}$$

This is how the observed size of the GRB is related to the observed time.

The blast wave has some kinetic energy, E_K, some fraction η of which produces γ-rays with energy E_{iso}. That kinetic energy moves outward as the blast wave expands, shocking up and heating the external medium. Shocks convert kinetic energy into thermal energy, and the heated material radiates to produce the afterglow flux.

In the frame moving with the shock, if a mass of material M is swept up, the energy is ΓMc^2; this is converted to thermal energy. In the observer frame, the shock is moving toward us such that the thermal energy is a factor of Γ larger, or $\Gamma^2 Mc^2$.

We have:

$$M(T)\Gamma^2 c^2 = \frac{E_{iso}}{\eta} \tag{1.2}$$

Assuming a circum-burst density that is constant in time, $\rho = m_H n$, where m_H and n are the mass and number density of hydrogen atoms, respectively, we have:

$$\frac{4}{3}\pi R^3 m_H n \Gamma^2 c^2 = \frac{E_{iso}}{\eta} \tag{1.3}$$

And, plugging in $R = 2\Gamma^2 Tc.$ from Equation 1.1, we have:

$$\Gamma = \left(\frac{3E_{iso}}{32\pi\eta m_H n c^5}\right)^{1/8} T^{-3/8}. \tag{1.4}$$

Due to relativistic effects, only an angle $\theta = 1/\Gamma$ of the jet can be observed. As Γ decreases (the blast wave decelerates), more of the jet becomes visible. Eventually, the viewing angle reaches the edge of the GRB jet (i.e. $\theta_{jet} \sim 1/\Gamma$). Here, $1/\theta_{jet} = \Gamma(T_{jet}) = \left(\frac{3E_{iso}}{32\pi\eta m_H n c^5}\right)^{1/8} T^{-3/8}$.

Including the redshift, an observed jet break at time T_{jet} would predict a full jet opening angle of

$$\theta_{jet} = \left(\frac{3E_{iso}}{32\pi\eta m_H n c^5}\right)^{-1/8} \left(\frac{T_{jet}}{1+z}\right)^{3/8} radians. \tag{1.5}$$

The proceeding derivation follows from Frail et al. 2001. In Strausbaugh et al. 2019, Chapter 3, we make use of Equation 1.5 and explore the effects of relativistic beaming on the afterglow of GRB 160625B, which exhibits interesting phenomena around the jet-break.

If the lightcurve was declining as $T^{-\alpha}$ until the jet break time, T_{jet}, then it is declining faster after the jet break as $T^{-\alpha}\ (T/T_{jet})^{-3/4}$ for $T > T_{jet}$. This is because the observed flux is related to the average flux in the jet, $f(\theta)$, integrated over angle. If the jet flux versus angle is constant (say 1), the flux averaged over angle will be proportional to $F(\theta) = 2/\theta^2 \int f(\theta)\theta d\theta = 1$ as well. Once $f(\theta)$ goes to zero at the edge of the jet, θ_{jet}, $F(\theta) = (\theta_{jet}/\theta)^2$. So, the flux starts do drop more rapidly by a fraction $(\theta_{jet}/\theta)^2 = (T_{jet}/T)^{3/4}$. That is, the average flux per solid angle is no longer growing as rapidly because there is no extra flux past the edge of the jet.

At early time, during the GRB prompt emission phase, the situation is somewhat different. The GRB starts out with constant $\Gamma = \Gamma_0$, which only begins declining after the blast wave decelerates in time T_d. This is the time at which the swept-up mass energy first equals the burst kinetic energy, $4\pi/3\Gamma_0^2 R^3 m_H n c^2 = E_{iso}/\eta$, so

$$T_d = (3E_{iso}/(32\pi\eta m_H n c^5))^{1/3}\Gamma_0^{-8/3}. \tag{1.6}$$

That time is typically several hundred seconds after the GRB, after which the afterglow begins. The derivation above then becomes valid, with $\Gamma = \Gamma_0(T/T_d)^{-3/8} = \Gamma_0 T_d^{3/8} T^{-3/8}$.

GRB afterglows can be used as probes of the ISM and inter-galactic medium (IGM) (e.g., Chornock et al. 2013). GRB afterglows have a uniform and easy to model power-law spectrum emitted via synchrotron emission over all wavelengths. This known spectrum allows for the accurate determination of the redshift of GRB afterglows (e.g., Krühler et al. 2011; Littlejohns et al. 2014); because synchrotron emission covers all wavelengths, GRB afterglows are optically detectable at high redshifts.

With a known photometric redshift, we can look for the effects of the Lyman forest (Lynds 1971) on the spectrum of the GRB afterglow. At high redshifts, Lyman-α (Ly-α) emissions and absorption will be shifted redwards, and at $z > 5$, will be shifted into near-infrared (NIR) wavelengths. Ly-α is the transition of an electron from the n=2 to the n=1 orbital (or n=1 to n=2 in the case of absorption) of a hydrogen atom that emits (or absorbs) a photon with a wavelength of 121.567 nm (e.g., Griffiths 2005). With the known spectra of a GRB afterglow as a reference, a lack of emission at Ly-α wavelengths is indicative of absorption by intervening neutral hydrogen in the ISM/IGM; a complete lack of emission at Ly-α wavelengths is called the Gunn-Peterson absorption trough (Gunn and Peterson 1965). If, however, we see emission from the GRB afterglow at Ly-α wavelengths, we can infer that the ISM/IGM must be partly ionized (e.g., Chornock et al. 2013) at the redshift of the GRB. In this way, GRB afterglows can be used to probe the Epoch of Re-ionization.

There are additional motivations for studying GRB afterglows in the IR. GRB afterglows have their peak brightness in the IR, and last longer in this bandpass (e.g., van Eerten 2013; Rau et al. 2004). Visible and ultraviolet (UV) light is heavily attenuated by ISM/IGM dust; as such, targeting GRB afterglows in the IR can reduce the detection rate of dark GRBs (GRBs with detected prompt emission, but no optically detected afterglow, e.g., Greiner, J. et al. 2011).

1.1.2 Supernovae

Supernovae are the calamitous explosions that can occur at the end of a stars life; there are two different channels for the creation of a supernova: core collapse of a massive star or accretion in a binary system.

Throughout the life cycle of a massive star, different phases of nuclear reactions occur, from hydrogen, helium, carbon, neon, oxygen, and finally silicon; silicon burning yields iron through a set of fusion reactions reliant on photo-disintegration (e.g., Clayton 1983). The iron produced is inert, as the energy needed to initiate iron fusion is less than the energy released by the reaction. When the iron core exceeds the Chandrasekhar limit, the star's nuclear reactions are no longer enough to counter the in-fall of gravity and consequently the star undergoes a rapid gravitational collapse (e.g., Janka et al. 2007).

Core collapse (Type II) supernovae are theorized to produce gravitational waves, which have important implications in observational and theoretical physics (Logue et al. 2012). Gravitational waves from a core collapse have not yet been detected, as the SN must be very close by, or its signal will be too faint to detect with current instruments.

Type Ia supernovae, caused by the accretion, above the Chandrasekhar limit, of material from a companion star onto a white dwarf in a binary system, are more uniform than supernovae formed by the collapse of massive stars. The Chandrasekhar limit (Chandrasekhar 1934) is the well-defined point at which the electron degeneracy pressure of a white dwarf can no longer support the mass of the accreting white dwarf; this mass-limit (≈ 1.38 solar masses) is responsible for Type Ia uniformity (Mazzali et al. 2007).

The accretion method of creating a supernova is promising from the standpoint of devising a uniform cosmological standard candle. One way to constrain dark energy, the unidentified 70% of the matter and energy density of the universe, is through the establishment of a standard candle for cosmology. A standard candle is an object or event that produces a consistent luminosity no matter where or when it occurs in the universe, such as a type Ia supernova. Using type Ia supernovae as standard candles the distance to the event can be determined by measuring its brightness; the spectra of these supernovae can provide the relative velocities of these objects. Combining the distances and relative velocities, reveals not only the expansion (Hubble 1929), but the accelerated expansion of the universe (Riess et al. 1998).

While the light curves of supernovae studied in the optical can be normalized to act as a standard candle, work in the IR shows more promise for uniformity (Friedman et al. 2015), because IR light is not as heavily attenuated by dust (Mandel, Narayan, and Kirshner 2011). The peak intensities of the supernova luminosity in the optical and IR are uncorrelated, and therefore offer independent measurements for distances. Using both optical and IR data, magnitude errors for Type Ia supernovae can be reduced by more than 25% (Mandel, Narayan, and Kirshner 2011).

1.1.3 Nucleosynthesis from Transient Sources

SNe (David and Clayton 1970; Hashimoto et al. 1996; Fuller and Meyer 1995) and GRBs (Li and Paczyński 1998a) have been theorized as the source of nuclei heavier than iron in the universe. Light elements – hydrogen, helium, and lithium – are believed to have been created early in the universe during a process called Big Bang nucleosynthesis (Alpher, Bethe, and Gamow 1948; Boesgaard and Steigman 1985; Wagoner 1973); stellar nucleosynthesis, driven by nuclear reactions within stars, can account for the creation of elements heavier than lithium, but less massive than iron (Eddington 1920; Hoyle 1946, 1954; Burbidge et al. 1957; Clayton 1983). The origin of the elements is traced out in Figure 3.

1.1.4 Kilonovae

Compact object mergers involving neutron stars offer a unique channel for production of an electromagnetic signal, separate from GRBs. Both neutron star-neutron star (NS-NS) mergers and neutron star-black hole (NS-BH) mergers are capable of ejecting the exotic, neutron-rich matter that a neutron star is composed of, into the

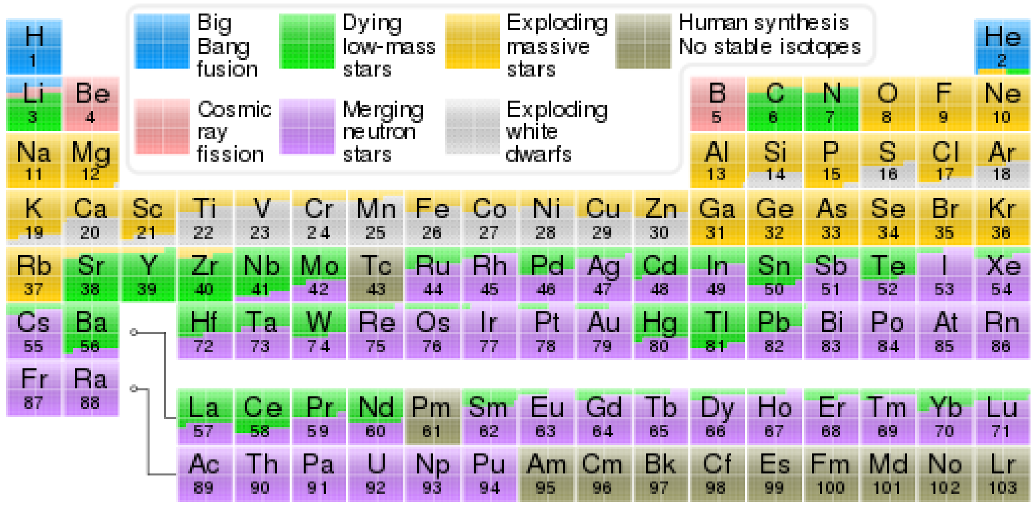

Figure 3. A periodic table that displays the cosmic origins of various elements. Elements heavier than iron are created by transient phenomena (e.g. merging neutron stars and exploding high mass stars can be observed as GRBs, and exploding white dwarfs and exploding high mass stars result in SNe). Image adopted from Wikipedia[2].

circum-burst medium at tremendous energies; neutron-rich matter is expelled during the sGRB that occurs after a NS-NS merger (e.g., Li and Paczyński 1998b), whereas tidal disruption forces can rip apart and expel some neutron-rich matter during a NS-BH merger (e.g., Rosswog 2005), before it has the chance to fall into the black hole.

In either case, neutron-rich ejecta is expelled into the CBM and captured by the atoms in the surrounding medium, leading to the formation of heavy, radioactive elements by r-process nucleosynthesis (e.g., Lattimer and Schramm 1974, 1976; Freiburghaus, Rosswog, and Thielemann 1999). These radioactive elements decay, emitting light isotropically in a kilonova (e.g., Metzger et al. 2010), and have been detected (Tanvir et al. 2013; Berger, Fong, and Chornock 2013).

The spatial uniformity of the kilonova electromagnetic signature has implications

[2]https://upload.wikimedia.org/wikipedia/commons/3/31/Nucleosynthesis_periodic_table.svg

for its use as an electromagnetic counterpart to gravitational waves, and allows for the detection of compact object mergers where the beam of the GRB is not directed towards the Earth. The radioactive decay that produces the kilonova can be detected at its greatest intensity in the IR (Tanvir et al. 2013), and peaks in the first 1-4 days after coalescence (e.g., Li and Paczyński 1998b; Rosswog 2005; Piran et al. 2014), before fading after 1-2 weeks (e.g., Tanvir et al. 2013; Berger, Fong, and Chornock 2013).

1.1.5 Electromagnetic Counterparts to Gravitational Waves

The general theory of relativity, as posited by Einstein in the early 20^{th} century, predicted that space-time was a fabric which could be distorted by matter and energy; the effects of gravity propagate on this space-time fabric like a wave. One hundred years later, experimental science has detected the first gravitational waves, with aLIGO ushering in a new era of astronomy (Abbott et al. 2016).

The first GW detection was followed not long after by the dual gravitational wave-electromagnetic (GW-EM) counterpart detection (Abbott and al. 2017; Abbott, Abbott, Abbott, Acernese, Ackley, Adams, Adams, Addesso, Adhikaril, et al. 2017, and references therein), starting an era of multi-messenger astronomy; following the gravitational wave event, GW170817, a short duration GRB and a kilonova were detected as EM counterparts. Using gravitational waves as triggers for electro-magnetic counterpart follow-up, it has been shown that the progenitors of some short GRBs are compact object mergers (e.g., Abbott, Abbott, Abbott, Acernese, Ackley, Adams, Adams, Addesso, Adhikaril, et al. 2017).

Determining the source of these gravitational waves is not easy, however. Surveys seeking to detect gravitational waves have very poor spatial resolution; thousands of possible candidates could lie within the 100s of square degrees in the aLigo error region (Golkhou et al. 2018). EM counterparts to GWs are important due to the poor spatial resolution of interferometers like aLIGO and Virgo, can help determine the progenitors of GWs, and provide more information about the host galaxy. Redshifts determined from EM sources coupled with luminosity distances from GWs allow for an independent measurement of the Hubble constant (e.g., Deffayet and Menou 2007; Abbott, Abbott, Abbott, Acernese, Ackley, Adams, Adams, Addesso, Adhikari, et al. 2017), used as a constraint on the amount of dark energy in the universe. The detection of gravitational waves generated by a collapsar, creating both a SN and long GRB (e.g., Woosley 1993), could resolve the debate between different explosion mechanisms (Summerscales et al. 2008; Powell et al. 2016).

Compact object mergers are expected to create the strongest GW signals, and comprise the only GW signals detected so far. Binary black hole mergers are the strongest sources of gravitational waves (e.g., Lipunov, Postnov, and Prokhorov 1997), but are not expected to have a strong EM counterpart, if any at all, (e.g. Metzger 2017). There is speculation, however, that if enough mass is shed during the black hole progenitor's evolution, an accretion disk may be able to power an EM counterpart in the event of a binary black hole merger (e.g., Mink and King 2017).

Binary neutron star or neutron star-black hole mergers create weaker GW events due to the smaller system mass, but should have an EM counterpart: short GRBs and their afterglows (e.g., Kochanek and Piran 1993), orphan afterglows (e.g., Totani and Panaitescu 2002), or kilonovae (e.g. Metzger et al. 2010). We might be able to identify candidates for this type of coalescence, and determine when an event is likely to occur, by studying X-ray binaries (e.g., Hulse and Taylor 1975; Lewin, Paradijs, and Heuvel 1997; Remillard and McClintock 2006; Ballantyne et al. 2012)

The deaths of massive stars are also predicted to produce GWs, but at a much weaker intensity than any compact object merger (e.g., Ott et al. 2011). Long GRBs and SNe can accompany the GWs released following the deaths of these massive stars (e.g., Woosley 1993), leading to EM counterpart detection.

Many of the triggers for the generation of gravitational waves, such as core collapse supernovae, and GRBs are not spatially uniform. Unless the Earth is in the electromagnetic sight-line of one of these events, the gravitational wave detection will not be coupled to a known source. While much fainter, kilonovae are spatially uniform, and therefore are excellent candidates for EM counterparts to GW (e.g. Li and Paczyński 1998b; Rosswog 2005).

1.1.6 Exoplanet Transits

The study of exoplanets offers an insight into not only the formation of planets, but also the stars around which those planets orbit. Studying the transits of exoplanets around their host star is one way to study these systems. Recent analysis has shown that the efficiency of transit surveys can match and exceed the more conventional radial velocity surveys (e.g., Burke and McCullough 2014).

There are two competing theories for planetary system formation. One theory involves the swirling of gas and dust around gravitational wells (Snytnikov and Stoyanovskaya 2013; Basu and Vorobyov 2012; Rafikov 2008). Alternatively, material larger than gas and dust collides and combines to create even larger objects in a cascading effect, which ends with planet sized objects (e.g., Thebault, Kral, and Ertel

2012). Recent models have shown evidence for both of these mechanisms being in play during planetary nascence (e.g., Lambrechts and Johansen 2012).

Evidence for planets orbiting other stars was first discovered using the radial velocity method (e.g, Mayor and Queloz 1995). A system in which a planet orbits a star will cause the center of mass of the system to be shifted away from the center of the star. The star will then orbit around this new center of mass. This orbit will cause the star to be at times moving towards the Earth, and at other times moving away from the Earth. The differences in these velocities results in a Doppler shift in the emission spectrum of the star; studying the displacement of these emission lines can determine characteristics of the planet in the system, such as planetary mass and orbital radius (e.g., Feroz, Balan, and Hobson 2011).

Analysis of ground based transit surveys has shown that their efficiency is comparable to radial velocity surveys (e.g., Burke and McCullough 2014); the launch of the Transiting Exoplanet Survey Satellite in 2018 is revolutionizing the study of exoplanet transits (Ricker et al. 2014). Studying the transits of exoplanets around their host star leads to additional information beyond the orbital mechanics. Using the amount of star light blocked by the planet, the radius of the planet with respect to the host star can be determined. Assuming the star is on the main sequence, its radius and therefore the planet's radius, can be determined. Combining the planetary mass from radial velocity measurements, with the planet's radius from transit observations, leads to a determination of the density of the exoplanet.

In addition, the atmosphere of the planet can be characterized by studying the transmission and emission spectra during a transit (e.g. Charbonneau et al. 2002; Bean et al. 2011; Kreidberg et al. 2014). Exoplanetary atmospheres can also be studied using direct imaging techniques (e.g., König et al. 2002).

A visual representation of the geometry of a transiting exoplanet system is shown in Figure 4. While the planet is neither in front nor behind the star, most of the light detected is from the host star, while a small fraction of the light will be emitted from the planet; if measurements are made spectroscopically, the result is an emission spectrum for the star and planet. When the planet passes in front of the star, not only will the intensity of the light decrease, as seen at the bottom of Figure 4, but the spectrum of the light will also change.

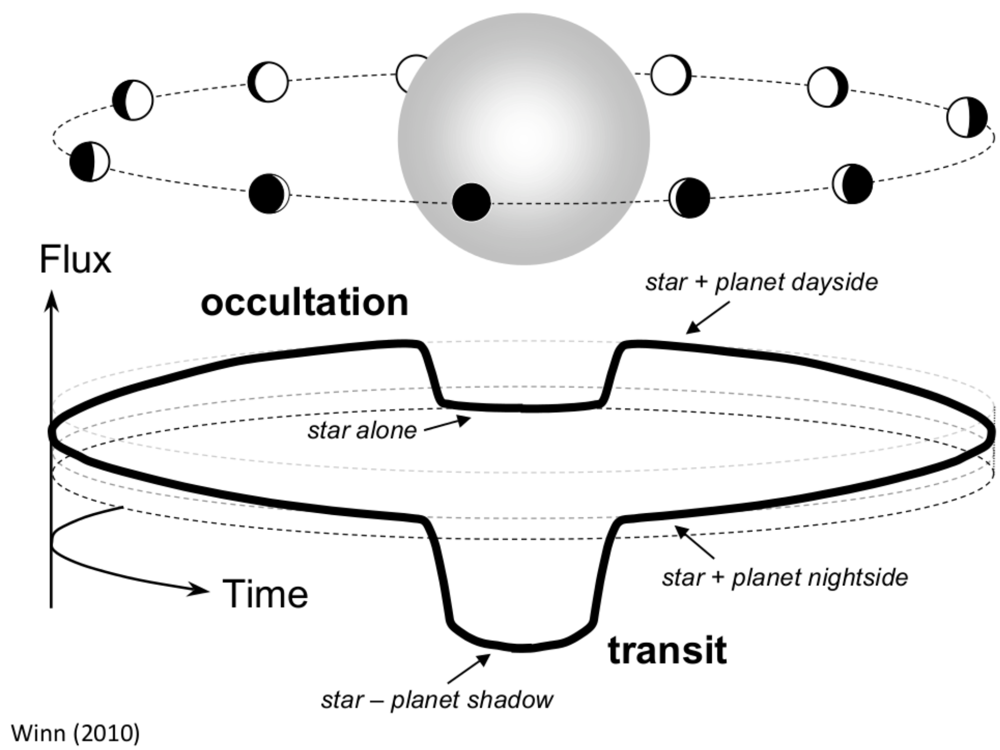

Figure 4. Exoplanet Transit Model

A model of an exoplanet transit, with the expected light curve. The primary transit occurs when the planet passes in front of the star, and the secondary transit occurs when the planet passes behind the star; both transits are important for spectroscopic study of exoplanet atmospheres. Image adopted from Winn 2010.

The atmosphere of the exoplanet can absorb some of the light from the star when it passes in front of the star; this is either a transmission spectrum, if looking at the light that made it through the atmosphere, or an absorption spectrum if looking for the light which did not make it through the atmosphere. Different elements and molecules in the exoplanet atmosphere can be identified by studying the wavelength, of these absorption features.

Studying the secondary transit, as the exoplanet passes behind the star can help us find the emission spectrum of the planet itself. Subtracting the spectrum when the exoplanet is neither in front nor behind the star, from the spectrum when the planet is behind the star will directly reveal the emission spectrum of the exoplanet (e.g., Baskin et al. 2013).

For the transit of an exoplanet around its host star, the signal is determined by the normal intensity of the star, I, and the minimum intensity of the star, I_0, during transit, $Signal = \frac{I}{I_0} = \exp^{-\tau}$; the transit of an exoplanet may also be characterized by a factor called the optical depth, represented by τ.

Telescopes operating in the IR range can study cooler objects; stars which previously couldn't be studied in the visible and UV are viable sources in the IR. The study of brown dwarfs should benefit greatly from the ability to resolve cooler objects (e.g., Warren et al. 2007). Brown dwarfs are stellar mass objects which for an as yet undetermined reason never initiated hydrogen-burning (e.g., Reiners et al. 2007). Brown dwarfs have been found with exoplanets of their own (e.g., Joergens and Müller 2007), which could provide insight into stellar and planetary evolution.

In addition to being able to study cooler objects, the shape of transit light curves in the IR makes for easier identification. Limb darkening is the effect that causes stars to appear darker on the outside of their disk. This is due to the optical depth at the edge of the star being smaller than at the center, as well as the temperature of the limb being lower (e.g., Neilson and Lester 2011a). Less optical depth means fewer chances for emission, and lower temperature means less intense emission of light. This limb darkening is dependent on the wavelength of the emitted light; longer wavelength light is not as influenced as shorter wavelength light (e.g., Howarth 2011a). There is not as much limb darkening while imaging in the IR; therefore an exoplanet transit can be detected much closer to the edge of the stars disk. Exoplanet transit light curves in the IR are sharper than in the visible or UV; IR light curves have a flatter bottom and steeper sides. This shape can allow for easier transit detection, especially by automated computer searches.

In the search for Earth-like life, we look for planetary densities (determined using both radial velocity and transit data) indicative of rocky planets, as opposed to gas giants, or liquid planets, that orbit within the habitable zone of their host star (determined with radial velocity data). The atmosphere of a planet fitting these criteria could then be studied using the primary and secondary eclipses obtained using transit study (e.g., Belu et al. 2011), searching for chemical signatures of life (e.g., Domagal-Goldman et al. 2011; Fujii et al. 2018; Schwieterman et al. 2018). Such an atmospheric study should be possible with JWST (e.g., Greene et al. 2016; Beichman et al. 2014).

The search for Earth-like planets offers the best chance to identify the potential for life that is similar to life on Earth. These exoplanets might also hold the future for human evolution into space. Developing a catalog of stars with exoplanets would also help answer the questions of the frequency with which planetary systems form around stars.

1.1.7 Other Transient Sources

There are several other transient sources that, while important, are not within the scope of this dissertation. These sources include: novae, RR Lyrae, and Cepheid variables, which will be described here briefly, as well as others that have not been included.

Novae are thought to be the result of objects in a binary system interacting with each other. Binary systems consisting of a white dwarf and a companion star can result in explosions called classical novae. If the companion star is close enough to the white dwarf, hydrogen from the atmosphere of the companion can accrete onto the surface of the white dwarf. Once the accreted hydrogen reaches a critical temperature, due to the latent heat of the white dwarf, fusion reactions can occur (e.g., Gallagher and Starrfield 1978); this process produces a bright flash of light, and expels the fused matter into the ISM. This process can occur several times, resulting in recurrent novae (e.g., Webbink et al. 1987; Schaefer 2010). A related phenomena can occur during the merger of two stars in a binary system; these events are called red luminous nova, as they are brighter, and their spectra more red, than classical novae (e.g., Kulkarni et al. 2007; Kasliwal et al. 2011; Rau et al. 2007).

An RR Lyra is thought to be an older A or F star that has progressed through its life cycle to the point of helium burning; at some point during its evolution, the RR Lyra loses its outer Hydrogen envelope (Smith 2004). Without the outer hydrogen envelope, an instability can form between layers of the stars atmosphere, governed by the κ-mechanism (e.g. Cox 1980).

In a typical star, an increase in the temperature of a layer in the stellar atmosphere will cause the opacity to decrease, allowing for more energy to be radiated away, thus maintaining an equilibrium. Layers of partly ionized hydrogen and helium, like those exposed in RR Lyrae stars, behave inversely (e.g. Maeder 2009): opacity increases with temperature. Therefore, when an outer layer in an RR Lyra falls deeper into the star, the layer will become more opaque and collect more energy; this results in a buildup up pressure that will eventually push the layer back outwards. The cyclic process of in-fall, pressure buildup, and outwards expansion results in the regular period of the RR Lyra, typically about one day or less (e.g., Lafler and Kinman 1965; Smith 2004).

Similar to RR Lyrae, the pulsations from Cepheid variables can be traced back to the κ-mechanism (e.g. Cox 1980). Unlike their lower mass cousins, Cepheids are much brighter, and thought to be high mass stars in the latter stages of their life, after losing their outer shell of hydrogen (e.g., Turner 1996). The period for Cepheid variables is much longer than RR Lyrae, from days to months (e.g., Gieren, Fouque, and Gomez 1998; Pierce et al. 1994).

The location of various transient sources is plotted on a Hertzsprung-Russel diagram in Figure 5. Transient sources are crucial for determining cosmological distance scales. We can use parallax, the angular distance stars appear to move on the sky as a result of Earth's orbit around the Sun, to determine the distances to stars within our own galaxy. For distances outside of our own galaxy, we rely on transient phenomena. Variable stars, like RR Lyrae and Cepheids are important as first rungs on the cosmological ladder of distance scales (e.g., Cacciari and Clementini 2003; Madore and Freedman 1991). Type Ia supernovae, as previously discussed, can be used as standard candles to determine cosmological distances.

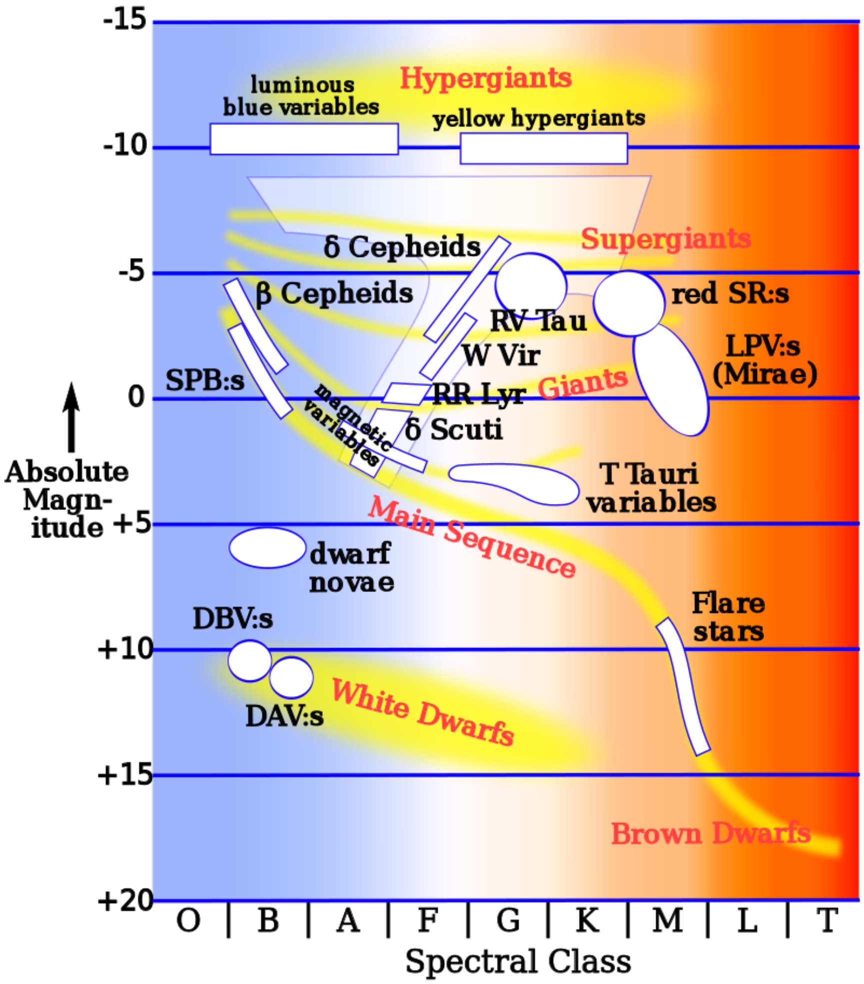

Figure 5. A Hertzsprung-Russel diagram highlighting the location of transient sources on the instability strip. Stars can evolve off the main sequence and onto the instability strip by shedding their outer hydrogen layer. Without the outer hydrogen envelope, the κ-mechanism (e.g. Cox 1980) can cause the star to pulsate, resulting in a regular period, useful for determining cosmological distance scales. Image adopted from Wikipedia[3].

[3]https://en.wikipedia.org/wiki/File:HR-vartype.svg

1.2 Infrared Astronomy

Short wavelength infrared (SWIR) and near-infrared (n-IR) astronomy (λ=750-3000 nm) provides the tools to probe many mysteries of cosmological and astrophysical origin. There are several advantages to working in these wavelengths. IR light scatters off interstellar dust at a much lower rate than visible or ultraviolet light. Cooler objects may be studied in the n-IR range, such as brown dwarfs. Exoplanet transit light curves are more sharply defined in the IR. Type Ia supernova light curves are more standard in the IR. GRB afterglows have their peak brightness in the IR, and also last much longer in this regime. An electromagnetic counterpart to gravity waves should be strong in the IR.

Interstellar dust scatters light in the visible and ultraviolet wavelengths much more effectively than in the IR. The wavelength, λ, of IR light is much longer than the size, a, of inter-stellar dust (Glass 1999); this regime where $\lambda >> a$ is described by Raleigh Scattering. The loss of light from scattering is called extinction. The extinction of the intensity of the light due to dust scattering is given by $\frac{dI}{I} = -n_d C_{ext} dL$, where I is the intensity of the light, n_d is the number of particles per unit volume, C_{ext} is the extinction cross-section, and dL is the path length.

While IR light is relatively unencumbered by the ISM, there are certain limitations when observing in IR. The terrestrial sky is very bright in IR, due to absorption and emission from particles in the atmosphere (Sivanandam et al. 2012). Fortunately there are several techniques which can mitigate this problem. The Y-band is a gap, at 0.96-1.08μm, in the emission and absorption spectra of the gases that make up the atmosphere, providing an uninterrupted window for observations (Choi et al. 2012); the Z, J and H-bands, while not as clean as the Y-band, are also useful for making astronomical observations (e.g., the transmission spectra in Figure 7). Another technique which covers the deficiencies of terrestrial IR observations is the method of periodically pointing the telescope away from the source to a brighter target, while ensuring the same pixel is irradiated (Mann, Gaidos, and Aldering 2011).

1.2.1 Infrared Detectors

The photoelectric effect (Einstein 1905), which won Einstein the Nobel Prize (Arons and Peppard 1965), is the underlying principle behind the photo-diodes used to detect and measure light from astronomical sources. Telescopes focus light onto a device that will record or measure the incoming photons (historically it was photographic plates, and now it is digital detectors). Modern detectors have a layer called the substrate that will interact with photons of a specific range of wavelengths, or frequencies. Photons with shorter wavelengths do not penetrate the surface of the substrate, while photons with longer wavelengths pass through the material without interacting (Mackay 1986). Photons with the correct wavelength enter the bulk of the material, and remove an electron from the valence band to the conducting band of the substrate. Modern electronics can measure these electrons as a charge, and read that charge into a digital count. These digital counts over many pixels on a detector can build an image of an astronomical source.

The current standard for infrared astronomical detectors are mercury-cadmium-telluride (HgCdTe or MerCad) semiconductors; this semiconductor was first synthesized by Lawson et al. 1959. Charged coupled devices (CCDs), ubiquitous in visible wavelength astronomy, can not be used for IR astronomy, as the quantum efficiency of these devices breaks down for wavelengths longer than 1000nm.

MerCad detectors can be tuned to be sensitive to infrared light over a wide range of wavelengths: 0.7-25 μm (Norton 2002). MerCad detectors must be cooled to cryogenic temperatures (e.g., 60K cooling for RATIR, Butler et al. 2012) to have viable noise characteristics, greatly increasing the cost of systems using these detectors (Norton 2002).

Indium-gallium-arsenide (InGaAs) is alternative substrate used for observations in the IR with a much narrower bandpass (0.7-1.7 μm, Sullivan, Croll, and Simcoe 2013) when compared to HgCdTe. InGaAs was synthesized by Pearsall and Hopson 1977; Pearsall, Quillec, and Pollack 1979, decades later than HgCdTe, and is therefore not as mature as a technology. They key advantage that InGaAs has over HgCdTe is that the former does not need to be cooled to cryogenic temperatures to have useful noise properties (Sullivan, Croll, and Simcoe 2013; Nagayama et al. 2014; Strausbaugh, Jackson, and Butler 2018); as such, InGaAs has uses in the surveillance and night vision industries, and is therefore on a trajectory for the development of larger and more cost-effective photo-diode arrays.

The sensor tested in Chapter 2 has an array of InGaAs photo-diodes with a complementary metaloxide-semiconductor (CMOS). The absorption of photons occurs in the InGaAs layer, where an electron-hole pair is created in the band gap of the semi-conductor. The charge collected in the photo-diodes is shepherded to the CMOS via an indium bump bond. An integrated circuit at each pixel amplifies the photo-current, and then converts the current to a voltage. The voltage is read out row by row to an analog-to-digital converter (ADC) that converts the analog voltage output to digital counts. The noise inherent in this digitization process is known as read noise (RN).

1.2.2 Ground Based Infrared Telescopes

Ground based observations are noise limited by the Poisson noise of atmospheric emissions. The sky noise can be reduced by making observations at wavelengths with low noise, such as the Y-band in IR. The thermal noise from the instrumentation could be countered by cryogenically cooling the detectors, but this is not cost effective.

To observe fainter sources, more photons from the source must be collected. This can be done by increasing the integration time, but this also leads to greater noise. A larger collection area for the telescope offers the most effective way to increase the precision of observations.

Large telescopes, however are very expensive. In addition, they encounter an issue with scintillation. As the collection area of the telescope increases, so does the area of the sky through which the light it collects passes. The atmosphere can be quite turbulent, especially in the infrared; this turbulence is the reason for the twinkling of stars, and leads to problems when data is collected with a large telescope.

The issues of cost and scintillation with a single large telescope can be overcome with the use of smaller telescopes working together in an array. A network of telescopes fixes the scintillation problem because there are different lines of sight through which each telescope observes; averaging over these mitigates the effect of scintillation. The effective area of the telescopes can be made to match or exceed that of a single telescope (e.g. Kaiser et al. 2002; Beckers 1986). The effective area of an array of telescopes is the physical area multiplied by an efficiency factor based on the telescope.

An important aspect of such a telescope array is interferometry. With telescopes observing the same object, but spaced some distance apart, the timing of the events at each telescope must be correlated. Radio telescope arrays can be correlated computationally (e.g., Brown and Twiss 1954; Perley, Schwab, and Bridle 1989); a similar technique is not feasible for optical astronomy, and so physical systems have been developed to ensure correlation of signals from different telescopes (e.g., the system designed for the Very Large Telescope Interferometer, Petrov et al. 2007). Photon correlation interferometry can be used to directly measure the size of astronomical objects (e.g., Thompson, Moran, and Swenson 1986).

1.2.2.1 Re-ionization And Transients InfraRed Camera (RATIR)

RATIR is a multi-band (r, i, Z, Y, J, H) instrument that studies transient sources, specifically the afterglows of GRBs (Butler et al. 2012). The instrument consists of 6 detectors, one for each band: 2 CCDs for the r and i bands, and 4 HgCdTe detectors for the remaining bands. The incoming beam is split into the different wavelengths using high efficiency dichroic filters, that operate on the principle of thin film interference (e.g., Macleod and Macleod 2010). The optical setup of RATIR is detailed in Figure 6, showing the beam path, detectors, and filters, and the quantum efficiency of the instrument is shown in Figure 7.

RATIR is mounted on the 1.5m Harold Johnson telescope at the Observatorio Astronómico Nacional in San Pedro Martir, Baja California, Mexico, and is joint venture between University of California, NASA Goddard Space Flight Center, and the Instituto de Astronomía of the Universidad Nacional Autónoma de México; ASU later joined the collaboration. The telescope is completely automated, and responds to triggers for GRBs from the Gamma-ray Coordinates Network (Alan M. Watson et al. 2012; Christopher R. Klein et al. 2012). The field of view of visible wavelength RATIR cameras is 5.3’x5.3’, while the field of view for the n-IR cameras is 10’x10’, but is vertically split. Collaborators are able to apply for telescope time to study sources of their choosing; however, predetermined programming is interrupted in the event of a GRB trigger, thanks to the robotic nature of the telescope.

RATIR afterglow data from GRB 160625B is presented in Chapter 3 (Strausbaugh et al. 2019). An overview of years worth of RATIR data, with an emphasis on its efficiency, is presented in Chapter 4.

1.2.2.2 A Test Bed of Small Telescopes at Arizona State University

As a part of the research in this thesis, small telescopes (12-inch and 18-inch diameters mirrors) were used to test detectors, study transient sources, and determine the feasibility of an inexpensive telescope array.

An 18-inch Newtonian telescope, f/4.5, with a split ring, equatorial mount produced by JMI, shown in Figure 8 was tested for use with the IR detector. This telescope model is highly mobile, making it suited for an array with movable components to suit different observational needs.

The mount is driven by an on board computer, the Servo Cat produced by Stellar Cat. It is capable of receiving signals from multiple external sources, such as a hand-pad or other computers.

The telescope is also fitted with two smaller telescopes, for alignment and guiding. A small polar alignment scope is attached to the base of the telescope; this allows the scope to be oriented correctly with respect to Polaris, the north star. A larger,

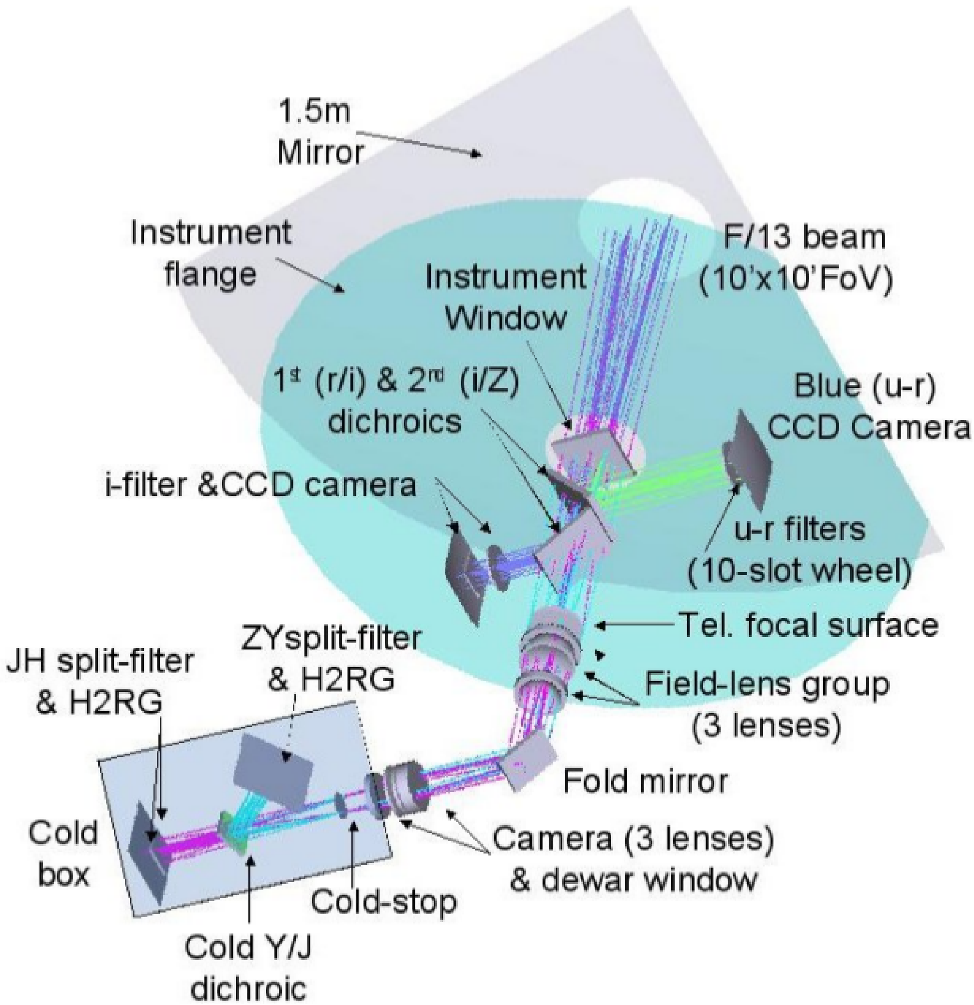

Figure 6. RATIR Optical Setup

The RATIR optical setup, showing light pathways through filters and dichroics to the cameras for detection. The n-IR detectors (H2RG in the figure) must be placed in a cryostat to maintain temperatures below 60K. Figure adopted from (Butler et al. 2012).

50mm scope is attached to the top of the telescope; this scope can be fitted with an eye piece for finding stars, or an optical camera for guiding.

Flat fielding allowed us to measure and reduce the effects of scattered light in the system (the InGaAs detector mounted on the 18-inch telescope), which proved to

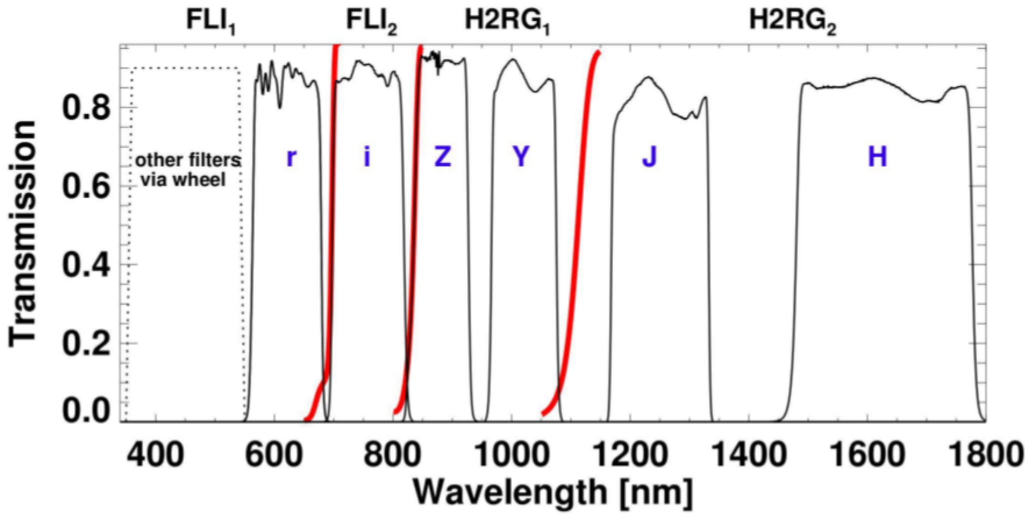

Figure 7. RATIR Quantum Efficiency

Transmission through the entire RATIR optical setup, including filters (labeled r,i,Z,Y,J, and H) and dichroics (denoted by the red lines). The cameras for detection are also listed above the graph. Figure adopted from (Butler et al. 2012).

be a greater problem in the IR than in the visible. A tarp was wrapped around the telescope to block this scattered light, improving noise properties by around a factor of 10. Next, internal reflections within the optical setup connecting the camera to the telescope were discovered; these were mitigated by covering the smooth, reflective, insides of the draw tube with felt paper which did not reflect IR light; this improved noise properties by another factor of 5.

A 12-inch Cassegrain telescope from Meade has also been utilized, and is shown in Figure 9. This is an f/10 telescope, and can be used with a wedge to switch between ALT/AZ and equatorial mountings. This telescope has its own internal motor and tracking software. It is also fitted with a guide scope compatible with guiding cameras. This scope was used when the physical limitation of the 18 inch were reached (e.g., looking in the extreme south sky).

Data collected from an InGaAs detector mounted on both the 12-inch and 18-

Figure 8. 18-inch JMI Telescope

The 18-inch JMI telescope on which much of the on-sky testing of InGaAs detectors was conducted. This telescope was also used with the InGaAs detectors to study transient sources.

inch telescopes are presented in Chapter 2 (Strausbaugh, Jackson, and Butler 2018). Continued work with the 18-inch telescope determined that the stock motors were underpowered for our research goals. As such either more robust motors, or different, more stable telescopes, like the 12-inch Meade, would be deployed in a telescope array.

1.2.2.2.1 Software and Additional Hardware for Small Telescopes

Hardware, such as tracking computers and guide cameras, that were necessary for the operation of the 18-inch and 12-inch telescope are discussed here. Third party

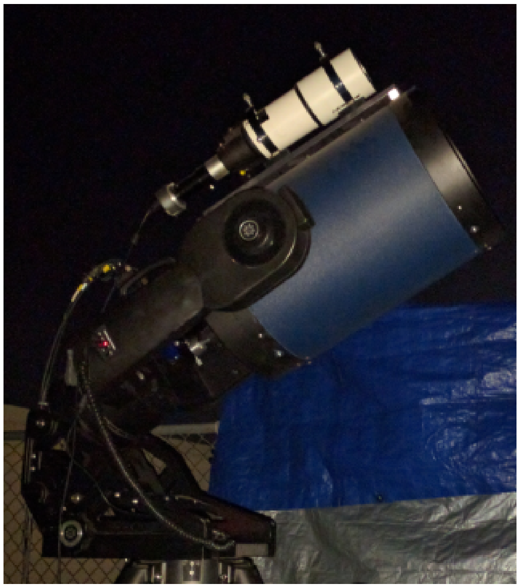

Figure 9. 12-inch Meade Telescope

The 12-inch telescope used to supplement the 18 inch telescope for the on-sky testing of detectors and the study of transient sources.

software such as PHD2 for guiding, as well as an original program used to collect data from an InGaAs detector, ICACTI, are discussed as well.

1.2.2.2.1.1 Argo Navis

An auxiliary computer mounted to the 18 inch telescope, the Argo Navis, determines the telescope's position on the sky. There are several different modes in which it can determine its position. The Argo Navis can assume that the telescope is very well aligned with Polaris, and then only requires a one star alignment. If there is insufficient confidence in the polar alignment, a different mode allows the telescope's position to be determined using a two star alignment. Once the telescope's orientation is determined, the Argo Navis calculates the speed at which the mount needs to move in order to keep up with the apparent motion of the sky, caused by the Earth's rotation.

A telescope is tracking, if it follows the motion of the sky throughout the night. The precision of both these modes has been tested. If the telescope is well-aligned with Polaris, and is stationary (i.e., in a dome), then the one-star align mode is sufficient; otherwise the two-star align mode is necessary for proper tracking.

1.2.2.2.1.2 Orion StarShoot Autoguider

The optical guide camera used on the 18-inch and 12-inch telescope is an Orion StarShoot Autoguider, as seen in Figure 10. The guide camera is attached to the finder scope on the side of the telescope. Placing the guide camera in conjunction with the IR camera using either a dichroic or a beam splitter results in a very narrow field of view, with too few stars for the guiding algorithm to work properly. The guiding camera needs to be used with a smaller secondary guide scope mounted on the telescope.

The sensor in the optical camera is a Micron MT9M001 CMOS chip. The sensor has physical dimensions of 6.66mm x 5.32mm and pixel dimensions of 1280 x 1024; the size of each pixel is $5\mu m$ x $5\mu m$. The camera can operate in a wide range of exposure times ranging from 0.05-10 seconds.

The size of the guide camera pixels on the sky for the 18-inch telescope's guide scope is 0.72 arcsec per pixel; on the 12-inch telescope's guide scope, the pixels are 2.68 arcsec per pixel.

A USB wire connects the camera to a computer (in our case running Windows 7), transmitting images that can be accessed by software such as PHD2 for guiding. The computer then sends commands either directly to the mount, using a USB to RJ-12 connection, or back through the camera via USB and then to the mount over

Figure 10. The Orion StarShoot AutoGuider, optical CCD camera, used for guiding on the 12-inch and 18-inch telescopes. The camera works with PHD2 guiding software to correct for any telescope movement not corrected by sky tracking software (e.g. wind or a skipped gear). Image adopted from telescope.com website[4].

an RJ-12 cable. The configuration with the greatest guiding precision is the one in which the computer communicates directly with the mount.

1.2.2.2.1.3 PHD2 Guiding Software

The guiding software chosen to interface with the guide camera and the telescope is PHD2 created by Stark Labs. PHD2 is initialized with information about the camera and mount. The dimensions of the camera and the individual pixel size are entered. Information about the mount and telescope, such as the focal length and aperture size are also entered. Through an ASCOM connection, the mount is able to relay information to PHD2, such as its pointing. PHD2 uses all of this information in its calibration phase, where it determines the effect of guiding pulses on the motion of the mount.

PHD2 receives images from an optical camera, and identifies the position of a

[4] https://www.telescope.com/Orion-StarShoot-AutoGuider/p/52064.uts

chosen guide star in the field of view. Based on the stars motion on the sensor, PHD2 sends a guide pulse to the mount, over an RJ-12 cable. The guide pulse is meant to move the mount so as to keep the guide star at the same location on the sensor.

There are various guiding algorithms that are accessible through PHD2 which can be set independently for both right ascension (RA) and declination (DEC). The hysteresis algorithm has proven to be the most reliable for both axes. Hysteresis uses its previous corrections to predict which corrections it needs to make in the future. The different parameters for this algorithm are aggression, hysteresis, minimum motion, and maximum pulse length.

The aggression setting determines what percentage of the guide pulse PHD2 calculated will actually be sent to the mount. This could be lowered if PHD2 were over correcting.

The hysteresis parameter sets the amount PHD2 should consider its previous corrections when calculating the next guide pulse. If guiding seems to be smooth, and all the corrections are going in the same direction, then this setting should be high; for choppy, unpredictable corrections, this setting should be low.

The minimum motion parameters in both RA and DEC set the amount the star has to move across the sensor before PHD2 will issue a guide pulse for correction. A high minimum motion setting can lead to the stars wandering, and making for streaky science frames. Minimum motion that is too low can lead to correcting for random noise, like the motion caused by atmospheric seeing.

The maximum pulse length determines how far PHD2 will be able to move the mount in a single pulse. This can be scaled to follow the integration time, but should not be so high that PHD2 can over correct and compromise guiding.

The integration time for the images, and thus the time between guide pulses is also a parameter that can be changed such that an appropriate guide star is in the field. While not explicitly a part of the guiding algorithm it must not be too high or too low, for the same reasons as the minimum motion.

Using PHD2 guiding in addition to the tracking carried out by the Argo Navis on the 18-inch telescope produced precise guiding where a source is able to be localized to one pixel on the InGaAs detector, as seen in Figure 11. Ensuring a source stays on a single pixel allows for easier stacking of images, and mitigates the effects of pixel-to-pixel variations on the detector.

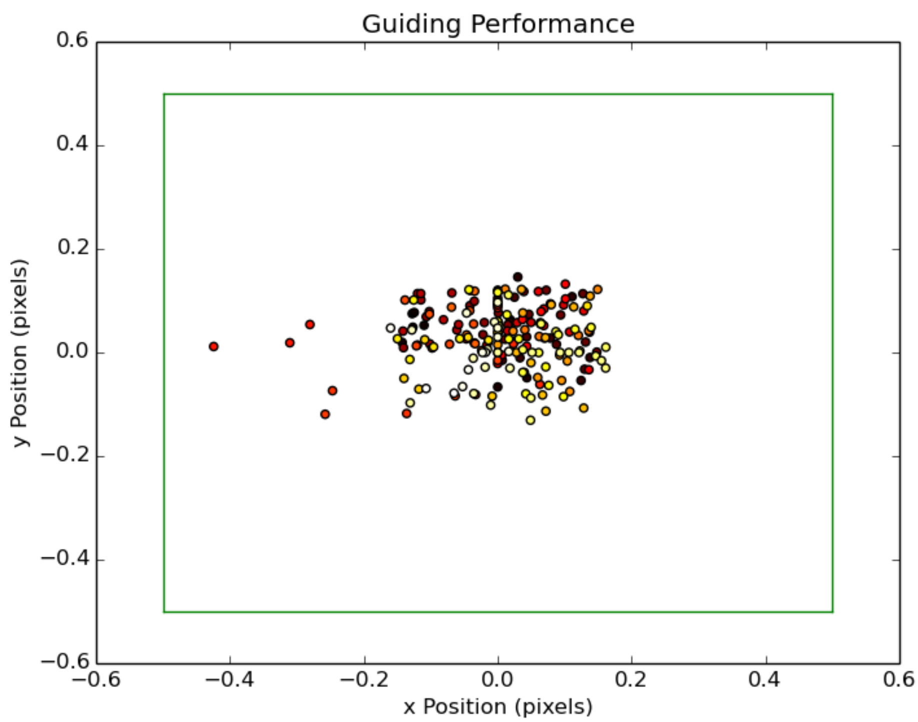

Figure 11. 18-inch Telescope Guiding Performance

The guiding performance of the 18-inch telescope with Argo Navis tracking, and PHD2 guiding; the telescope is able to keep a source confined to a single pixel, marked with the green box. The color change of the data points denotes the passage of time, from darker to lighter colors over the course of 12 minutes.

1.2.2.2.1.4 Infrared Camera for Astrophysical and Cosmological Transients Interface (ICACTI)

An InGaAs detector was tested on the 18-inch and 12-inch telescopes at ASU to determine its effectiveness in astronomical research (Strausbaugh, Jackson, and Butler 2018), and as a possible component in a ground based telescope array. The unique demands required for scientific work render the software provided by the InGaAs camera manufacturer insufficient. Not only does the camera need to continuously take data, but that data needs to be simultaneously uploaded and saved to memory. As a novel code must be written, a data pipeline can be constructed to reduce, stack, and analyze the data as well. The code created to interface with the camera, Infrared Camera for Astrophysical and Cosmological Transients Interface (ICACTI), is written in Python.

ICACTI can operate in two different ways. The first way utilizes the internal triggering and timing of the camera and is used for data acquisition. The second way uses an external source to trigger the exposures and determine the exposure time; this method was used in laboratory testing of the camera, and may be later implemented to drive down the read noise of the detector.

ICACTI runs as a neatly packaged graphical user interface (GUI), with appropriate buttons for initializing the link between the computer and the camera, taking dark images, setting the exposure length and program run time, and collecting data. There are toggle options for turning on and off image display and saving the data to file. The program can display the most recent image collected, so that the user can be confident that the source is still in frame.

When internally timed, each exposure lasts only 16.7 ms; the data from this exposure is saved to a buffer on the camera. This buffer is then accessed by the program through a datalink cable, and the buffer is saved to an array.

To increase the sensitivity of the camera, many images are stacked on top of each other, allowing fainter objects to be seen. This is achieved by adding the digital counts on each specific pixel together, continuously adding to the array of data.

These arrays are stacked on one another for 1 second as the default, resulting in a stack of 60 images. Then the data is rescaled and saved to a fits file, so that it may be used at a later time. Written into the header of the fits files is important information about the given exposure, such as its start and stop time and the temperature of the camera during the exposure.

This process is repeated for the desired duration of observation, which could be on the order of several hours for the transit of an exoplanet around its host star. Each individual 16 ms exposure is not saved due to data storage constraints. Exposures longer than one second can be used to ease data storage issues, as well as identify dimmer sources in the frame.

Figure 12 displays a screen shot of the GUI at work. The right window is the GUI itself, with all of the interactive buttons displayed. The upper left window is a terminal readout of the actions of the GUI. The bottom left window is a display of the most recent image taken, with a histogram of digital counts across the pixels on the sensor included.

External triggering needs to be employed to accurately measure the dark current for the camera during cooling and is used to determine the read noise. Cooling the camera and taking data with internal timing leads to suppressed zeros in the data. When the camera reaches a low enough temperature, instead of rescaling the data,

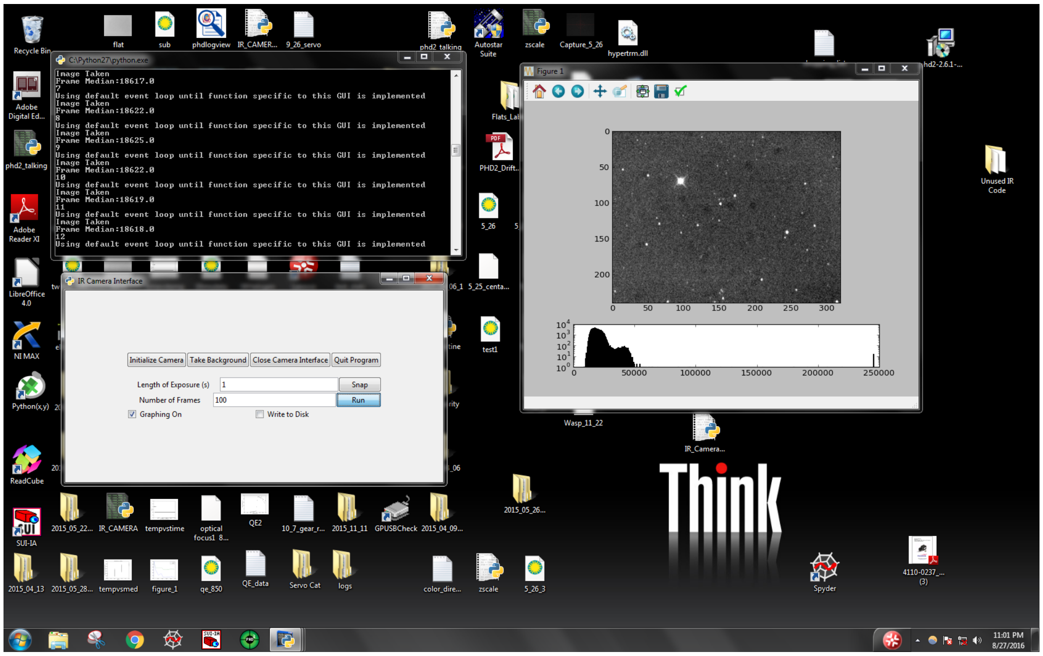

Figure 12. ICACTI GUI

A screen shot of the ICACTI GUI in operation, with the read out and reduced image in separate windows.

the internal processing on board the camera sets the digital count to zero, meaning data is lost.

The camera can be externally triggered by a signal generator. In this way, the gain can still be kept at its most sensitive setting, 5 $e^{-}/count$, but the exposure time can be lengthened, eliminating the suppressed zeros.

1.3 Transient Identification Software

Novel data reduction and analysis techniques are being developed, and will have to be refined for rapid identification of new transient sources. The use of machine learning is revolutionizing the field of rapid source detection (e.g., Narayan et al.

2018). Going through the data stored by astronomical surveys will require efficient data mining procedures (e.g., Borne et al. 2008).

1.3.1 Image Subtraction

The main technique for discovering explosive transients (e.g., SNe and GRBs) is to perform image subtractions. Archived images of the sky are used as a template, and an image of the same part of the sky after an event (perhaps triggered by a GCN alert) is used as a science frame. The source is not always apparent in the science frame as foreground stars or the host galaxy could obscure the target. Subtracting the archival data from the science frame can reveal the transient source. Source identification using image subtraction techniques focuses on hypothesis testing models (specifically testing the null-hypothesis: is the source variable?).

High Order Transform of PSF And Template Subtraction (HOTPANTS, Becker 2015) remains the standard for image subtraction software, and many data reduction pipelines (Palomar Transient Factory (N. M. Law et al. 2009), Deeper Wider Fast program (Andreoni et al. 2017), Pan-STARRs (Kaiser et al. 2002), Dark Energy Survey (Morganson et al. 2018), to name a few) make use of the software.

1.3.2 Machine Learning Light Curve Analysis

Studying the light curves of sources, instead of the image subtraction frames, allows for binary testing (i.e. is this a constant or variable source?) (e.g., Pashchenko, Sokolovsky, and Gavras 2018). Non-linear testing opens up the possibility to test other machine learning algorithms (e.g., random forests and neural nets).

These different techniques may find additional sources missed by image-subtraction detection algorithms. In Pashchenko, Sokolovsky, and Gavras 2018, 13 additional variable sources were detected from a catalog of about 200 known sources using non-linear machine learning algorithms. Knowledge of missed events can be used to help improve real-time transient detection algorithms, or at the very least, provide a metric for the accuracy of those algorithms.

Several science cases warrant a light curve analysis machine learning algorithm. The first orphan afterglow was detected by mining archival radio data (C. J. Law et al. 2018), and mining archived survey data could uncover more orphan afterglows. Sources that are not strong candidates in an image subtraction – variable stars and exoplanet transits – could also be discovered by mining light curve data.

Machine learning algorithms need sample data for training, and so trying to discover as yet unobserved phenomena, such as an optical detection of an orphan afterglow, is challenging. Using simulated data to train a machine learning algorithm to detect orphan afterglows is one possibility. An alternate strategy would be to make use of the wealth of afterglow data already available to us. We can use existing afterglow data, and instead of using all of the data from immediately following the burst, we instead use data from when the afterglow is several hours to days old. This would accurately simulate the type of afterglow that would be detected in a transient survey, with no prompt emission to initiate observations.

Surveys have used light curve analysis to detect transiting exoplanets. The Kepler (Borucki et al. 2010) and Transiting Exoplanet Survey Satellite (Ricker et al. 2010) both use automated programs to identify transiting exoplanets.

Citizen scientists can be trained to identify exoplanet transit light curves (e.g., Fischer et al. 2012; Mahabal et al. 2011). Amateur scientists can identify sources that were missed by machine learning algorithms, can help train algorithms, and can test against false-positives. The most famous example of what citizen scientists are capable of is the discovery of Tabby's Star (Boyajian et al. 2016), whose asymetric, aperiodic lightcurves exhibit dips of up to 20%. This unprecedented behavior did not fit within the parameters of the exoplanet light curve detection algorithms, and so was not flagged as a potentially interesting source, but it was noted by citizen scientists and followed up by astronomers. It will be interesting to see what role citizen scientists can play in future transient surveys.

Chapter 2

NIGHT VISION FOR SMALL TELESCOPES

2.1 Abstract

We explore the feasibility of using current generation, off-the-shelf, indium gallium arsenide (InGaAs) near-infrared (NIR) detectors for astronomical observations. Lightweight InGaAs cameras, developed for the night vision industry and operated at or near room temperature, enable cost-effective new paths for observing the NIR sky, particularly when paired with small telescopes. We have tested an InGaAs camera in the laboratory and on the sky using 12 and 18-inch telescopes. The camera is a small-format, 320x240 pixels of 40μm pitch, Short Wave Infra-Red (SWIR) device from Sensors Unlimited. Although the device exhibits a room-temperature dark current of 5.7×10^4 $e^{-}s^{-1}$ per pixel, we find observations of bright sources and low-positional-resolution observations of faint sources remain feasible. We can record unsaturated images of bright ($J = 3.9$) sources due to the large pixel well-depth and resulting high dynamic range. When mounted on an 18-inch telescope, the sensor is capable of achieving milli-magnitude precision for sources brighter than $J = 8$. Faint sources can be sky-background-limited with modest thermoelectric cooling. We can detect faint sources ($J = 16.4$ at 10σ) in a one-minute exposure when mounted to an 18-inch telescope. From laboratory testing, we characterize the noise properties, sensitivity, and stability of the camera in a variety of different operational modes and at different operating temperatures. Through sky testing, we show that the (unfiltered) camera can enable precise and accurate photometry, operating like a filtered J-band detector,

with small color corrections. In the course of our sky testing, we successfully measured sub-percent flux variations in an exoplanet transit. We have demonstrated an ability to detect transient sources in dense fields using image subtraction of existing reference catalogs.

2.2 Introduction

The near-infrared (NIR), and particularly the short-wave-infrared (SWIR, 750 – 2500 nm), are important wavelength bands in astronomy. There are several advantages to working in these wavelengths. NIR light scatters off interstellar dust at a much lower rate than visible or ultraviolet light, because NIR wavelengths are much longer than the average size of interstellar dust particles (Glass 1999). The redshifted NIR light that reaches us from cosmological distances probes the physics at shorter wavelengths in the rest frame unlike short wavelength light that would be absorbed by the intergalactic medium. Also, many sources of astrophysical interest (e.g., low mass stars) are intrinsically quite red.

We are interested here in the potential uses of SWIR detectors on small telescopes to study transient astrophysical objects. In the specific arena of time domain astronomy, there are several science cases for which NIR observations are advantageous. Exoplanet transit light curves are likely to be more sharply defined in the NIR due to the effects of limb darkening (Neilson and Lester 2011b; Howarth 2011b), making them easier to identify. The study of exoplanets around smaller, cooler stars (M-type and Brown Dwarfs) is also optimal while operating in the NIR (Osterman et al. 2012). Type Ia supernova light curves appear to be more standard in the NIR bands than at visible wavelengths (Friedman et al. 2015; Mandel, Narayan, and Kirshner 2011). Gamma-ray

Burst (GRB) afterglows have their peak brightness in the NIR, and they tend to fade more slowly in this regime (van Eerten 2013; Rau et al. 2004; Littlejohns et al. 2014). Finally, the electromagnetic counterpart to gravitational waves from neutron star mergers should have a characteristic NIR signature (Tanvir et al. 2013).

There are natural limitations for NIR observations. The terrestrial sky is very bright in the NIR, due to emission from particles, namely hydroxil (OH^-), in the atmosphere (Sivanandam et al. 2012). As such, ground-based IR astronomy tends to be noise-limited by sky background. This suggests an interesting instrument design path that utilizes inexpensive or off-the-shelf detectors, with higher-than-typical noise properties as compared to state-of-the-art detectors, because the detector noise can still be driven below the limiting sky noise in some situations. We explore the implications for small telescopes, in particular, below. Even when sky noise is not the limiting noise source, as in the case of very bright sources like exoplanet transits, detector stability and stability of the variable night sky in the NIR become key considerations.

Astronomers have characterized well the NIR sky brightness, with expected magnitudes of $J = 16.6$ per $arcsec^2$ and $H = 15.5$ per $arcsec^2$ (Persson et al. 2002). It is possible to decrease the resulting sky background by utilizing narrow filters that sit in wavelength space between bright sky lines, which are also highly-time-variable. The FIRE spectrograph on Magellan has achieved a mean inter-line sky continuum level of $Y = 20.05 \pm 0.04$, $J = 19.55 \pm 0.03$, and $H = 18.80 \pm 0.02$ (stat.) ± 0.2 (sys.) mag arcsec^{-2} (Sullivan and Simcoe 2012). A narrow Y-band filter could exploit one of these gaps (at 960-1080 nm), providing an uninterrupted window for observations (Choi et al. 2012). We note that all magnitudes presented in this paper are in the AB system.

The quantum efficiency (QE) of conventional silicon-based CCD detectors breaks down at wavelengths beyond 1000 nm (Sullivan, Croll, and Simcoe 2013). The current standard for IR astronomy are HgCdTe detectors. These detectors must be cryogenically cooled to decrease detector dark current to acceptable levels and to permit stable readout. Astronomical instruments using these detectors tend to be both expensive and heavy. A different semi-conductor, InGaAs (useful for 700-1700 nm, Pearsall and Hopson 1977; Pearsall, Quillec, and Pollack 1979), covers the shorter end of the NIR bandpass (Figure 13; Norton 2002). These detectors, which have become commercially available as a result of night vision industry, have decent noise properties at room temperature. InGaAs detectors are cheaper to obtain than HgCdTe detectors, although the available format is currently smaller. Depending on the application (and on the sky brightness per pixel in particular), there is the possibility of operating at relatively high temperature, at or near room temperature.

In this study, we characterize a commercially available SWIR camera from the Goodrich corporation in both laboratory and on-sky settings with small telescopes and realistic observing conditions. Below, we show the results of the laboratory testing, including dark rate (and its behavior with temperature), gain, read noise, QE, linearity, and charge persistence. We also present the results of testing the InGaAs detector on the sky. We show the detector's photometric precision, its color (comparing J band to Y and H bands), and finally present a light curve of HD189733, which shows the predicted dip caused by a known exoplanet transit. Having presented these results, we show that we can account for the noise present in our system by accurately modeling the statistical sources of noise. Using our model for noise, we put limits on what sources we can study.

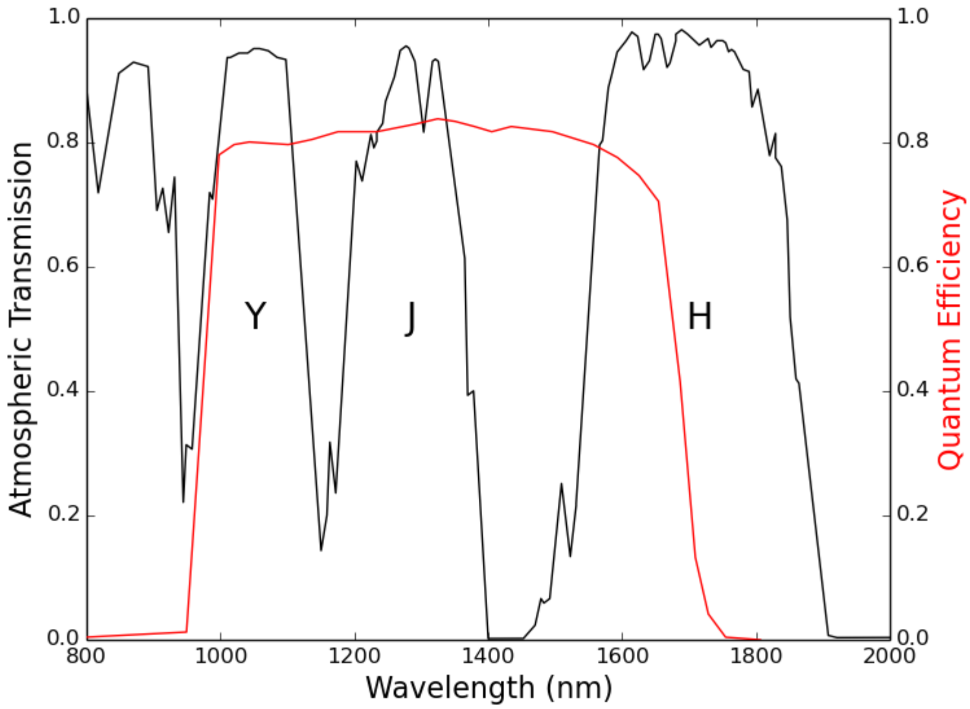

Figure 13. Goodrich InGaAs QE Curve and IR Atmospheric Transmission

An example InGaAs QE curve (from, http://www.sensorsinc.com), plotted in red over the atmospheric transmission spectra in black (from, http://modtran.spectral.com/modtran_index), with the Y, J, and H bands labeled.

2.3 Camera Description and Laboratory Testing

We have tested a small-format (320x240 pixel) Short Wave Infra-Red (SWIR) camera from Sensors Unlimited, Inc.[5], a division of UTC Aerospace Systems. The SU320HX-1.7RT is a Mil-Rugged InGaAs video camera featuring high-sensitivity and wide operating temperature range. It has a compact size ($<$ 3.8 in^3) and can be operated over a wide temperature range (-40 to 70 C) with low required power ($<$ 2.9 W at 20 C). The sensor has large pixels (40μm x 40μm) and is advertised to have

[5] http://www.sensorsinc.com

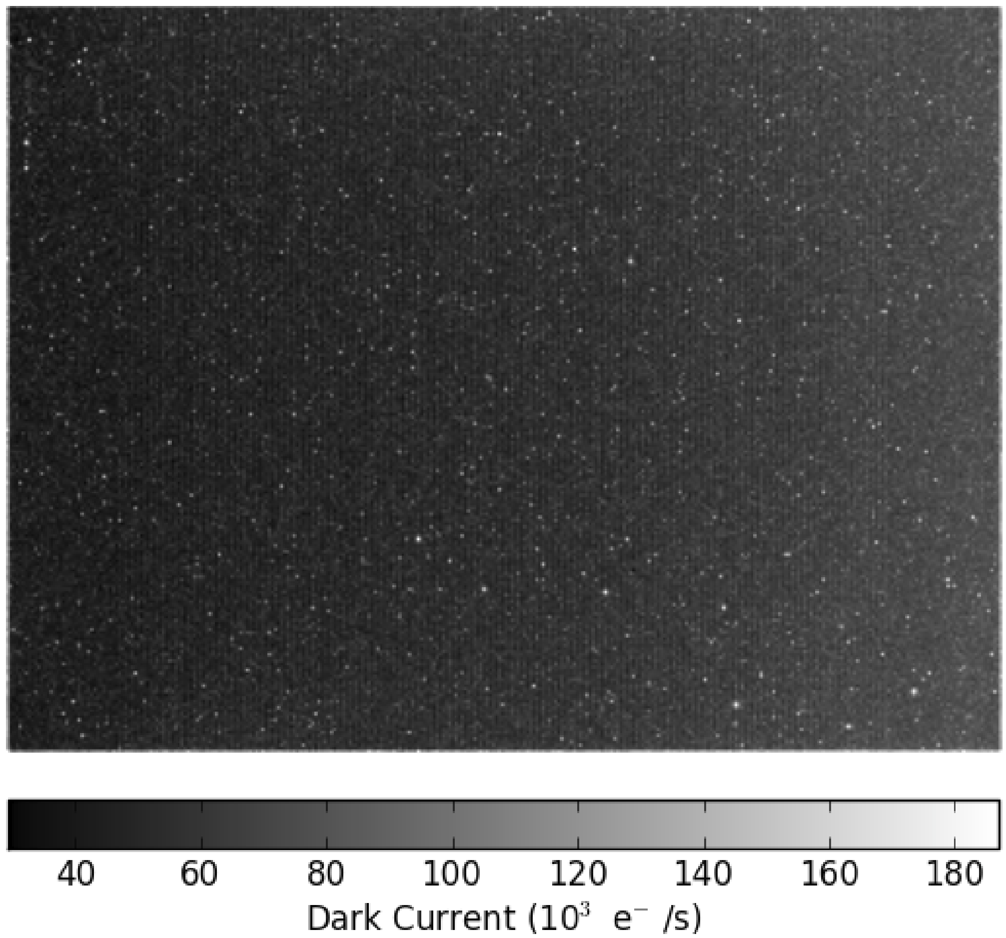

Figure 14. Goodrich Dark Frame

The visible gradient across a dark frame of the detector at 20 C, most likely due to a temperature gradient caused by the ohmic heating of the camera's electronics.

high pixel operability (> 99%) and high sensitivity (> 65% QE) from 900 nm to 1.7 μm. The full-well depth is 10^7 e^-. A built-in thermo-electric cooler (TEC) is designed to maintain a stable sensor temperature of 20 C.

The analog signal from the sensor is digitized to 12-bit data in CameraLink format. We use a frame-grabber from National Instruments (NI PCIe-1427) and the NI-IMAQ software[6] for image acquisition. Custom python scripts have been written to provide

[6]see, http://www.ni.com

a GUI and scripting interface as well as to provide real-time image visualization; this software is called ICACTI (Infrared Camera for Astrophysical and Cosmological Transients Interface) and has been made freely available[7]. We set camera modes using the serial interface and use the NI-IMAQ C libraries to store image frames in FITS format. We operate the camera in a continuous read mode of individual 16.3 ms frames which are summed into longer exposure frames as desired. The 16.3 ms frame time is found to offer an acceptable compromise: the noise floor is well-sampled while there is also sufficient dynamic range to avoid saturation due to bright stars. In the sub-sections below, we discuss laboratory measurements of the detector dark current, gain, quantum efficiency, persistence, and linearity.

2.3.1 Dark Current, Read Noise, and Sensor Gain

Blocking light to the camera, we measure a dark current at the nominal operating temperature (20 C) of $5.7 \times 10^4\ e^- s^{-1}$ per pixel (i.e., $3.6 \times 10^{13} e^- s^{-1} m^{-2}$). A variation in the dark current level is found to be present across the sensor (Figure14), similar to the pattern discussed for the device in Sullivan, Croll, and Simcoe 2013. We find that this gradient persists when the internal TEC is turned off and cannot, therefore, be due to the TEC. A likely explanation for the temperature gradient is ohmic heating due to circuitry behind the sensor.

Similar detectors have been characterized (Sullivan, Croll, and Simcoe 2013; Nagayama et al. 2014), with similar dark rates at 20 C. The camera studied by Sullivan, Croll, and Simcoe 2013 has a dark rate of $3.5 \times 10^{13} e^- s^{-1} m^{-2}$. Nagayama et al. 2014 tested an InGaAs detector with a dark rate of $6.6 \times 10^{14} e^- s^{-1} m^{-2}$.

[7] https://github.com/rstrausb/ICACTI

We have also experimented with additional cooling (Figure 15) using an external TEC mounted to the side of the aluminum camera housing. We employed a Ferrotec 3-stage Deep Cooling unit, capable of generating a $\Delta T = 111$ C temperature differential between the hot and cold side of the TEC. The entire camera was kept near 0 C in an external, cooled enclosure and insulation was wrapped around the device and 3-stage TEC. However, we did not achieve the expected 111 C temperature differential due to the lack of direct contact between the 3-stage TEC and sensor. By measuring both the signal level (dominated by dark current; Figure 15) and the signal variance in several frames captured over a range of temperatures (Figure 16), we find an inverse gain of approximately 3 e$^-$/ADU. We find a read noise of about 12 e$^-$ per 16.3 ms frame.

After moderately cooling the camera (down to -15 C), we achieve a dark current of $1.42 \times 10^{13} e^- s^{-1} m^{-2}$. Sullivan, Croll, and Simcoe 2013 and Nagayama et al. 2014 achieve a more significant decrease in the dark current after similar cooling ($1.5 \times 10^{12} e^- s^{-1} m^{-2}$ and $1.4 \times 10^{13} e^- s^{-1} m^{-2}$, respectively). We have modeled the change in dark current with respect to temperature using simple exponential functions, of the form $D(T) = Ae^{BT} + C$, where $D(T)$ is the dark current as a function of temperature, T. These exponentials are plotted as a solid green line, for the Goodrich detector, and as a solid blue line, for the Sullivan, Croll, and Simcoe 2013, in Figure 15.

Separating the exponential and constant baseline (the dotted green components in Figure 15), demonstrates that both our Goodrich detector, and the Sullivan, Croll, and Simcoe 2013 detector have similar exponential behavior, with a large discrepancy between the constant offsets. The large constant component still present when cooling the Goodrich detector is most likely due to the fact that we did not directly cool sensor, and instead cooled the entire camera unit.

Directly cooling the sensor inside the Goodrich camera would require to disassembly of the camera. We would need to run longer wires from the electronics to the sensor, attach the TEC to the back of the sensor, and run water cooling to pull heat from the hot side of the TEC. This would all need to be enclosed in a larger aluminum case, with fans to dump heat from the water cooling system. Although not yet developed, such a scheme to apply direct cooling to the sensor would likely remove the pattern noise found in the dark frames. An external triggering device could also be housed in the new camera assembly (as motivated in Section 2.5).

Cooling the sensor directly, we expect to achieve a dark current on the order of the sky background ($\approx 6000 e^{-} s^{-}$ per pixel in J-band for the telescopes we have utilized; see Section 2.5). We can determine at which temperature this dark current will occur using our exponential fit models; however, this temperature is very sensitive to baseline level. If we assume a similar baseline to the Sullivan, Croll, and Simcoe 2013 detector, we should achieve a dark current comparable to the sky background level at $T = 0C$. Even at a baseline level several times higher than the Sullivan, Croll, and Simcoe 2013 detector, the temperature needed to achieve sky background levels in the dark current would still be well within the cooling range of the Ferrotec TEC.

We note that our inferred inverse gain value is somewhat smaller than the manufacturer's value quoted for 16.3 ms frames. This suggests some smoothing present in the analog-to-digital conversion. By calculating the autocorrelation between subsequent frames on a pixel-by-pixel bases, we determine that approximately 15 subsequent frames show signs of correlation. We expect that this smoothing is due to the capac-

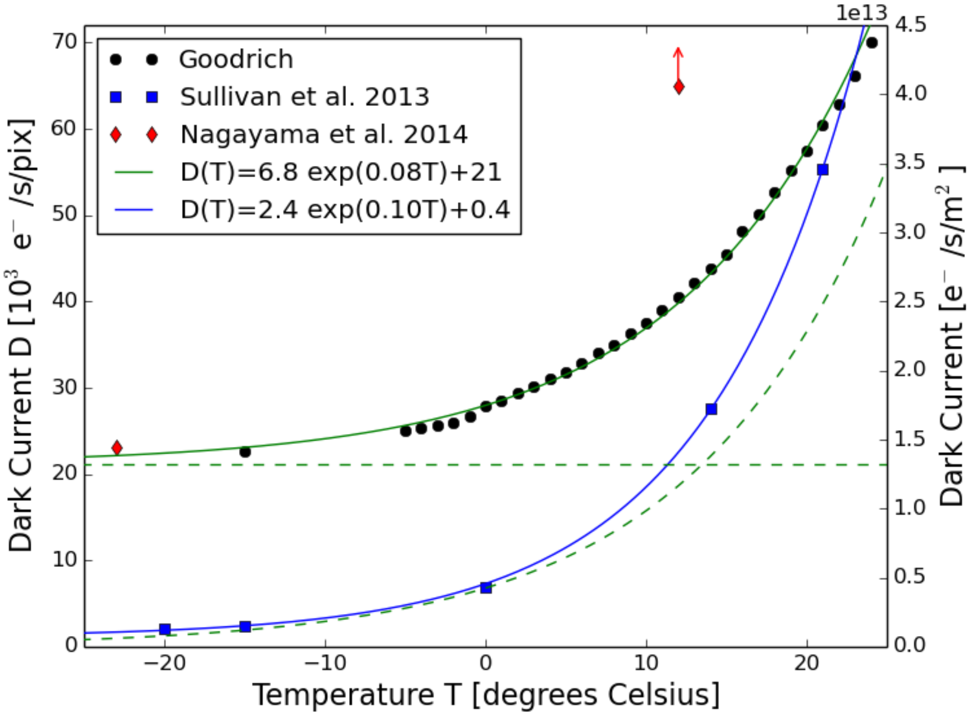

Figure 15. The Effect of Temperature on the Dark Current of the Goodrich InGaAs Detector

The effect of temperature on dark rate, utilizing an external 3-stage TEC. The units on the right side y-axis denote the per pixel dark rate if each detector had the same sized pixels (40 μm $\times$ 40 μm). The left y-axis shows the dark rate in terms of area instead of pixels, so that the different detectors can be directly compared.

itors present in each pixel read-out. Our measurements of all astronomical sources below were conducted using 1 s integration sums of the 16.3 ms frames, sufficiently long enough to average over this capacitive smoothing. We estimate that the effective inverse gain in a 16.3 ms frame is approximately 5 e^-/ADU.

Using Figure 16, we are also able to determine the read noise of the detector. Using the y-intercept, and converting to appropriate units, the read noise corresponds to 12 $e^- frame^{-1}$ (90 $e^- s^{-1}$).

Finally, we note that cooling the InGaAs detector strongly comes at a price: the

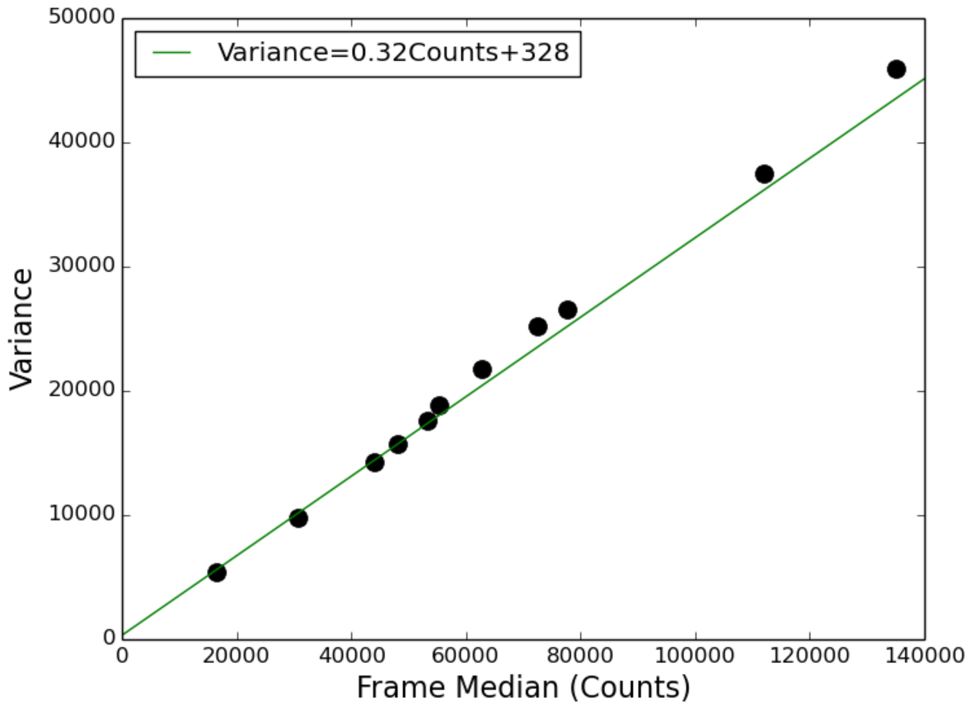

Figure 16. Goodrich InGaAs Detector Variance and Signal Relationship

The relationship between variance and signal is plotted, with the equation describing the fit shown.

sensitivity to longer wavelength light is degraded for InGaAs (e.g. Figure 4-8[8]. The sensitivity lost by this detector would occur in the H-band, where the sky brightness level is high, perhaps making the loss of sensitivity at longer wavelengths acceptable.

2.3.2 Quantum Efficiency, Persistence, and Linearity

We confirmed the advertised QE of the camera (Figure 13) by measuring monochromatic light with both the Goodrich camera and a photo-electric diode, with known

[8]https://www.hamamatsu.com/resources/pdf/ssd/infrared_kird9001e.pdf

responsivity. We measure a QE of $> 80\%$ between 950-1050 nm and $> 60\%$ between 1050-1700 nm. This wavelength range encompasses the entire J-band and most of the H-band with moderate efficiency ($> 60\%$), and importantly, the very clean Y-band at high efficiency ($> 80\%$).

The effects of charge persistence can be important for time domain astronomy, in particular. To quantify the persistence, while the detector was collecting data, a light source was turned on and off. We fit exponentials to this data, resulting in a time constant of 23.9 ms for exponential growth (when the light was turned on) and 16.5 ms for decay (when the light was turned off). These time scales are on the order of the individual frame time (16.3 ms) and are likely to be much shorter than any natural timescales for typical astrophysical transients.

We also tested the linearity of our detector to ensure it was suitable to study the wide range of magnitudes inherent in transient astronomy: from bright stars hosting exoplanetary systems, to dim and distant SNe and GRBs. The Goodrich detector exhibits a linear response over a range of 10 e^- per pixel to 3×10^6 e^- per pixel (a dynamic range of $> 10^5$).

2.4 Sky Testing

In order to verify our laboratory device characterization just discussed, we conducted a number of on-sky imaging campaigns (Table 1). In addition to confirming device properties utilizing a noise model for sources detected by the camera, which we explore in Section 2.5 below, there were two major goals of these campaigns: (1) to conduct proof of principle observations of both very bright sources and faint sources near the noise floor of the device, and (2) to observe a sufficient number of field stars to allow for the photometric characterization of the camera in terms of flux and color accuracy.

We mounted the Goodrich camera on an 18-inch ($f/4.5$) and 12-inch ($f/10$) telescope and conducted sky testing from a roof top on ASU's campus in Tempe, Arizona. The sensor has a plate scale of 4.0 arcseconds/pixel on the sky on the 18-inch telescope, with a field of view of 21.4 x 16.0 arcmin2. The sensor has a plate scale of 2.7 arcseconds/pixel on the 12-inch telescope, with a field of view of 14.4 x 10.8 arcmin2. Due to the large size of the camera's pixels on the sky, it is sometimes true that the entire full width at half maximum (FWHM) of a star is contained in a single pixel. At site with better seeing, this is likely to be a common occurrence. Single pixel source monitoring could be useful for some high-precision photometric applications which seek to mitigate the effect of intra-pixel and pixel-to-pixel gain variations.

The 18-inch Newtonian telescope, manufactured by JMI, features a highly stable, 36 inch split ring polar mount. The primary mirror and secondary diagonals used for telescope are supplied by Galaxy Optics (Buena Vista, CO), which produce high quality, large diameter Newtonian mirrors. It is a precision annealed, 2 inch thick pyrex primary mirror floated on 18-points, which provides even support and prevents pressure areas leading to distortion. The mirrors are manufactured to yield RMS wavefront errors below that of the diffraction limit. The optical coating are custom fit to be effective in the IR band, with a $< 1/100$ wave center to thickness variation and mirror reflectivity of 98%. The 12-inch telescope is an LX-200 Cassegrain telescope from Meade.

Data for the sky tests was collected and saved from the camera using the acquisition software (Section 2.3). The data were then analyzed using a pipeline similar to the one used for RATIR (Reionization And Transients Infrared/Optical camera; Littlejohns et al. 2015), as follows. Images were first reduced using flat-fielding algorithms in Python. Stars in the reduced images are found using Source Extractor (Bertin and Arnouts 1996), and images are aligned based on those star locations using astrometry.net (Lang et al. 2010). These aligned images are then stacked using SWARP (Bertin 2010). Finally, photometry is obtained using Source Extractor on the stacked images.

The results of running our pipeline on data collected for the fields of the galaxy Centaurus A and HD189733 are shown in Figures 17 and 18, respectively. Additional information about the data from these fields, as well as the field HAT-P-36, are shown in Table 1.

Table 1. Summary of Astronomical Fields Observed for On-Sky Testing of InGaAs Detector

Figure Label	Target	RA (center) Dec (center)	Start Time (UTC) End Time (UTC)	Effective Exposure Time (s)	Telescope
2013_10_29	HD 189733	$20^h00^m30.189^s$ $+22°43'26.867"$	2013-10-30T03:24 2013-10-30T04:55	463	12-inch Meade
2016_02_16	Centaurus A	$13^h25^m37.200^s$ $-42°59'44.160"$	2016-02-16T10:28 2016-02-16T13:20	8198	12-inch Meade
2016_04_14	HAT-P-36	$12^h33^m35.204^s$ $+44°55'00.796"$	2016-04-15T05:21 2016-04-15T09:46	14610	18-inch JMI
2016_04_26	HAT-P-36	$12^h33^m15.343^s$ $+44°53'26.867"$	2016-04-27T04:41 2016-04-27T08:33	12245	18-inch JMI

Additional information for the data plotted in Figures 17-24.

We targeted HD189733 and HAT-P-36 as they are known to host exoplanets. Centaurus A was imaged a week after the detection of SN2016adj (Marples, Bock, and Parker 2016). Despite blending with a nearby ($J = 10.8$ mag) star, image subtraction with HOTPANTS (Becker 2015), using a convolved 2MASS J-band archival image as a reference, reveals the $J \sim 13$ mag supernova (Figure 17).

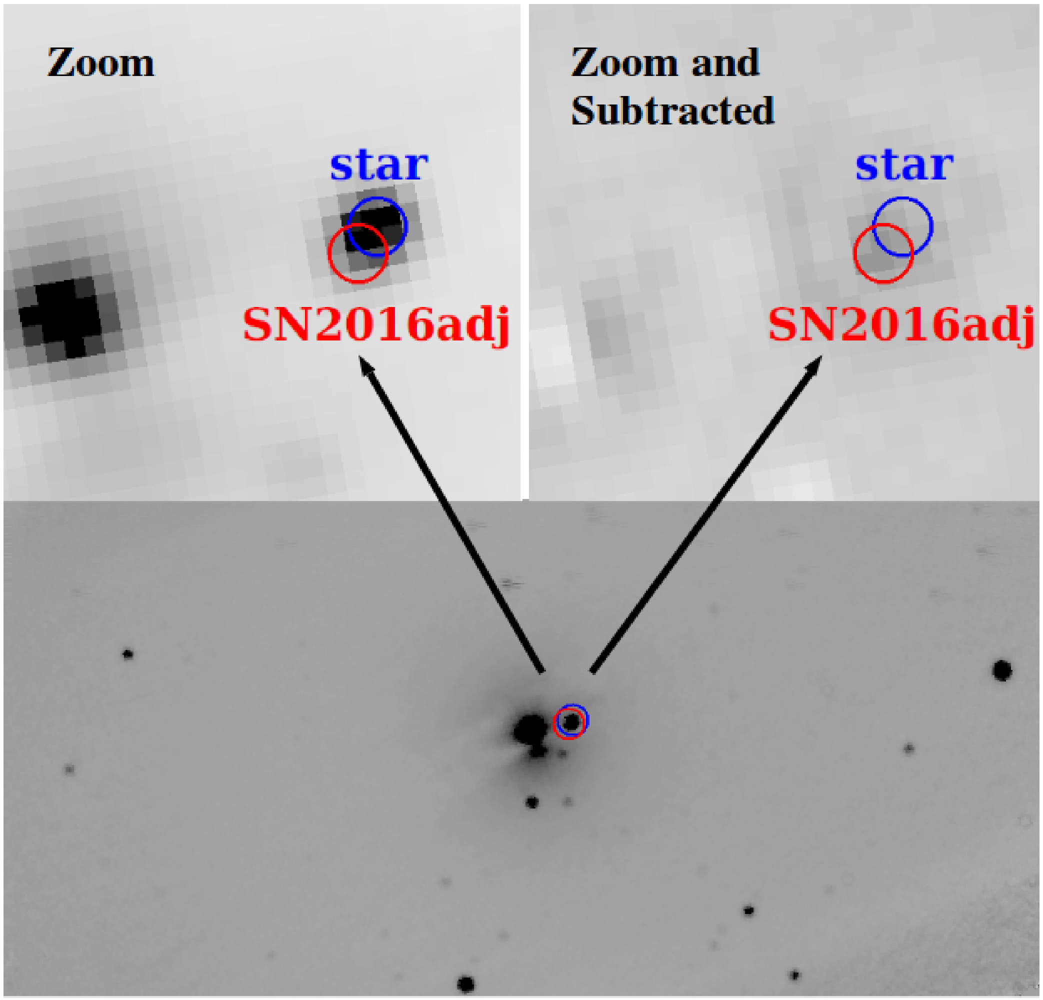

Figure 17. Centaurus A and SN2016adj Captured by the Goodrich InGaAs Detector

The field of Centaurus A, the host galaxy for the recent supernova, SN2016adj. The images at the top are a zoom on the region of SN2016adj, and an image subtraction of the same zoomed area of the sky. The image subtraction removes the foreground star, revealing SN2016adj.

We collected the HD189733 data on the 12-inch telescope before the 18-inch telescope was operational. The Centaurus A data were collected on the 12-inch telescope due to the galaxy's location on the sky and the fact that it would have been challenging to point our 18-inch telescope that far South.

In the following sub-sections, we use the data from HD189733, Centaurus A, and

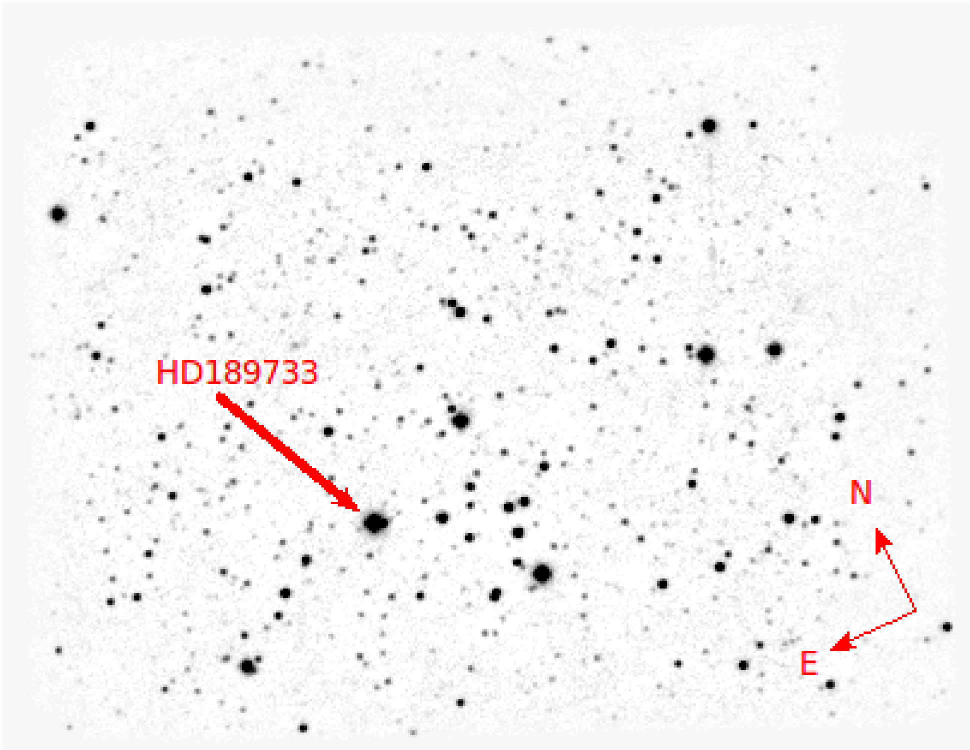

Figure 18. Field of transiting exoplanet HD189733b capture by the Goodrich InGaAs Detector

The field containing the exoplanet orbiting HD189733. The light curve showing a detection of the exoplanet is shown in Figure 24. Additional information for these images can be found in Table 1.

HAT-P-36 fields to determine the Goodrich camera's performance on the sky, testing its photometric performance, comparing its color to the established 2MASS (Skrutskie et al. 2006) and Pan-STARRS (Chambers et al. 2016) catalogs, and determining a color correction term to compare our broadband results to these filtered catalogs. We are able to detect exoplanet transits, as evidenced by the dip in the lightcurve of HD189733 (Figure 24), associated with the transit of exoplanet HD189733b.

2.4.1 Photometric Performance

We obtained photometry from as many stars from the HD189733, Centaurus A, and HAT-P-36 fields as possible. In Figure 19, we have plotted the apparent magnitude of the fields stars against their respective errors.

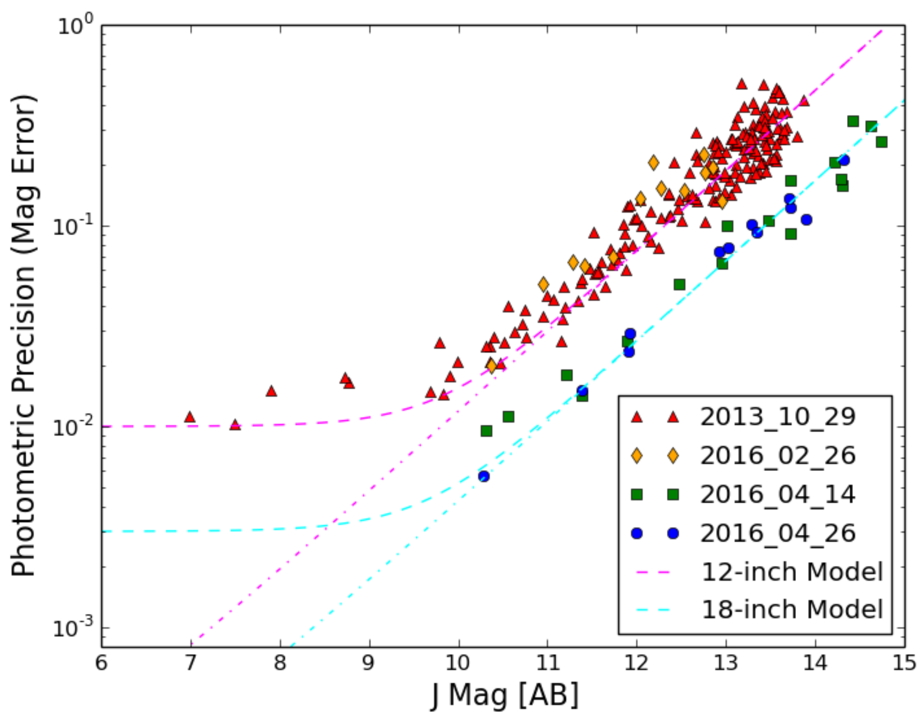

Figure 19. Goodrich InGaAs Photometric Precision

The photometric errors of detected stars compared to a model of statistical noise, described in Section 2.5; the dashed line shows a model with a systematic error term, and the dot-dashed line shows the same model without the systematic term. The observations on these nights are detailed in Table 1.

The theoretical curves plotted in Figure 19, modeling the 18-inch and 12-inch telescopes, are calculated in Section 2.5. We note that the models closely match the data, and as such we can use these models to predict whether an exoplanet transit will be visible for stars of a certain magnitude.

Following the dot-dashed curve for the 18-inch telescope in Figure 19 to brighter sources, we find that milli-magnitude precision should be possible for stars brighter than $J = 8$.

2.4.2 Color Correction

If the camera is used without a bandpass filter, as it was in the sky testing presented in this paper, a color-correction term may be needed to compare the measured magnitude of sources to the J, H, and Y band measurements from established catalogs. We compare our data from the nights described in Table 1 to catalogs from 2MASS for J and H bands, and Pan-STARRS for Y band. There are no Pan-STARRS data, however, for the Centaurus A field, as that survey did not collect data south of declination -30 degrees.

Comparing our magnitude to the J and H bands from 2MASS yields a color term of -0.05$\pm$ 0.03 (Figure 20). This small color correction term demonstrates that the bulk of light collected by the camera is in the J-band, with a small fraction of light in the H-band.

The overall photometric accuracy is plotted in Figure 21. Including the color term derived above, the photometry is accurate (within the error bars) for both bright ($J \leq 12$) stars and fainter stars where the uncertainties are large.

There is also potentially a color correcting in the blue due to the detector response shortward of J-band (Figure 13). Comparing our magnitudes with the J-band from

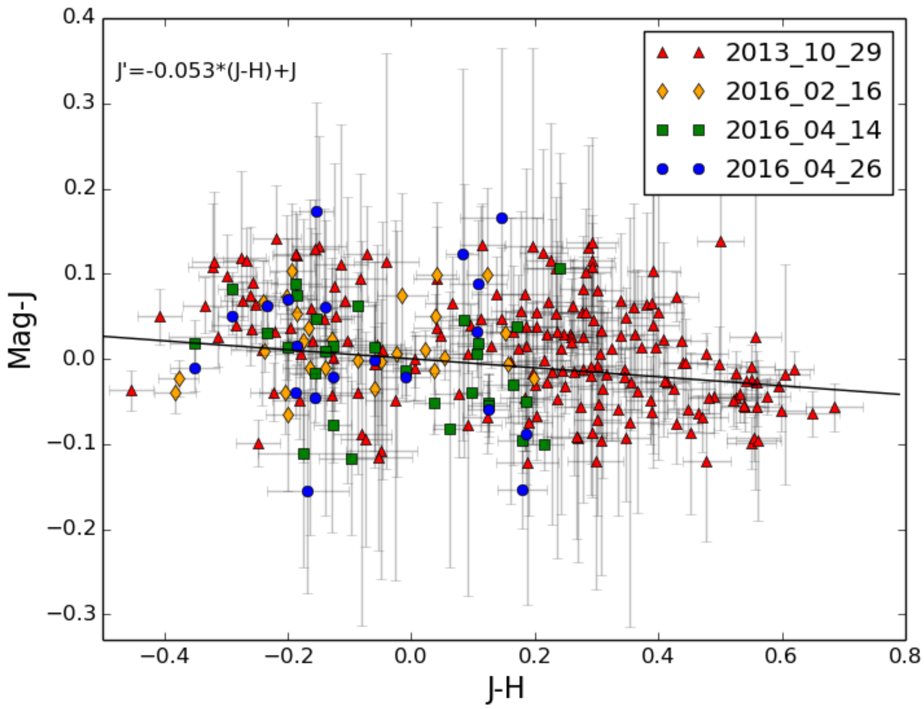

Figure 20. Goodrich InGaAs J-H Color Correction Term

A color correction term is given by the slope of the line (-0.05) through the data. This term is important for comparing our instrumental magnitudes with catalog magnitudes (J and H taken from the 2MASS catalog). J' is the expected magnitude, given J and H from the catalog and applying the color correction term.

2MASS and the Y-band from Pan-STARRS, we derive a color correction term of 0.01$\pm$ 0.03 (consistent with zero), as seen in Figure 22; the accuracy of this color correction term is shown in Figure 23.

With the small $J-H$ color correction and the even smaller $J-Y$ color correction of (-0.05 and 0.01, Figures 21 and 23, respectively), we note that our (unfiltered) camera acts very much like a filtered J-band camera. There appears to be an overall blue-ward shift in the color data when using the 12-inch telescope compared to the

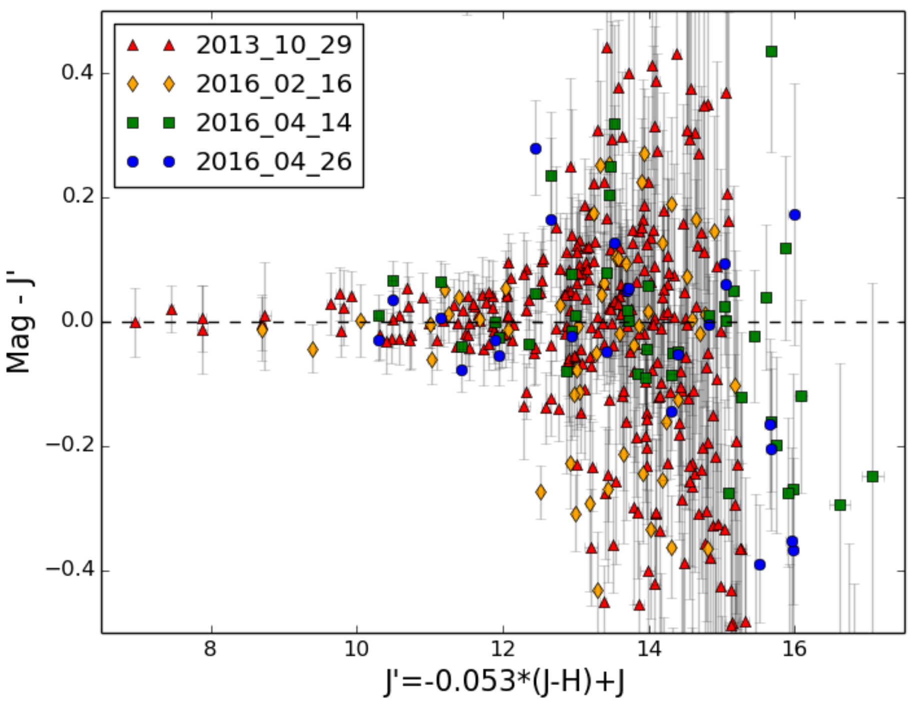

Figure 21. Goodrich InGaAs J-H Color Correction Accuracy

The accuracy of the color correction is shown by comparing our measured magnitude relative to the expected magnitude J'. The observations on these nights are detailed in Table 1.

18-inch telescope (or a red-ward shift in the 18-inch telescope compared to the 12-inch telescope) as seen in Figures 20 and 22.

2.4.3 HD189733b Transit

The exoplanet HD189733b was detected around its host star by Bouchy et al. 2005 using radial velocity measurements. It was verified spectroscopically shortly thereafter by the same group (Bouchy et al. 2005). HD189733 is a well studied system, due to

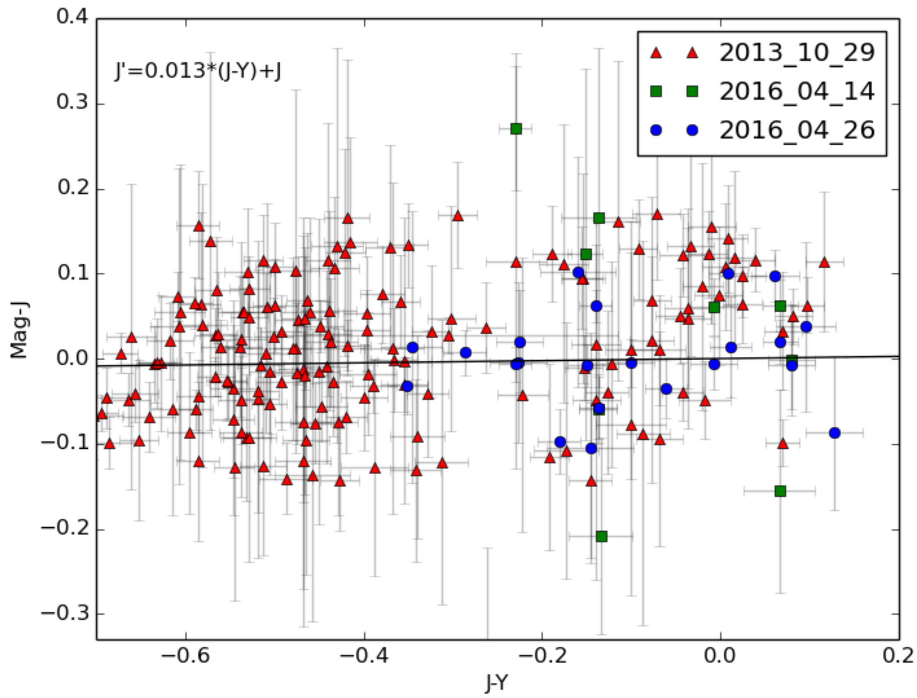

Figure 22. Goodrich InGaAs J-Y Color Correction Term

The color correction term is given by the slope of the line (0.01) through the data. This term is important for comparing our instrumental magnitudes with catalog magnitudes (J taken from the 2MASS catalog and Y taken from Pan-STARRS). J' is the expected magnitude, given J and Y from the catalogs and applying the color correction term.

the brightness of the star (J and $H \approx 7$; Skrutskie et al. 2006) and the depth of the transiting exoplanet (a $\gtrsim$2% decrease in star brightness; Bouchy et al. 2005).

Despite non-ideal conditions (bright sky, hot buildings, etc.), the latter half of one transit was recorded. Our light curve is shown in Figure 24. Additional information about this observation can be found in Table 1. Having demonstrated that we are capable of detecting exoplanet transits, we have continued to work with the Goodrich detector to obtain exoplanet light curves. Lightcurves for the HAT-P-33 system, as

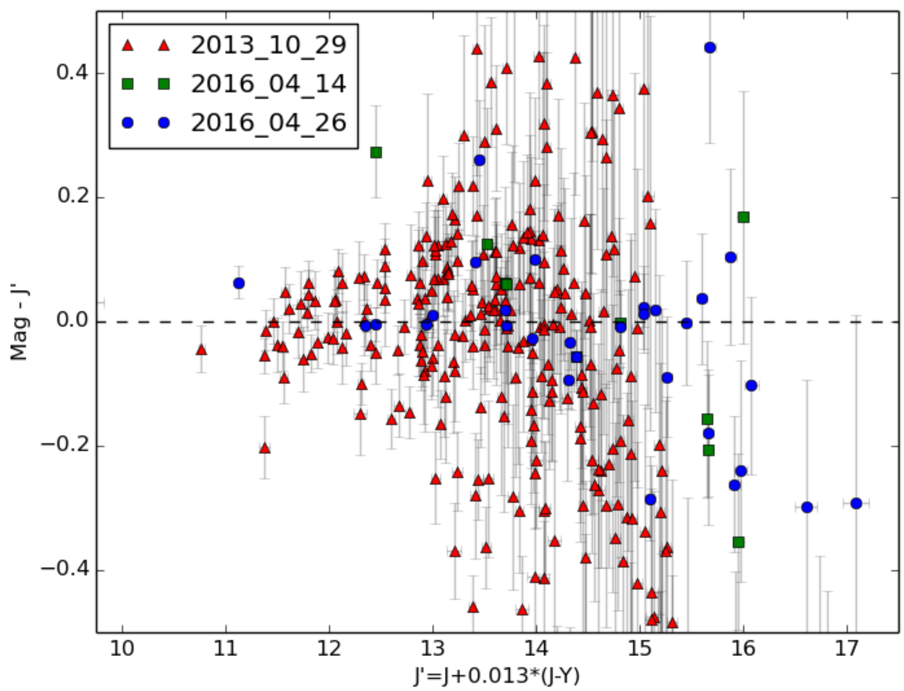

Figure 23. Goodrich InGaAs J-Y Color Correction Accuracy

The accuracy of the color correction is shown by comparing our measured magnitude relative to the expected magnitude J'. The observations on these nights are detailed in Table 1.

well as several others, will be presented, in conjunction with data taken simultaneously with RATIR, in a follow-up paper.

2.5 Discussion of Noise Properties

In order to characterize the quality of our data acquisition and to allow for future observation planning, we must understand the sources of noise for our detector. Equation 2.1 summarizes the expected signal-to-noise ratio (S/N) as a function of sources of signal in the detector:

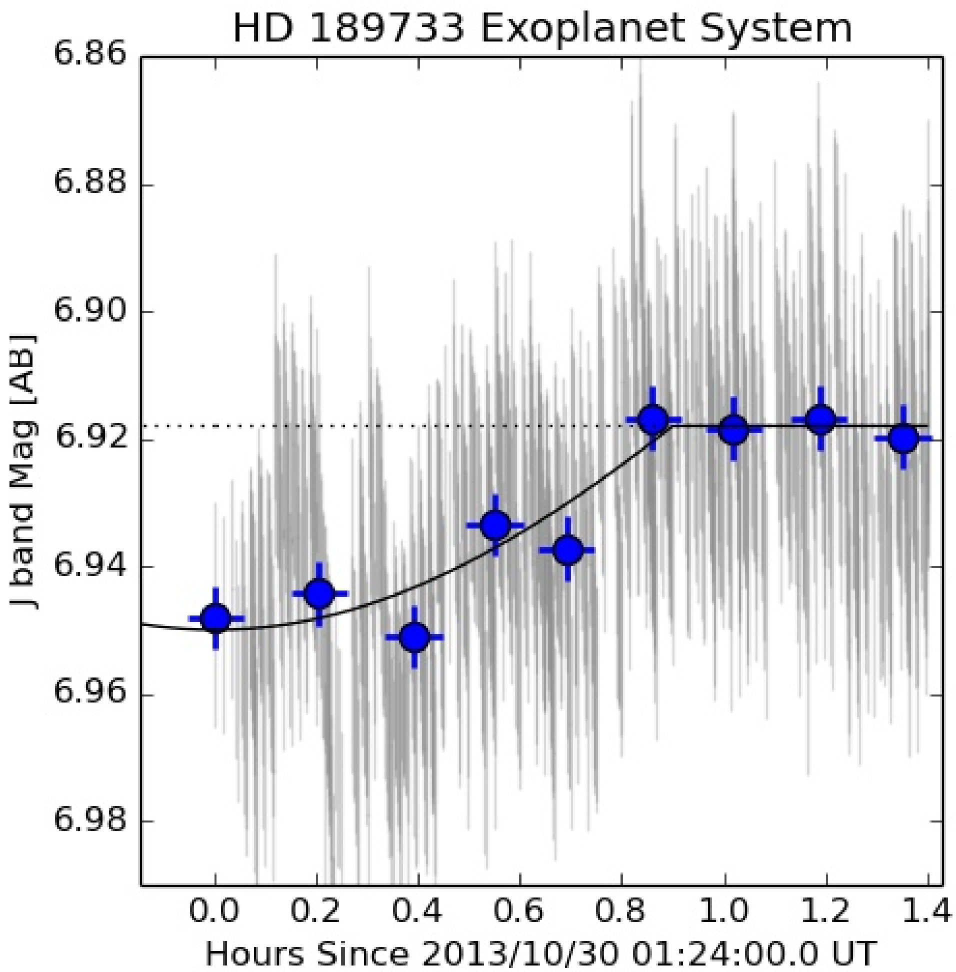

Figure 24. Light Curve of Transiting Exoplanet HD189733b captured with Goodrich InGaAs Detector

Unfiltered observation of the transit of the 7th magnitude system HD 189733. This proof of concept observation was taken with the Goodrich detector on a rooftop of a building on the Arizona State campus in Tempe, AZ. We identify the correct transit depth and end time. The data were taken with a 12 inch Meade telescope with a plate scale of 2 arcsec/pixel.

$$\frac{S}{N} = \frac{N_*}{\sqrt{N_* + n_p N_D + n_p N_S + n_p D_T + n_p RN^2 + (\sigma N_*)^2}}, \tag{2.1}$$

where N_* is the electron count from the source during the exposure time, N_D is the number of dark current electrons from the sensor, N_S is the sky brightness in electrons, N_T is the number of electrons due to the thermal emissions of the instrument (telescope, camera window, etc.), RN is the read noise, and σ is a systematic term to represent any errors that scale with the source brightness. The factor n_p is the number of pixels used to extract a source from an image. Here, we are assuming the counts (N_D, N_S, N_*, and N_T) are Poisson distributed. The read noise is squared in the noise calculation as it is a Gaussian noise source; the systematic term, with error proportional to σ, is also assumed to be Gaussian. Having thoroughly tested the camera in the laboratory and on the sky, we can now compare our observed measurement uncertainties to calculations of the noise properties, using Equation 2.1.

Assuming we cool the camera with its internal TEC ($T \approx$15 C), the dark current, N_D, is 5.2×10^4 $e^- s^{-1} pixel^{-1}$. Cooling the camera with an external TEC to $-5C$ reduces the dark rate to 2.5×10^4 $e^- s^{-1} pixel^{-1}$, as seen in Figure 15. It should be noted that we believe this is not the actual temperature of the sensor, but instead the temperature inside the camera; if we were able to directly cool the sensor, the dark should be much lower at $-5C$.

We note that the color plots in Figures 20 and 22, suggest that our detector operates almost exclusively in the J-band. Assuming the data from Las Campanas in Chile as a best case scenario, the sky background, N_S, has a level of 6600 $e^- s^{-1} pixel^{-1}$ in the J-band (Persson et al. 2002).

In Figure 15, we show that the read noise (RN in Equation 2.1) of the Goodrich detector is 12 $e^- pixel^{-1} frame^{-1}$. We currently capture data with a frame time of 16 ms, which means that 60 of these frames are added to create a one second exposure. Adding 60 frames together brings the read noise up to 90 $e^{-}pixel^{-1}s^{-1}$. This read noise is on the order of the sky background, but is much smaller than the contribution of dark noise. The level of the read noise can be reduced dramatically by externally triggering exposures for the entire one second. We have verified this in the laboratory but do not typically use external triggering in our on-sky setup.

Assuming the equipment in the experimental setup acts as a black body, the thermal noise registered by the sensor would be 4850 $e^{-}s^{-1}$ across the entire collecting area. On a pixel level, this noise, N_T, is negligible ($< 1e^{-}s^{-1}pixel^{-1}$).

The remaining sources of noise in Equation 2.1 depend on N_*, the flux from the source itself. For a source of a given magnitude, the flux can be calculated using Equation 2.2,

$$mag_{AB} = -2.5\log\left(\frac{F}{3631 \times 10^{-23}}\right) \tag{2.2}$$

where F is the flux from the source, and 3631×10^{-23} is a conversion factor from Jansky to cgi units. This flux can be converted into a signal on the detector using Equation 2.3,

$$F = \frac{h \times \nu \times g}{d\nu \times A \times QE} \times \frac{C}{dt} \tag{2.3}$$

where h is Plank's constant, ν is the frequency of light, g is the inverse gain of the camera, $d\nu$ is the bandwidth over which the observation is done, A is the collection area of the telescope, QE is the quantum efficiency of the camera and telescope together, C is the number of counts on the detector, and dt is the integration time over which the data are collected.

The inverse gain of the camera is 5 e^- per count (Section 2.3). The quantity $\nu/d\nu$ is about 0.24 in the J-band, which was the dominant color as seen in Figures 20 - 23. When the mirrors of the telescope, both primary and secondary, are taken into account, a conservative estimation of the total QE is around 20%. The two telescopes used for testing have an 18-inch and 12-inch primary mirror respectively, which is used to calculate the area, A. The quantity C/dt is either the count rate from a source of interest or is taken as the number of counts per second from the statistical sources of noise to determine limiting magnitudes.

Given the magnitude of a source, we can calculate the theoretical contribution to the noise by statistical sources, using the denominator of Equation 2.1. This is shown in Figure 19, with the "Model" curves for both the 18-inch telescope and the 12-inch telescope. The dashed line models in Figure 19 include the systematic term, σ, from Equation 2.1, while the dot-dashed line models do not include the systematic term. The data from the 12-inch telescope in Figure 19 (the red triangles and orange diamonds) show that there is systematic uncertainty preventing precision better than 10 mmag. Our sensitivity is somewhat better with the 18-inch telescope. In any case, we are confident that this systematic term is not due to the camera, but instead due to poor observing conditions (very bright sky in the Phoenix, AZ metro area). Evidence for this can be seen in Figure 15 (e.g., the right-most point in the right panel), where we demonstrate stability in the laboratory to better than 1.5 mmag.

The dot-dashed lines have been included in Figure 19 to show the precision we can expect at a darker site. The dashed line theoretical curves go through the observational data points at lower magnitudes (due to the systematic term, σ).

Optimal ground-based observations tend to be sky-noise-limited. In order for our detector to operate in a regime dominated by sky noise, the detector would need to be cooled directly, which would involve redesigning the camera housing. Following the trend seen in Figure 15, the Goodrich detector would need to be cooled to 0 C in order to have a dark signal approximately equal to sky emission. As mentioned above (Section 2.3), cooling the sensor significantly may lead to a loss of sensitivity at longer wavelengths. This trade-off could be acceptable due to the small fraction of H-band light detected, as seen in Figure 20, and the higher sky noise in the H-band.

2.6 Conclusion

We have thoroughly tested a Goodrich InGaAs detector in the laboratory and on the sky for use in transient astronomy. Our laboratory testing (e.g., Figure 15), indicates that the Goodrich detector performs similarly to previously tested InGaAs detectors. At room temperature (20 C), the Goodrich detector has a dark rate of 57,000 $e^{-}s^{-1}$ per pixel. We determined the read noise of the detector to be $12e^{-}$ per frame, and the gain of the detector to be 5 e^{-} per count (Figure 15). The QE (Figure 13) was confirmed to be between 60-90% over a wavelength range that includes Y, J, and parts of H band (900-1700 nm). Due to large pixels and highly-stable readout, the detector's response is linear over a factor of $> 10^{5}$ in dynamic range.

Through sky testing, we conclude that the unfiltered detector yields photometry comparable to a filtered J-band detector. Comparing our data to 2MASS and Pan-STARRS, we derive a $J-H$ color term of -0.05$\pm$ 0.03 (Figures 20) and a $J-Y$ color term of 0.01$\pm$ 0.03 (consistent with zero; Figure 22). We have shown that we are able to successfully model the noise present in our system (Figure 19), and using that model we can predict whether or not we will be able to study certain transient sources. By catching the tail-end of the transit of HD189733 (Figure 24), we have shown that the Goodrich camera is capable of detecting exoplanet transits and that our data-reduction pipeline is capable of extracting meaningful light curves, with better than 1% photometry, from the data. Even though under-sampled, the images are amenable to image subtraction using existing 2MASS catalog data, making possible faint source identification in potentially crowded fields (i.e., SN2016adj in Figure 17).

According to the noise model fits to our data (Figure 19), we expect to achieve milli-magnitude precision for $J < 8$ sources on an 18-inch telescope. This level of precision is achieved without any advanced dithering routines, such as the snapshot technique (Mann, Gaidos, and Aldering 2011), or any additional cooling. Implementing these would potentially push our noise ceiling down to a regime dominated by sky background. Overall, we find that mounting to smaller telescopes has the benefit of allowing for a larger area of the sky to be imaged, while also allowing for more sky background to potentially dominate the dark noise at each pixel. With the InGaAs camera mounted to a larger telescope, a finer resolution on the sky is possible; however this combination will tend to lead to a noise budget dominated by dark noise.

Based on our work with the InGaAs detector in the laboratory and on the sky, we can place limits on the brightness of sources we can study. For very bright sources, such as exoplanet transits around bright stars, we are limited by the pixel well depth of 10^7 electrons; if the well depth is achieved in a one second exposure, we can study sources as bright as $J = 3.9$, before saturation on an 18-inch telescope at a signal-to-noise level of over 3000 (0.4 mmag precision). For dimmer sources, such as distant SNe or GRBs, our thresholds are set by statistical sources of noise. In our best case scenario, we are limited by the sky background; this would require lowering our dark, by cooling the detector to $0°C$ (Figure 15). If the sky background is the dominant source of noise, we expect to be able to resolve sources of $J = 16.35$ at 10σ in a one minute exposure with the InGaAs detector mounted to an 18-inch telescope. The field of view of the detector on our 18-inch ($f/4.5$) telescope is $16' \times 21'$.

Current generation, off-the-shelf, InGaAs detectors offer a cost-effective way to study the NIR sky, as they do not need the drastic (and therefore expensive) cooling that HgCdTe detectors require. The low cost of these detectors would make them useful for compound focal planes or to enable arrays of small telescopes each with single or a few detectors. It would, therefore, be possible to build up sky coverage for monitoring multiple bright sources or for conducting wide-field, sky-limited (but relatively shallow) surveys in the NIR. Both of these science cases would benefit from the large detector pixels of the device we have studied. The large well-depth allows for monitoring of very bright sources, while the large pixels (i.e. on the sky) allow us to potentially reach the sky-background limit with modest cooling.

2.7 Acknowledgements

This publication makes use of data products from the Two Micron All Sky Survey, which is a joint project of the University of Massachusetts and the Infrared Processing and Analysis Center/California Institute of Technology, funded by the National Aeronautics and Space Administration and the National Science Foundation.

Some of the data presented in this paper were obtained from the Mikulski Archive for Space Telescopes (MAST). STScI is operated by the Association of Universities for Research in Astronomy, Inc., under NASA contract NAS5-26555. Support for MAST for non-HST data is provided by the NASA Office of Space Science via grant NNX09AF08G and by other grants and contracts.

Chapter 3

EVIDENCE FOR A BRIGHT-EDGED JET IN THE OPTICAL/NIR AFTERGLOW OF GRB 160625B

3.1 Abstract

Using deep and high-cadence gamma-ray burst (GRB) afterglow data from RATIR, we observe a sharp and achromatic light curve break 12.6 days after the GRB, accompanied by an approximately achromatic bump. Fitting of the optical, NIR, and X-ray data suggest a very narrow (2 degree) jet which remains collimated at late-time. We argue that the sharp light curve bump suggests an edge brightened jet, perhaps emitting only during a brief period of lateral jet expansion. The lightcurve also exhibits a gradual spectral evolution lasting > 10 days. The evolution of the flux can be modeled as Flux $\sim \left(\frac{t}{[20\text{days}]}\right)^{\alpha}\left(\frac{\lambda}{[800\text{nm}]}\right)^{\beta}$, with a temporal slope $\alpha = -0.956 \pm 0.003$ and a gradually time-varying spectral slope $\beta = (0.60 \pm 0.07) + (0.26 \pm 0.06)\log\left(\frac{t}{20\text{days}}\right)$.

3.2 Introduction

GRB 160625B was detected by NASA's Fermi Gamma-ray Space Telescope's γ-ray burst monitor (Meegan et al. 2009) as a one-second long pulse (Dirirsa et al. 2016). Automatic follow up by the Large Area Telescope (Atwood et al. 2009) resulted in detection of another bright, but longer lasting ($\approx$ 30 seconds) pulse about three minutes later. This later pulse peaked at a visual magnitude of 7.9, and a secondary peak exhibiting significant polarization was detected 16 seconds later by the MASTER-

IAC telescope (Lipunov et al. 2010). We focus here on late-time, afterglow data in the $riZYJH$ bands captured with the Reionization And Transients Infra-Red/Optical camera (RATIR) (Butler et al. 2012) which was presented but not thoroughly modeled in (Troja et al. 2017). Over fifty observing nights after the GRB, we are able to measure a so-called "jet break" with unprecedented cadence and sensitivity across multiple optical/NIR bands. We also study *Swift* X-ray and Ultra-Violet (UV) data captured during the same epoch.

These data potentially allow us to obtain unique constraints on the jetting of the afterglow and the possibility of lateral expansion of the jet. At early times, the high bulk Lorentz factor, $\Gamma \approx 10^3$, of the outflow permit us to view only a narrow region of angular size $1/\Gamma$ of the jet. The polarization detected by MASTER peaked at $8 \pm 0.5\%$ (Troja et al. 2017), suggestive of a jet viewing angle which is slightly off-axis. As the blast wave decelerates, more of the jet becomes visible. Once $1/\Gamma \sim \theta_{\rm jet}$, the edge of the jet becomes visible and the flux begins declining more rapidly as the energy per solid angle begins decreasing (Rhoads 1997, 1999; Rybicki and Lightman 1986). The edges of the jet come into causal contact at about this point, and the jet can potentially begin spreading laterally (see, e.g., Wygoda, Waxman, and Frail 2011; Eerten and MacFadyen 2012; Granot and Piran 2012). If the jet spreads, it can effectively halt the blast wave expansion and further decrease the afterglow flux (Rhoads 1999; Sari, Piran, and Halpern 1999; Granot et al. 2001; Wygoda, Waxman, and Frail 2011).

Detailed observations and accurate models for jet breaks are critical because they allow us to determine opening angle of the jet (Frail et al. 2001), which is crucial in turn for understanding GRB energetics (Freedman and Waxman 2001; Wygoda et al. 2016; Sari, Piran, and Halpern 1999; Kocevski and Butler 2008; Ghirlanda, Ghisellini, and Lazzati 2004; Ghirlanda et al. 2013; Amati, L. et al. 2002) and rates (Rhoads 1997; Wanderman and Piran 2010; Butler, Bloom, and Poznanski 2010; Jimenez and Piran 2013; Fenimore and Ramirez-Ruiz 2000). In addition, high-cadence observations with small error bars (as we have here) can potentially allow us to measure the energy and velocity structure of the jet (e.g., Granot and Kumar 2003; Rossi et al. 2002; Kumar and Granot 2003; Lipunov, Postnov, and Prokhorov 2001) and to constrain the hydrodynamical processes that potentially lead to a spreading jet (Sari, Piran, and Halpern 1999; Granot et al. 2001; Mao and Wang 2001; Zhang et al. 2006).

3.3 Analysis

RATIR photometry for GRB 160625B in the $riZYJH$ bands, reduced as described in (Troja et al. 2017), along with measurements reported by the it Swift UVOT and XRT are shown in Figure 25. A dominant feature in the RATIR and XRT data is an apparently achromatic temporal "jet-break" at a time of about 12 days. Interestingly, there is a slight brightening (i.e. the temporal power-law decay is less steep around the jet break than at early times) present just prior to this jet-break. The feature is present in all the RATIR bands with comparable amplitude, suggesting a color similar to that of the afterglow. The jet-break, and the brief re-brightening just before it, can be seen more clearly in the inset of Figure 25, where the RATIR data have been normalized with respect to the early H-band behavior.

The Swift XRT data (Figure 25), reduced using our automated pipeline[9], show a power-law decline in flux as $t^{-1.20\pm0.02}$ prior to the break. The spectrum, with a

[9] http://butler.lab.asu.edu/swift

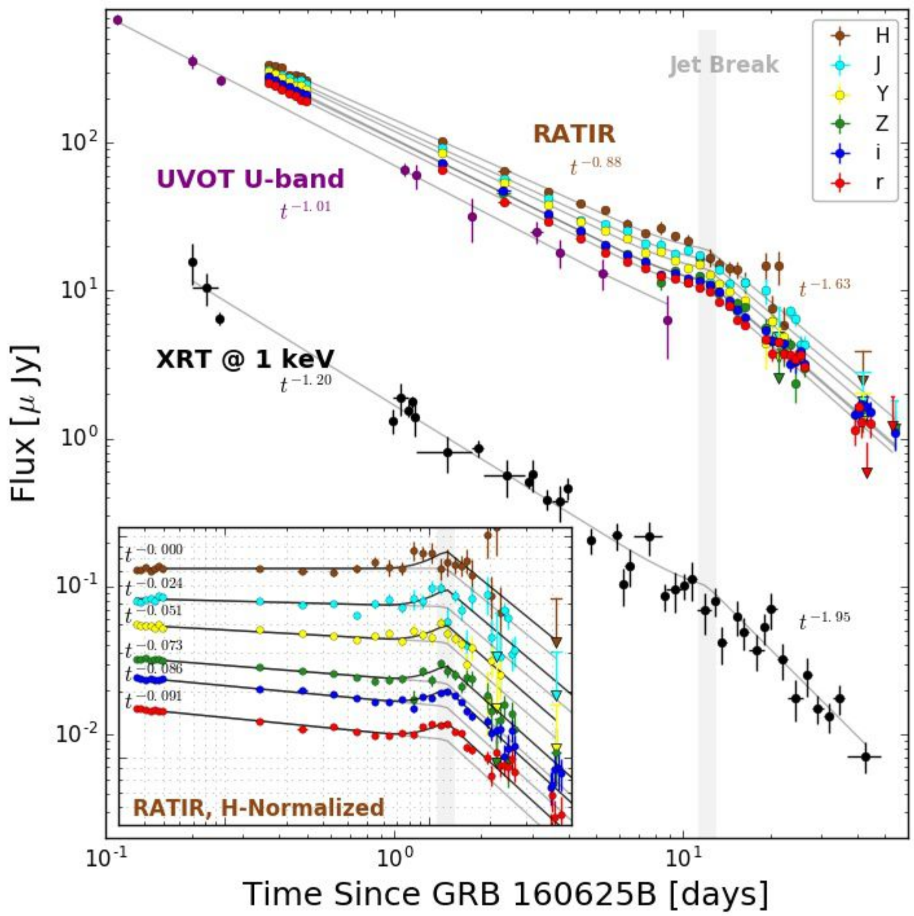

Figure 25. GRB 160625B RATIR and *Swift* Lightcurves

The afterglow lightcurve for GRB 160625B in the $riZYJH$ bands from RATIR. X-ray and UV data are from $Swift$. The inset lightcurves are normalized by the early time H-band to better display the jet break and bump. The data in both graphs are fit with the model described in Section 3.3. Additional information about the fits can be found in Table 2. The data presented in this figure can be found in Appendix A.

Table 2. GRB 160625B Light Curve Fitting Parameters

Band	θ_1	$\theta_{\rm jet}$	$B(\%)$	α_1	α_2	χ^2/ν
r	1.75 ± 0.05	2.40 ± 0.05	22.0 ± 2.1	0.971 ± 0.002	1.59 ± 0.06	1.31
i	1.90 ± 0.10	2.40 ± 0.05	18.6 ± 1.9	0.966 ± 0.002	1.64 ± 0.05	1.10
Z	2.00 ± 0.15	2.35 ± 0.05	23.4 ± 3.6	0.953 ± 0.004	1.58 ± 0.10	0.87
Y	1.95 ± 0.25	2.35 ± 0.05	17.8 ± 4.6	0.931 ± 0.005	1.73 ± 0.21	0.80
J	1.95 ± 0.35	2.35 ± 0.15	29.8 ± 9.8	0.904 ± 0.005	1.37 ± 0.16	2.91
H	1.15 ± 0.50	2.80 ± 1.10	23.3 ± 12.5	0.880 ± 0.006	2.19 ± 0.90	1.65
UV	...	...	...	1.013 ± 0.032	...	0.32
X-ray	...	2.5 ± 0.3	< 20.5 (1-σ)	1.202 ± 0.022	2.06 ± 0.22	1.64

Fitting parameters from the solid line models plotted in Figures 25 and 27, corresponding to Equation 3.2.

mean count rate of 0.014 cps (0.3-10 keV), is well-fitted ($\chi^2/\nu = 68.57/75$) by an absorbed power-law with photon index $\Gamma = 2.07 \pm 0.06$ and an absorbing column of $N_H = 4.4 \pm 0.1 \times 10^{21}$ cm^{-2} at $z = 1.406$ in addition to the Galactic absorbing column. The mean unabsorbed flux is (103 ± 5) nJ at 1 keV.

Assuming the standard external shock model (e.g., Sari, Piran, and Narayan 1998) for a constant density circum-burst medium (CBM), in the slow-cooling regime with a cooling break below the X-ray band, the X-ray temporal and spectral indices imply and are consistent with a power-law index for the shocked electrons of $p = 2.26 \pm 0.03$. Assuming the optical/NIR bands are below the cooling break, the implied temporal decay is $t^{-0.94 \pm 0.02}$. This is similar to the typical decay laws we observe (Figure 25; Table 2), although the observed indices are not constant across the optical/NIR bands. The early-time optical/NIR spectral energy distribution (SED) is consistent with the expected $F_\nu \propto \nu^{-0.6}$ ($F_\lambda \propto \lambda^{0.24}$ in Figure 26) spectrum, absorbed by $A_V \sim 0.1$ of SMC-type dust (Pei 1992). The 1 keV to r-band flux ratio (~ 50; Figure 25) is consistent with a cooling break initially near the X-ray band.

The temporal decay law in the optical/NIR bands flattens slightly with increasing

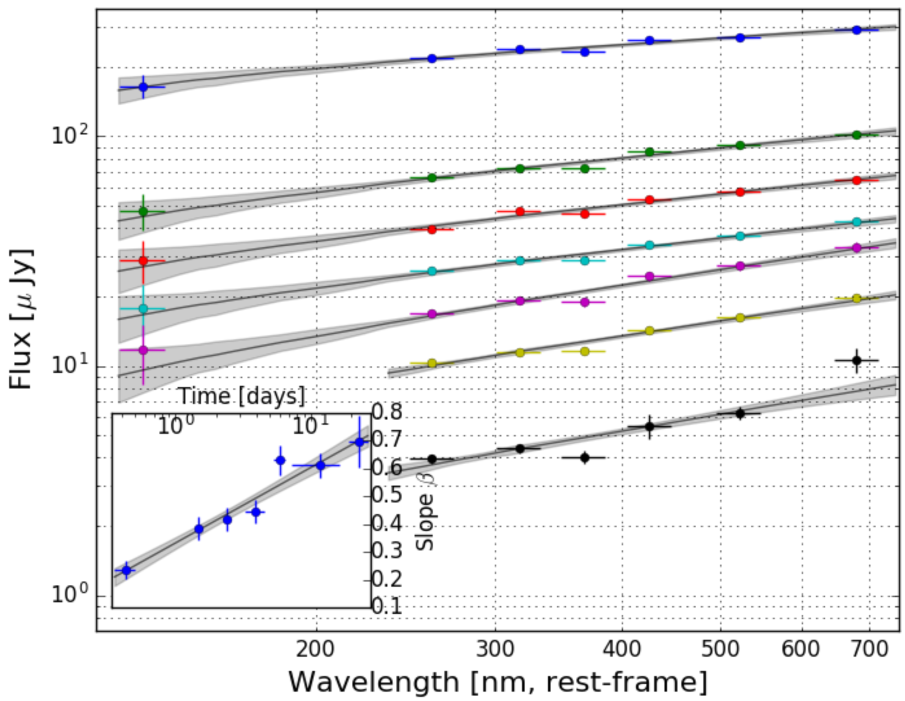

Figure 26. GRB 160625B RATIR SED

The spectral evolution of GRB 160625B over the RATIR bands, as well as UV from *Swift*. The data are fit with a power law attenuated by SMC extinction (Pei 1992). The inset shows the evolution of the spectral power-law index, β, over time; the power-law index and fit statistics can be found in Table 3. The data presented in this figure can be found in the Appendix.

wavelength (Figure 25, inset; Table 2). The data are well-fitted as $\alpha(\lambda) = (0.938 \pm 0.003) - 2.5(0.08 \pm 0.01)\log(\lambda/\ [980\ \mathrm{nm}])$. The result is a slow and continuous reddening that yields an optical/NIR SED (Figure 26) described by a gradually steepening power-law index, $\beta = (0.60 \pm 0.07) + (0.26 \pm 0.06)\log\left(\frac{t}{20\mathrm{days}}\right)$, reaching $F_\lambda \propto \lambda^{0.6-0.7}$ by the end of the observation. The evolution of the spectral power law index – likely due to a gradual passage of the synchrotron spectrum beginning prior to our observations – may or may not continue through the jet-break (Figure 26, inset). The color transition

Table 3. GRB 160625B SED Fitting Parameters

Time (days)	β	χ^2/ν
0.36-0.51	0.24 ± 0.07	0.96
1.41-1.52	0.39 ± 0.07	1.40
2.27-2.52	0.42 ± 0.07	1.61
3.30-4.53	0.45 ± 0.07	1.36
5.31-6.45	0.63 ± 0.08	2.50
7.30-16.41	0.61 ± 0.07	3.42
19.25-26.51	0.70 ± 0.11	5.84

Fits for the power-law models describing the spectral evolution of GRB 160625B plotted in Figure 26; all models are fit using an $A_V = 0.05 \pm 0.04$ in SMC law extinction (Pei 1992) in the host galaxy.

prior to 10 days is gradual and smooth, with no break in either the spectrum or lightcurve. We see no evidence for any strong spectral evolution during the jet break, with the synchrotron cooling frequency likely to be above the RATIR bandpass until at least approximately 30 days after the GRB.

We determine the jet opening angle, $\theta_{\text{jet}} = \Gamma(t_{\text{jet}})^{-1}$, using the jet break time t_{jet} as

$$\begin{aligned}\theta_{\text{jet}} = \Gamma^{-1}(t_{\text{jet}}) &= 3.27\left(\frac{t_{\text{jet}}}{\text{days}}\right)^{3/8}\left(\frac{1+z}{2}\right)^{-3/8}\left(\frac{E_{\text{iso}}}{10^{53}\text{ erg}}\right)^{-1/8}\left(\frac{\eta}{0.2}\right)^{1/8}\left(\frac{n}{0.1\text{ cm}^{-3}}\right)^{1/8}\\ &= 2.28\left(\frac{t_{\text{jet}}}{12.6\text{ days}}\right)^{3/8}\text{ degrees}\end{aligned} \tag{3.1}$$

(Frail et al. 2001). Here, we have inserted values for the redshift z, the isotropic energy in γ-rays E_{iso}, the efficiency of converting the ejecta kinetic energy into γ-rays η, and the CBM density n from (Troja et al. 2017). If we make the simplifying assumption that we are viewing the jet exactly on-axis, we can use Equation 3.1 to convert between observed time and the observable extent of the jet $1/\Gamma(t)$. The light curve can then be divided by the empirical, wavelength-dependent, early-time decay law to reconstruct the apparent jet profile $F_j(\theta = 1/\Gamma)$ (Figure 27).

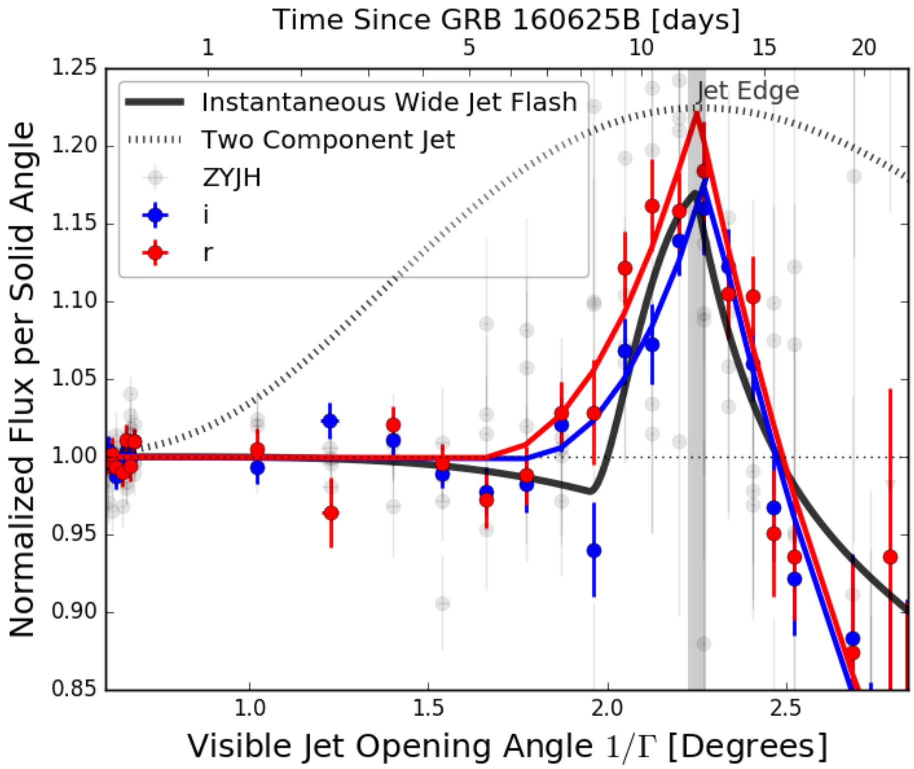

Figure 27. GRB 160625B Jet Profile

The emissivity of GRB 160625B's jet with respect to jet angle for all bands (with i and r bands highlighted), showing a structured jet with bright edges. The blue and red curves are the model shown in Equation 3.2; the black and gray curves show physical models derived in Section 3.4 for two-component jets.

We discuss the relation between $F_j(\theta)$ and the jet emissivity $j(\theta)$ in detail below in Section 3.4. In the uniform, or homogeneous, jet model (e.g. Rhoads 1997; Sari, Piran, and Halpern 1999), $F_j = 1$ until the edge of the jet becomes visible at $1/\Gamma = \theta_{\text{jet}}$. After this time, in the absence of jet spreading, $F_j(\theta) = (\theta_{\text{jet}}\Gamma)^2$, and the flux steepens by a factor $(t/t_{\text{jet}})^{-3/4}$ in time. This model fits the data well at early and late time in all bands (see, Figure 25). However, the lightcurve bump that occurs near the jet break requires an additional component. We assume a phenomenological model:

$$F_j(\theta = 1/\Gamma) = \begin{cases} 1, & \theta \leq \theta_1 \\ 1 + B(\theta - \theta_1)^2/(\theta_{\,\mathrm{jet}} - \theta_1)^2, & \theta_1 < \theta \leq \theta_{\,\mathrm{jet}} \\ 1 + B(\theta_{\,\mathrm{jet}}/\theta)^2, & \theta > \theta_{\mathrm{jet}} \end{cases} . \tag{3.2}$$

The apparent jet flux $F_j(\theta)$ is constant until $1/\Gamma = \theta_1$, after which point it increases quadratically by a limb-brightening factor B at the edge of the jet, $\theta_{\,\mathrm{jet}}$. We find that all bands are well-fitted by such a model with consistent values for the parameters (Table 2). The X-ray data do not require a bump, but they also cannot rule out the optical/NIR bump at $> 1\sigma$ significance ($\Delta\chi^2 = 2.28$ for 2 additional degrees of freedom). The model is also over-plotted in Figure 25 using the mean fit parameters ($\theta_1 = 1.80 \pm 0.05°$, $\theta_{\mathrm{jet}} = 2.40 \pm 0.03°$, $B = 20.5 \pm 1.2\%$) to compute $t^{-\alpha(\lambda)}F_j(\theta)$.

3.4 Discussion

Bumps of varying shapes and sizes have been observed in GRB afterglows. A contemporaneous supernova (SN) can cause a re-brightening in the afterglow lightcurves (Bloom et al. 1999; Hjorth and Bloom 2012). However, at $z = 1.406$ (Xu et al. 2016; D'Elia, Melandri, and Malesani 2016), typical SNe (absolute magnitude $M = -19$) would be 5 magnitudes fainter than the bump in Figure 25. The bump has a red color consistent with that of the afterglow, quite unlike the very blue color of the brightest SNe (e.g., Dong et al. 2016). Furthermore, SNe have very broad temporal brightening features (e.g., Bloom et al. 1999) , very different from the sharp bump in the afterglow of GRB 160625B. Reprocessing the afterglow light by dust in the CBM can, in principle, generate bumps in the NIR but not typically in the r band (e.g., Waxman and Draine 2000; Esin and Blandford 2000). As the optical transition from reverse-shock to forward-shock dominated emission is early ($t < 1$ day; Troja et al. 2017), it is not likely to contribute the sharp bump 10 days after GRB 160625b.

X-ray flaring is a common effect seen in many early afterglows (e.g., Galama et al. 1998). Attributed to a central engine that is still active (Li et al. 2012; Galama et al. 1998), these features are similarly narrow in time – $dt/t \sim 0.1$ for early (e.g., Chincarini et al. 2007) and late (e.g., Curran et al. 2008) flares – but refreshed shocks typically occur within hours of the GRB (Panaitescu, Mészáros, and Rees 1998; Li et al. 2012) and also exhibit harder spectra than the afterglow (e.g., Butler and Kocevski 2007). It is important to note that there is no observed change to the color evolution in the SED around the time of the re-brightening.

It seems most natural to assume that the increase in flux just before the jet break is not coincidental, but that the phenomena are related. However, it is important to note that the effects of relativistic beaming would permit a jet with bright edges (e.g., as implied in Equation 3.2 above, or Kumar and Granot 2003) to be observed at quite early time, yielding smooth temporal variations in the observed flux with $dt/t \sim 1$. A jet with a bright edge that does not change with time would produce a wide bump in the light curve starting at earlier times than the bump in Figure 27. To see this, we can derive the observed jet structure starting with a model for the rest-frame emissivity j' of the jet; a complete derivation of the following equations can be found in Appendix B. The expected flux is

$$f_\nu(t) = 2\pi D\Gamma^{-2} \int \varphi^2 d\varphi \int \frac{j'_\nu(t', \Omega')d\mu}{(1-\beta\mu)^2(1-\mu^2)^{3/2}} \tag{3.3}$$

(see, Woods and Loeb 1999), where D is the distance from the source to the observer and φ is the angle to the jet edge as viewed by the observer. Here, $\beta = v/c$ and $\Gamma = 1/\sqrt{1-\beta^2}$; μ is the cosine of the angle between the velocity and the direction of the observer. We now assume a spherical blast wave traveling directly toward the observer and a infinitesimally thin emitting shell with zero emissivity beyond an angle $\theta = \theta_{\rm jet}$:

$$j' = A_0 t'^{-a} \nu'^{-b} \delta(r - \beta ct) H(\theta_{\rm jet} - \theta). \tag{3.4}$$

Here, a is the power-law temporal index and b is the power-law spectral index. The rest-frame time, t', and the lab-frame time, t, are related by $t' = t + r\mu/c$, and r is the radius of the blast wave. The function H is the Heaviside function. Following (Woods and Loeb 1999), we can use the delta function to integrate over the viewing angle φ to obtain:

$$f_\nu(t) = 2\pi\beta A_0 \left(\frac{c}{D}\right)^2 \frac{t^{2-a}\nu^{-b}}{\Gamma^{2+b}} \frac{(1-\beta)^{4-a+b}}{(4-a+b)} \left(1 - \left[\frac{(1-\beta)}{(1-\beta\mu_{min})}\right]^{4-a+b}\right), \tag{3.5}$$

with $\mu_{min} = \cos(\theta_{\rm\ jet})$. The term in the square brackets goes to zero at early time, and the pre-factor is the flux due to a spherical, non-jetted blast wave, $f_{\nu,{\rm sphere}}$. Defining, $F_j = f_\nu / f_{\nu,\ {\rm sphere}}$, we have:

$$F_j = 1 - [(1-\beta)/(1-\beta\mu_{min})]^{4-a+b} \approx 1 - (1 + (\Gamma\theta_{\rm\ jet})^2)^{-n}, \tag{3.6}$$

where we have taken the small angle limit. Like F_j above in Equation 3.2, this function is constant ($F_j = 1$) at early time and then falls like $(\Gamma\theta_{\rm jet})^2 \sim t^{-3/4}$ at late time, due to the relationship, $\Gamma \propto t^{-3/8}$, seen in Equation 3.1. The index $n \approx 4$ affects the sharpness of the break, since the flux decays as $t^{-\alpha}\nu^{-b}$, $\alpha = 1/4 + a/4 + 3b/8$ and $n = 5 - 4\alpha + 5b/2$. The indices α and b above and below the cooling break are constrained by closure relations and, in terms of the electron power law index p, $n = 11/2 - p/2$ and $n = 7(1 - p/4)$ below and above the cooling break, respectively. Hence, for $p = 2$, we expect a slightly sharper break below the cooling break ($n = 4.5$) than above the cooling break ($n = 3.5$).

A narrow jet (θ_1) with a large Γ enveloped by a wider jet (θ_2) with a smaller Γ can be modeled from Equation 3.6 as $F_j(\theta_1) + (1 + B)(F_j(\theta_2) - F_j(\theta_1))$. Plotted in

Figure 27 (as Two Component Jet), this model shows that relativistic beaming does not simply restrict the observer to view a portion $1/\Gamma$ of the jet. Rather, because the emissivity versus angle is convolved with the relative Doppler factor, $1 + (\Gamma\theta)^2$, to some power, a jet with an increased edge emissivity tends to produce temporally broad light curve variations ($dt/t \approx 1$). Some mechanism must be invoked to introduce additional time dependence. A natural mechanism is the lateral spreading of the jet, which can begin around the jet break time because the entire surface of the jet is just coming into causal contact at that point. Granot 2007 argue that the the jet angle should increase as $\theta_{jet} \approx \theta_1 + c_s/(c\Gamma)$, where c_s is the sound speed, leading to an approximately constant relative Doppler factor during the expansion. The function F then remains flat for longer. More recent work on jet expansion points towards a slower logarithmic jet expansion (Eerten and MacFadyen 2012; Zhang and MacFadyen 2009) as opposed to a fast exponential expansion (Sari, Piran, and Halpern 1999; Granot et al. 2001; Mao and Wang 2001).

To produce a narrow bump, we invoke the possibility of an instantaneous flash of emission, modeled by replacing H in Equation 3.4 by $H + j_e'(\theta)\delta(t' - t_1')t_1'$. Here, $j_e'(\theta)$ is a dimensionless, relative emissivity which is zero within θ_1. For $\theta > \theta_1$, we define $j_e'(\theta) = B(\theta - \theta_1)^2/(\theta_{\text{jet}} - \theta_1)^2$ (cf. Equation 3.2). With this addition, F_j (Equation 3.6) becomes:

$$F_j = 1 - [1 + (\Gamma\theta_{\text{jet}})^2]^{-n} + n\left(\frac{t}{t_1}\right)^{-n} j_e\left(\theta = \frac{1}{\Gamma}\sqrt{\frac{t - t_1}{t_1}}\right), \tag{3.7}$$

where t_1 is the observer-frame time corresponding to θ_1. This model is plotted in Figure 27, with $B = 26.4\%$.

Jets with either homogeneous or a brighter central region (Granot and Kumar 2003), viewed on-axis, are not expected to have an increase in their afterglow light curves. Jets with a brighter central region viewed slightly off-axis, may be able to cause a brief re-brightening before the jet break. If viewed from an angle not directly along the central axis of the jet, but still inside the jet opening angle ($0 < \theta_{\rm view} < \theta_{\rm\ jet}$), the observer could detect an increase in flux as the brighter center of the jet came into view. However, with these viewing conditions, we expect to see more complicated jet-break behavior on long time-scales ($dt/t \sim 1$; see, e.g., Kumar and Granot 2003). Jet models are considered in (Kumar and Granot 2003) which have a Gaussian energy profile and more exotic jet structures – such as ring- or fan-shaped jets (Granot 2007) – exhibit more complex afterglow behavior (e.g. multiple jet breaks). Two-component jets (Peng, Königl, and Granot 2005; Racusin et al. 2008) create smoother bumps at earlier times (e.g. the two-component jet plotted in Figure 27), that are not consistent with our short-duration bump and the ensuing rapid steepening by $(\Gamma\theta_{\rm\ jet})^2 \sim t^{-3/4}$.

It is also important to note that the functional form of this steepening is inconsistent with the hypothesis of continued lateral expansion of the jet. That expansion tends to halt the radial expansion of the fireball, producing a rapid flux decline in all bands proportional to t^{-p} (see, Sari, Piran, and Halpern 1999). We rule out that scenario at the $> 4\sigma$ level (Table 2), apparently consistent with hydrodynamical simulations (e.g., Kumar and Granot 2003). Although we think lateral expansion does not persist at late time for this afterglow, we do think it is important near the jet break time. It is a brief period of lateral expansion lasting $dt/t \approx df/f \approx 0.2$ that allows material just outside the primary jet ($\theta > \theta_1$ in Equation 3.2) to be shocked and to emit radiation. Interestingly, the spectral evolution we observe for this event (Section 3.3) represents a gradual loss of total blast wave energy of about 10% as compared to canonical models involving spectral/temporal breaks (e.g., Sari, Piran, and Narayan 1998). It could be that this energy reservoir, lurking near the edge of the jet, is tapped to make the bump during a brief period of lateral jet expansion.

3.5 Conclusion

With regular, nightly $riZYJH$ band observations over a period of weeks – yielding a $\lesssim 3\%$ typical photometric precision lightcurve – we are able to probe the internal jet structure of the afterglow to GRB 160625B in unprecedented detail. We observe a brief re-brightening in the afterglow light curve during the jet-break (Figure 25). We model this increase in flux by invoking a structured jet with bright edges (Figure 27), emitting instantaneously as the the jet expands laterally for a brief period. This interpretation is driven largely by the simultaneity of the bump and break. The primary alternative bump explanation surviving the arguments above – a weak pulse due to continued central engine activity – cannot be ruled-out by the X-ray data, which do not show a clear bump but are consistent with one. An admittedly more-pronounced X-ray bump does coincide with a probable jet break in the case of the flaring GRB 050502B (e.g., Falcone et al. 2006). Moreover, there is at least one case (e.g., Berger et al. 2000) of a similar multi-band optical bump present just before and not precisely simultaneous with a well-studied jet break.

We also observe a wavelength-dependent temporal evolution in the afterglow to GRB 160625B prior to the jet break, with temporal index $\alpha = 0.938 - 0.2\log(\lambda/[980\ \mathrm{nm}])$. Following the break, the temporal decay indices are consistent with those expected for a sharp-edged jet (increase by 3/4), with no lateral expansion.

GRB 160625B exhibits a very sharply defined jet break corresponding to a very narrow jet opening angle, $\theta_{\,\mathrm{jet}} \approx 2°$, indicative of nearly-on-axis viewing of a highly relativistic outflow impinging on a low density external medium (see, also, Troja et al. 2017). Typical jets should be observed at an angle $\theta_{\,\mathrm{view}} = \frac{2}{3}\theta_{\mathrm{jet}}$ and may or may not exhibit pronounced lateral expansion. Both effects can introduce variations with $dt \approx t$ (e.g., Granot 2007) and can tend to make jet break signatures in light curves less distinct. Whatever mechanism created the bump for GRB 160625B (Figure 25) also contributed to making a more distinct jet break, and this effect may or may not be common. Additional deep, high-cadence, late-time observations are required to uncover the light curve diversity and to yield a better understanding of why jet breaks are so challenging to detect and measure in the *Swift*-era (e.g., Panaitescu 2007).

3.6 Acknowledgements

We thank the RATIR project team and the staff of the Observatorio Astronómico Nacional on Sierra San Pedro Mártir, and acknowledge the contribution of Leonid Georgiev and Neil Gehrels to its development. RATIR is a collaboration between the University of California, the Universidad Nacional Autónoma de México, NASA Goddard Space Flight Center, and Arizona State University, benefiting from the loan of an H2RG detector and hardware and software support from Teledyne Scientific and Imaging. RATIR, the automation of the Harold L. Johnson Telescope of the Observatorio Astronómico Nacional on Sierra San Pedro Mártir, and the operation of both are funded through NASA grants NNX09AH71G, NNX09AT02G, NNX10AI27G, and NNX12AE66G, CONACyT grants INFR-2009-01-122785 and CB-2008-101958 , UNAM PAPIIT grant IN113810, and UC MEXUS-CONACyT grant CN 09-283.

Chapter 4

RATIR FOLLOW-UP OF FERMI-LAT EVENTS

4.1 Introduction

RATIR (Re-ionization And Transients InfraRed Camera) is a multi-band (r, i, Z, Y, J, H) instrument mounted on the 1.5-meter Harold Johnson telescope at the Observatorio Astronómico Nacional in San Pedro Martir, Baja California, Mexico. As a robotic instrument, it was designed to automatically follow-up triggers from the GCN within minutes (Alan M. Watson et al. 2012; Christopher R. Klein et al. 2012), and has an automated data reduction pipeline. With coverage into the near-infrared, RATIR is well suited to target gamma-ray burst (GRB) afterglows, especially those at high redshifts (Littlejohns et al. 2014).

RATIR relies on triggers from other telescopes, especially space-based telescopes, to detect and localize GRBs for further study. These triggers are posted to The Gamma-ray Coordinates Network (GCN), a network of space and ground-based telescopes that look for and study GRBs. Launched in 2004, the Neil Gehrels *Swift* Observatory, carries the Burst Alert Telescope (BAT, Barthelmy et al. 2005) to locate GRBs, and the X-ray Telescope (XRT, D. N. Burrows et al. 2005) and Ultraviolet/Optical Telescope (UVOT, Roming et al. 2005) to study the GRBs and their afterglows. The *Fermi Space Telescope* was launched in 2008 carrying the Gamma-ray Burst Monitor (GBM, Meegan et al. 2009) and Large Area Telescope (LAT, Atwood et al. 2009) instruments to detect and study GRBs over a wide range of γ-ray energies. Together these space-based telescopes are responsible for most of the GRB detections posted to the GCN.

aLIGO's first detection (Abbott et al. 2016) of gravitational waves (GWs) and subsequent GRB-GW dual detection (Abbott and al. 2017) ushered in a new era of multi-messenger astronomy. With GW detectors posting notices to the GCN, a strategy was developed to have RATIR follow-up on GW triggers, laid out in Golkhou et al. 2018. RATIR's narrow field of view (5.3'x5.3' for r and i bands, and 5'x10' for $ZYJH$ bands) makes following up GW triggers from aLIGO and VIRGO, with 100 square degree error regions, very challenging. To overcome this, a list of galaxies in the aLIGO/VIRGO search region is generated; RATIR looks through a ranked list of these galaxies, looking for new sources using image subtractions over multiple epochs. Potential host galaxy measurements for an electromagnetic counterpart to the GW from aLIGO/VIRGO Trigger G268556 are shown in Appendix D, Table 6; no new sources were detected in these galaxies over the course of several nights of observation.

There are other ground based telescopes that regularly follow-up on GRB triggers from the GCN. The Gamma-Ray Burst Optical and Near-infrared Detector (GROND, Greiner et al. 2008) is a similar device to RATIR. GROND is a 7-channel ($griZJHK$) instrument mounted on the 2.2-meter MPI/ESO telescope in La Silla, Chile. RATIR and GROND operate in similar manners, and each have their advantages and disadvantages. GROND has a wider wavelength coverage, including g on the shorter end and K on the longer end. GROND operates on a larger telescope, and is therefore able to resolve fainter sources; however, GROND is not the only instrument used on the MPI/ESO telescope. RATIR has a narrower bandpass, but includes a Y filter, which can help in the determination of certain GRB redshifts. RATIR is the only instrument mounted on the 1.5-meter Harold Johnson telescope. RATIR is located in the northern hemisphere, whereas GROND is located in the southern hemisphere. This means that each telescope has access to unique parts of the sky, but also share some overlap where both instruments can make detections.

4.2 RATIR Performance

Since it began operation in December 2012, there have been 195 unique RATIR generated postings to the GCN for GRBs; RATIR will continue its work with funding through at least 2020. Of the 195 GRBs followed-up by RATIR, 99 have been detections, while 96 have been upper limits. For a list of detections and upper limits, including magnitudes, exposure lengths, and observation times, see Appendix C, Table 5. Over its lifetime, RATIR has either detected and/or provided upper limits for on average ≈ 2.71 GRBs every month (1.38 ± 0.14 detections per month and 1.33 ± 0.14 upper limits per month).

In Figure 28, the frequency of RATIR GRB follow-ups is plotted with two-month long bins; in this figure we can see that RATIR has been functioning almost continuously, with gaps appearing during August and September of 2014 (maintenance and monsoon season) and December 2015 through January 2016 (maintenance and holidays).

While RATIR has been able to take data for much of its existence, there have been large passages of time where n-IR data has not been available, due to problems with the cryogenic cooling systems. As seen in Table 5, Y, J, and H coverage was unavailable from October 2014 until February 2016, and Z, Y, J, and H coverage was missing from February 2018 to August 2018. The reason for the long down times for

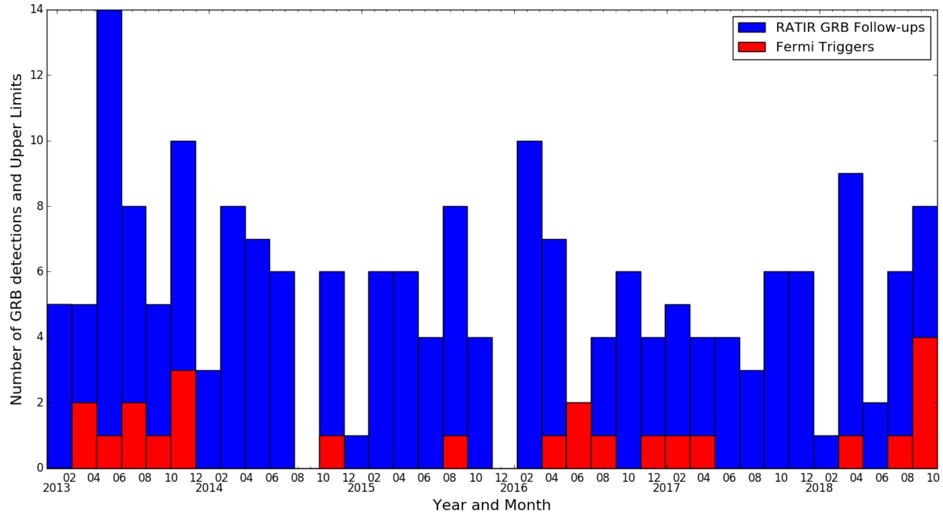

Figure 28. Histogram of RATIR Observation Dates

The bi-monthly frequency of detections and upper limits for GRBs obtained by RATIR during its operation. Data was taken from RATIR generated postings to the GCN.

the n-IR detectors is that they must be shipped back to the US for maintenance, due to ITAR restrictions.

The RATIR response time to investigating GRBs is plotted in Figure 29. We note that RATIR most often follows up GRBs within the first hour, and most initial observations occur within the first day of the GRB.

The median response time for RATIR is about 10 hours after the GRB is first detected. Once RATIR has begun observation, the median observation time is 2.31 hours. During its observation time, RATIR has a median efficiency ($\frac{\text{exposure time}}{\text{observation time}}$) of 0.66 for r and i bands, and 0.24 for Z, Y, J, and H bands; the reason for the n-IR bands having less than half the efficiency of the visible bands, is that when taking n-IR data, RATIR must switch between two paired filters, ZJ and YH.

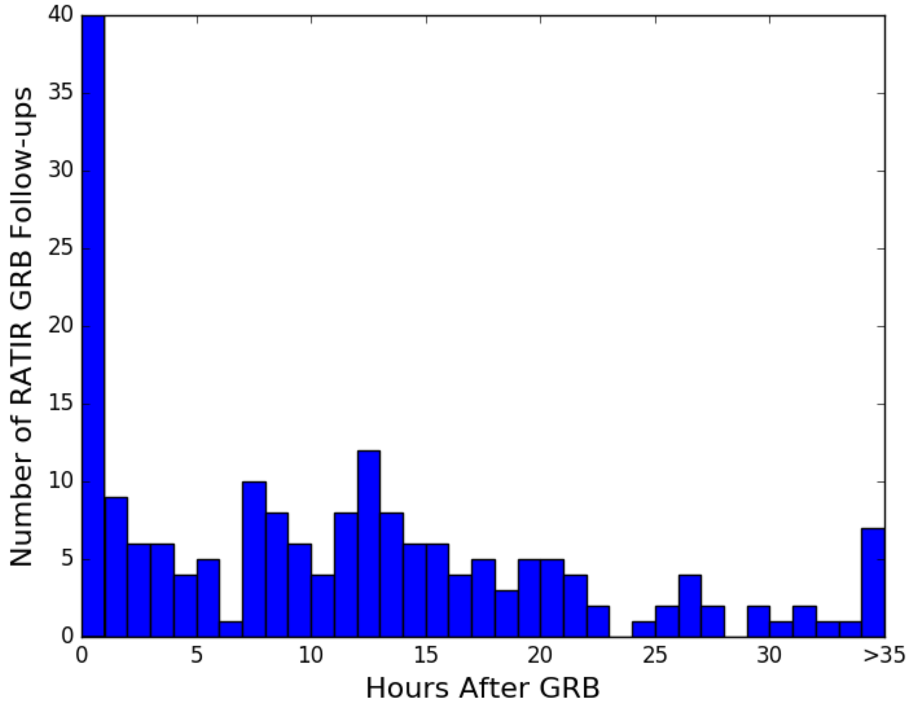

Figure 29. Histogram of RATIR Response Time

The response time of RATIR for following-up GRBs. Follow-ups occur most often within the first hour after the GRB; there is a also a smaller secondary peak 12 hours after the GRB, most likely due to the day-night cycle.

4.3 Conclusion

My work on this RATIR project is ongoing. I will be looking at the 24 Fermi GRBs that RATIR has followed up, before proceeding to RATIR follow-up of other triggers. A comprehensive look at RATIR follow-up of *Swift* events was published in Littlejohns et al. 2015. In that paper 28 GRBs, where RATIR detections were made after a *Swift* trigger, were analyzed; 40 additional *Swift* triggers were followed up by RATIR, where only upper limits were obtained, at the time of that paper. There have been 101 *Swift* GRBs that RATIR has followed-up since that publication. The third observation run of aLIGO is ongoing, and RATIR is continuing its program to try to detect an electromagnetic counterpart to a gravitational wave.

We will look to compare the work done by RATIR and GROND to follow-up GRBs. Finally, we will discuss some of the important results that RATIR has contributed to and their implications.

Chapter 5

CONCLUSIONS AND FUTURE PROJECTS

5.1 Conclusions

In this thesis, I have laid out the benefits of studying various transient astronomical sources in the IR, detailed my work with detectors and instrumentation to take advantage of those benefits, and demonstrated how IR data from transient sources can probe new frontiers.

The near-infrared and short-wavelength infrared offer a unique window (750-2500 nm) to study transient phenomena in the IR. IR light scatters off dust particles at a much lower rate than shorter wavelength light (e.g., Glass 1999); as such, targeting GRB afterglows in the IR can reduce the number of dark GRBs (e.g., Greiner, J. et al. 2011). GRB afterglows have their peak brightness in the IR, and last longer in this bandpass (e.g., van Eerten 2013; Rau et al. 2004); studying GRB afterglow in both visible and IR wavelengths can lead to the identification of high redshift events (e.g., Littlejohns et al. 2014). Kilonovae also have their peak brightness in the IR (e.g., Tanvir et al. 2013; Berger, Fong, and Chornock 2013). GRBs and kilonovae represent the most likely electromagnetic counterpart to gravitational waves that can currently be detected.

Studying other transient sources in the IR offers advantages as well. Type Ia supernova light curves are more standard in the IR (Friedman et al. 2015; Mandel, Narayan, and Kirshner 2011). Exoplanet transit light curves are easier to identify in the IR due to the effects of limb darkening (Neilson and Lester 2011b; Howarth

2011a). The study of exoplanets around smaller, cooler stars (M-type and Brown Dwarfs) is also optimal while operating in the IR (e.g., Osterman et al. 2012).

With these advantages of working in the IR in mind, I tested novel instrumentation that looks to mitigate some of the drawbacks of the current standard for IR astronomy; HgCdTe detectors must be cryogenically cooled to drive down the dark noise, leading to instruments that are more complicated, prone to failure, and expensive. I tested an InGaAs detector, a techonology orignially developed for the night vision and surveillance industry, for use in astronomical research. Through extensive labratory and on-sky testing, I am able to show that InGaAs detectors can in fact make useful contributions to the study of transient phenomena in the IR; some highlights of this work include detecting several exoplanet transits, as well as a nearby supernova, with an InGaAs detector mounted on small ($\lesssim$ 0.5-meter) telescopes from a rooftop at ASU.

Using the established RATIR instrument, I was able to study GRB afterglows in the IR with unprecedented precision, allowing me to probe the structure of a GRB jet. GRB 160625B had a particularly interesting afterglow, with a brief re-brightening before the jet-break, indicative of a jet-edge that is brighter than the center. My work with RATIR is ongoing to try to find more interesting GRBs, that can help shed light on the unanswered questions surrounding these events.

5.2 Future Projects

The benefits of IR transient study provide excellent motivation to overcoming the obstacles inherent in ground-based IR astronomy. Using InGaAs detectors, like those described in Chapter 2, a system like DDOTI (see section 5.2.2) can be assembled at a reasonable price ($\sim \$500,000$), allowing IR capabilities for a GW follow-up survey. A cheaper alternative would be to upgrade existing survey telescopes with high efficiency dichroic mirrors to split visible and IR light with minimal losses compared to conventional beam splitters.

Another way to study transient phenomena in the IR at relatively low costs would be to make use of the CubeSat standard (Puig-Suari, Turner, and Ahlgren 2001); IR detectors in orbit are not constrained by the brightness of the atmosphere. Using InGaAs is an attractive option compared to other IR detectors that require cryogenic cooling, leading to smaller, more cost-effective payloads. The compact design and small mass, meager power consumption, and relatively low cost of the InGaAs camera tested in Strausbaugh, Jackson, and Butler 2018 makes them viable candidates for CubeSat missions on the order of a couple of years. With promising performance on a CubeSat mission, larger InGaAs arrays could lead to science grade detectors capable of warranting their own large space based telescope.

The third observation run of aLIGO (O3) will hopefully detect more events with possible EM counterparts, and I hope to be a part of the detection of an EM counterpart using a transient survey telescope. These surveys offer other avenues for transient studies that are not dependent on aLIGO. I hope to be involved in developing a catalog for future transient detection using image subtraction and detecting transient events that can be followed up by more sensitive instruments.

5.2.1 Continuing Work with RATIR

My work with RATIR will continue, as there are ongoing projects that I am involved with. Following the plan laid out in Golkhou et al. 2018, we will follow-up gravitational wave triggers from aLigo O3. I will finish my work looking back at previous years of RATIR data, determining its efficiency in following up Fermi triggers, and will look into incorporating data collected with GROND, a RATIR analogue in the southern hemisphere; I plan to publish these results in The Astronomical Journal.

5.2.2 Deca-Degree Optical Transient Imager (DDOTI)

The Deca-Degree Optical Transient Imager (DDOTI), shown in Figure 30, is currently being constructed at the Observatorio Astronómico Nacional in Sierra San Pedro Martír, Baja California, México, on the same mountain as RATIR. DDOTI consists of six 26-cm, co-mounted telescopes. The telescopes will operate in broadband visible wavelengths with 6k by 6k CCDs; the combined sky coverage for all six telescopes is 72 square degrees.

The large error regions ($\sim$ 100 square degrees) for aLIGO, Virgo, and Fermi's GBM drive the design decisions for DDOTI. With a 72 square degree field of view, DDOTI will be able to search the entire error region within a few minutes down to $r \approx 18$ at 10σ. With these specifications, DDOTI should be able to identify bright electromagnetic counterparts to GW signals detected by aLIGO, as well as double the rate at which GBM-detected GRBs are localized.

The current strategy for source identification using DDOTI is to compare data collected with DDOTI to existing surveys, such as the US Naval Observatory catalog (USNO, Monet et al. 1998), which we regard as complete at $r \approx 18$. Any sources detected by DDOTI that are not present in the USNO catalog are flagged as possible potential transient phenomena and can be followed up by more sensitive instruments, like RATIR.

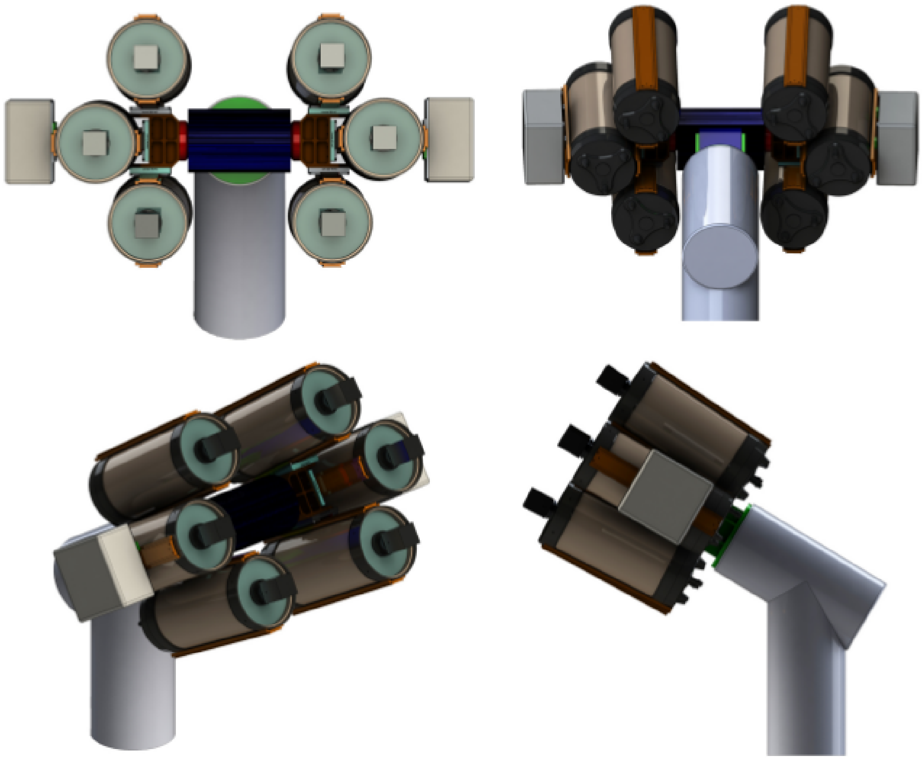

Figure 30. Rendering of DDOTI Telescope

A rendering of the six, co-mounted, 28-cm telescopes that make up the Deca-Degree Optical Transient Imager (DDOTI). Adopted from Watson et al. 2016.

Future work with DDOTI will be to develop an efficient image subtraction algorithm to provide real-time transient identifications. Once a database of light curves has been developed, more sophisticated machine learning software can be deployed on DDOTI data to find transients not detected by image subtraction.

Funding has already been approved for a DDOTI companion in France, with the goal of developing a network that can provide continuous night sky coverage. Due to relatively low cost of DDOTI ($\sim$ \$500k, Watson et al. 2016), another DDOTI companion instrument could be constructed in the southern hemisphere which would allow for entire sky coverage (not limited to only the northern hemisphere).

5.2.3 Post-Doctoral Position at the University of the Virgin Islands

I have accepted a post-doctoral position at the University of the Virgin Islands, working with Professor Antonino Cucchiara. I will be able to continue my work with RATIR and DDOTI, as Professor Cucchiara is part of those collaborations. I will also be working on the Deeper Wider Faster program (DWF, Andreoni and Cooke 2018), as well as a BurstCube (Racusin et al. 2016) satellite prototype.

5.2.3.1 Deeper Wider Faster Program (DWF)

The DWF program (Andreoni and Cooke 2018) is a transient survey whose goal is to identify transient phenomena on milli-second to hour timescales. Working towards this goal is a network of instruments around the globe observing from radio wavelengths through gamma-rays. The science cases that will benefit from rapid transient identification and study are as follows: supernova shock breakouts and early time supernova beavior that can differentiate between different supernova explosion mechanisms such as standing accretion shocks (Blondin, Mezzacappa, and DeMarino 2003), magneto-rotational instabilities (Akiyama et al. 2003), acoustic shocks (A. Burrows et al. 2007), and QCD phase-transitions (Sagert et al. 2009); GRBs; kilonovae; orphan afterglows; electromagnetic counterparts to GWs; and fast radio bursts (FRBs Lorimer et al. 2007), whose progenitors are unknown.

Infrastructure for the DWF program is already in place, with the *Mary* pipeline (Andreoni et al. 2017) for rapid transient identification, visualization software for human identification and verification of transients (Meade et al. 2017), and a novel approach to compressing data (Vohl et al. 2017) for transfer to remote supercomputers for source identification.

My work with the project will be to further develop the software for transient identification, specifically with machine learning algorithms. I will also use my knowledge of GRBs to aid in the detection of any afterglows or other electromagnetic counterparts to GWs detected by the DWF program.

5.2.3.2 BurstCube

The BurstCube satellite will be a 6u CubeSat monitoring the sky for γ-rays, and localizing the sources from events such as GRBs, and other flaring transient phenomena (Racusin et al. 2016); a prototype of this satellite is being built at the University of the Virgin Islands. BurstCube will use scintillation crystals and silicon photo-multipliers (SiPM) to detect incoming γ-rays; this type of design has been used on the *Fermi* (Meegan et al. 2009) and *BeppoSAX* (Frontera, F. et al. 1997) satellites. Cesium Iodide crystals will emit visible wavelength light when exposed to photons with γ-ray energy (e.g., Nishimura et al. 1995); the visible light emitted can then be detected using SiPM. The eventual goal will be to have multiple BurstCubes in orbit to provide full-sky coverage, at a fraction of the cost of a flagship NASA mission.

I will contribute in the planning, design, and construction of the BustCube prototype by leveraging my previous experience with SiPM (Bouvier et al. 2013) and my knowledge of GRBs and other transients. I hope that my experiences and involvement with the BurstCube will help in my goal to propose and fund a CubeSat operating in the IR with InGaAs detectors.

REFERENCES

Abbott, B. P., R. Abbott, T. D. Abbott, M. R. Abernathy, F. Acernese, K. Ackley, C. Adams, et al. 2016. "Observation of Gravitational Waves from a Binary Black Hole Merger." *Physical Review Letters* 116, no. 6, 061102 (February): 061102. doi:10.1103/PhysRevLett.116.061102. arXiv: 1602.03837 [gr-qc].

Abbott, B. P., R. Abbott, T. D. Abbott, F. Acernese, K. Ackley, C. Adams, T. Adams, P. Addesso, R. X. Adhikari, et al. 2017. "A gravitational-wave standard siren measurement of the Hubble constant." *Nature* 551 (November): 85–88. doi:10.1038/nature24471. arXiv: 1710.05835.

Abbott, B. P., R. Abbott, T. D. Abbott, F. Acernese, K. Ackley, C. Adams, T. Adams, P. Addesso, R. X. Adhikaril, and et. al. 2017. "Gravitational Waves and Gamma-Rays from a Binary Neutron Star Merger: GW170817 and GRB 170817A." *The Astrophysical Journal* 848, no. 2 (October): L13. doi:10.3847/2041-8213/aa920c.

Abbott, B. P., and et. al. 2017. "Multi-messenger Observations of a Binary Neutron Star Merger." *The Astrophysical Journal* 848, L12 (October): L12. doi:10.3847/2041-8213/aa91c9. arXiv: 1710.05833 [astro-ph.HE].

Akiyama, Shizuka, J. Craig Wheeler, David L. Meier, and Itamar Lichtenstadt. 2003. "The Magnetorotational Instability in Core-Collapse Supernova Explosions." *The Astrophysical Journal* 584 (February): 954–970. doi:10.1086/344135. arXiv: astro-ph/0208128 [astro-ph].

Alan M. Watson, Michael G. Richer, Joshua S. Bloom, Nathaniel R. Butler, Urania Ceseña, David Clark, Enrique Colorado, et al. 2012. "Automation of the OAN/SPM 1.5-meter Johnson telescope for operations with RATIR," vol. 8444. doi:10.1117/12.926927.

Alpher, R. A., H. Bethe, and G. Gamow. 1948. "The Origin of Chemical Elements." *Phys. Rev.* 73 (7): 803–804. doi:10.1103/PhysRev.73.803.

Amati, L., Frontera, F., Tavani, M., in 't Zand, J. J. M., Antonelli, A., Costa, E., Feroci, M., et al. 2002. "Intrinsic spectra and energetics of BeppoSAX Gamma-Ray Bursts with known redshifts." *A&A* 390 (1): 81–89. doi:10.1051/0004-6361:20020722.

Andreoni, I., C. Jacobs, S. Hegarty, T. Pritchard, J. Cooke, and S. Ryder. 2017. "Mary, a Pipeline to Aid Discovery of Optical Transients." *Publications of the Astronomical Society of Australia* 34, e037 (September): e037. doi:10.1017/pasa.2017.33. arXiv: 1708.04629 [astro-ph.IM].

Andreoni, Igor, and Jeff Cooke. 2018. "The Deeper Wider Faster program: chasing the fastest bursts in the Universe." *arXiv e-prints,* arXiv:1802.01100 (February): arXiv:1802.01100. arXiv: 1802.01100 `[astro-ph.IM]`.

Arons, AB, and MB Peppard. 1965. "Einstein's Proposal of the Photon Concept—a Translation of the Annalen der Physik Paper of 1905." *American Journal of Physics* 33 (5): 367–374.

Atwood, W. B., A. A. Abdo, M. Ackermann, W. Althouse, B. Anderson, M. Axelsson, L. Baldini, et al. 2009. "The Large Area Telescope on the Fermi Gamma-Ray Space Telescope Mission." *The Astrophysical Journal* 697 (2): 1071. http://stacks.iop.org/0004-637X/697/i=2/a=1071.

Ballantyne, D. R., J. D. Purvis, R. G. Strausbaugh, and R. C. Hickox. 2012. "IONIZED REFLECTION SPECTRA FROM ACCRETION DISKS ILLUMINATED BY X-RAY PULSARS." *The Astrophysical Journal* 747, no. 2 (February): L35. doi:10.1088/2041-8205/747/2/l35.

Barthelmy, Scott D., Louis M. Barbier, Jay R. Cummings, Ed E. Fenimore, Neil Gehrels, Derek Hullinger, Hans A. Krimm, et al. 2005. "The Burst Alert Telescope (BAT) on the SWIFT Midex Mission." *Space Science Reviews* 120, no. 3 (October): 143–164. doi:10.1007/s11214-005-5096-3.

Baskin, Nathaniel J., Heather A. Knutson, Adam Burrows, Jonathan J. Fortney, Nikole K. Lewis, Eric Agol, David Charbonneau, et al. 2013. "Secondary Eclipse Photometry of the Exoplanet WASP-5b with Warm Spitzer." *The Astrophysical Journal* 773, 124 (August): 124. doi:10.1088/0004-637X/773/2/124. arXiv: 1303.3886 `[astro-ph.EP]`.

Basu, Shantanu, and Eduard I. Vorobyov. 2012. "The migrating embryo model for disk evolution." *Meteoritics and Planetary Science* 47 (December): 1907–1914. doi:10.1111/maps.12040. arXiv: 1211.0625 `[astro-ph.SR]`.

Bean, Jacob L., Jean-Michel Désert, Petr Kabath, Brian Stalder, Sara Seager, Eliza Miller-Ricci Kempton, Zachory K. Berta, Derek Homeier, Shane Walsh, and Andreas Seifahrt. 2011. "THE OPTICAL AND NEAR-INFRARED TRANSMISSION SPECTRUM OF THE SUPER-EARTH GJ 1214b: FURTHER EVIDENCE FOR A METAL-RICH ATMOSPHERE." *The Astrophysical Journal* 743, no. 1 (November): 92. doi:10.1088/0004-637x/743/1/92.

Becker, A. 2015. *HOTPANTS: High Order Transform of PSF ANd Template Subtraction.* Astrophysics Source Code Library, April. ascl: 1504.004.

Beckers, Jacques M. 1986. "Field Of View Considerations For Telescope Arrays," vol. 0628. doi:10.1117/12.963538.

Beichman, Charles, Bjoern Benneke, Heather Knutson, Roger Smith, Pierre-Olivier Lagage, Courtney Dressing, David Latham, Jonathan Lunine, Stephan Birkmann, Pierre Ferruit, et al. 2014. "Observations of transiting exoplanets with the James Webb Space Telescope (JWST)." *Publications of the Astronomical Society of the Pacific* 126 (946): 1134.

Belczynski, Krzysztof, Rosalba Perna, Tomasz Bulik, Vassiliki Kalogera, Natalia Ivanova, and Donald Q. Lamb. 2006. "A Study of Compact Object Mergers as Short Gamma-Ray Burst Progenitors." *The Astrophysical Journal* 648, no. 2 (September): 1110–1116. doi:10.1086/505169.

Belu, AR, Franck Selsis, J-C Morales, Ignasi Ribas, Christophe Cossou, and H Rauer. 2011. "Primary and secondary eclipse spectroscopy with JWST: exploring the exoplanet parameter space." *Astronomy & Astrophysics* 525:A83.

Berger, E. 2009. "The Host Galaxies of Short-Duration Gamma-Ray Bursts: Luminosities, Metallicities, and Star-Formation Rates." *The Astrophysical Journal* 690 (January): 231–237. doi:10.1088/0004-637X/690/1/231. arXiv: 0805.0306 [astro-ph].

Berger, E., W. Fong, and R. Chornock. 2013. "An r-process Kilonova Associated with the Short-hard GRB 130603B." *The Astrophysical Journal* 774, L23 (September): L23. doi:10.1088/2041-8205/774/2/L23. arXiv: 1306.3960 [astro-ph.HE].

Berger, E., R. Sari, D. A. Frail, S. R. Kulkarni, F. Bertoldi, A. B. Peck, K. M. Menten, et al. 2000. "A Jet Model for the Afterglow Emission from GRB 000301C." *The Astrophysical Journal* 545 (1): 56. http://stacks.iop.org/0004-637X/545/i=1/a=56.

Bertin, E. 2010. *SWarp: Resampling and Co-adding FITS Images Together.* Astrophysics Source Code Library, October. ascl: 1010.068.

Bertin, E., and S. Arnouts. 1996. "SExtractor: Software for source extraction." *Astronomy and Astrophysics, Supplement* 117 (June): 393–404. doi:10.1051/aas:1996164.

Blondin, John M., Anthony Mezzacappa, and Christine DeMarino. 2003. "Stability of Standing Accretion Shocks, with an Eye toward Core-Collapse Supernovae." *The Astrophysical Journal* 584 (February): 971–980. doi:10.1086/345812. arXiv: astro-ph/0210634 [astro-ph].

Bloom, J. S., S. R. Kulkarni, S. G. Djorgovski, A. C. Eichelberger, P. Côté, J. P. Blakeslee, S. C. Odewahn, et al. 1999. "The unusual afterglow of the γ-ray burst of 26 March 1998 as evidence for a supernova connection." *Nature* 401 (September): 453–456. doi:10.1038/46744. eprint: astro-ph/9905301.

Boesgaard, Ann Merchant, and Gary Steigman. 1985. "Big Bang nucleosynthesis: theories and observations." *Annual Review of Astronomy and Astrophysics* 23 (1): 319–378.

Borne, K., J. Becla, I. Davidson, A. Szalay, and J. A. Tyson. 2008. "The LSST Data Mining Research Agenda." In *American Institute of Physics Conference Series,* edited by Coryn A. L. Bailer-Jones, 1082:347–351. American Institute of Physics Conference Series. December. doi:10.1063/1.3059074. arXiv: 0811.0167 [astro-ph].

Borucki, William J, David Koch, Gibor Basri, Natalie Batalha, Timothy Brown, Douglas Caldwell, John Caldwell, Jørgen Christensen-Dalsgaard, William D Cochran, Edna DeVore, et al. 2010. "Kepler planet-detection mission: introduction and first results." *Science* 327 (5968): 977–980.

Bouchy, F., S. Udry, M. Mayor, C. Moutou, F. Pont, N. Iribarne, R. da Silva, et al. 2005. "ELODIE metallicity-biased search for transiting Hot Jupiters. II. A very hot Jupiter transiting the bright K star HD 189733." *Astronomy & Astrophysics* 444 (December): L15–L19. doi:10.1051/0004-6361:200500201. arXiv: astro-ph/0510119 [astro-ph].

Bouvier, A., L. Gebremedhin, C. Johnson, A. Kuznetsov, D. A. Williams, N. Otte, R. Strausbaugh, et al. 2013. "Photosensor characterization for the Cherenkov Telescope Array: silicon photomultiplier versus multi-anode photomultiplier tube." In *Hard X-Ray, Gamma-Ray, and Neutron Detector Physics XV,* vol. 8852, 88520K. Society of Photo-Optical Instrumentation Engineers (SPIE) Conference Series. September. doi:10.1117/12.2023778. arXiv: 1308.1390 [astro-ph.IM].

Boyajian, T. S., A. Moor, A. Szewczyk, A. Weiksnar, A. J. Hoekstra, A. M. Smith, B. Csák, et al. 2016. "Planet Hunters IX. KIC 8462852 – where's the flux?" *Monthly Notices of the Royal Astronomical Society* 457, no. 4 (January): 3988–4004. doi:10.1093/mnras/stw218. eprint: http://oup.prod.sis.lan/mnras/article-pdf/457/4/3988/18513212/stw218.pdf.

Brown, R. Hanbury, and R.Q. Twiss. 1954. "LXXIV. A new type of interferometer for use in radio astronomy." *The London, Edinburgh, and Dublin Philosophical Magazine and Journal of Science* 45 (366): 663–682. doi:10.1080/14786440708520475. eprint: https://doi.org/10.1080/14786440708520475.

Burbidge, E. Margaret, G. R. Burbidge, William A. Fowler, and F. Hoyle. 1957. "Synthesis of the Elements in Stars." *Rev. Mod. Phys.* 29 (4): 547–650. doi:10.1103/RevModPhys.29.547.

Burke, Christopher J., and P. R. McCullough. 2014. "Transit and Radial Velocity Survey Efficiency Comparison for a Habitable Zone Earth." *The Astrophysical Journal* 792, 79 (September): 79. doi:10.1088/0004-637X/792/1/79. arXiv: 1406.6381 [astro-ph.EP].

Burrows, A., E. Livne, L. Dessart, C. D. Ott, and J. Murphy. 2007. "Features of the Acoustic Mechanism of Core-Collapse Supernova Explosions." *The Astrophysical Journal* 655 (January): 416–433. doi:10.1086/509773. arXiv: astro-ph/0610175 [astro-ph].

Burrows, David N., J. E. Hill, J. A. Nousek, J. A. Kennea, A. Wells, J. P. Osborne, A. F. Abbey, et al. 2005. "The Swift X-Ray Telescope." *Space Science Reviews* 120, no. 3 (October): 165–195. doi:10.1007/s11214-005-5097-2.

Butler, N. R., J. S. Bloom, and D. Poznanski. 2010. "The Cosmic Rate, Luminosity Function, and Intrinsic Correlations of Long Gamma-Ray Bursts." *The Astrophysical Journal* 711 (March): 495–516. doi:10.1088/0004-637X/711/1/495. arXiv: 0910.3341 [astro-ph.HE].

Butler, N., C. Klein, O. Fox, G. Lotkin, J. Bloom, J. X. Prochaska, E. Ramirez-Ruiz, et al. 2012. "First Light with RATIR: An Automated 6-band Optical/NIR Imaging Camera." In *Ground-based and Airborne Instrumentation for Astronomy IV,* 8446:844610. Proc. SPIE. September. doi:10.1117/12.926471.

Butler, Nathaniel R., and Daniel Kocevski. 2007. "X-Ray Hardness Evolution in GRB Afterglows and Flares: Late-Time GRB Activity without NH Variations." *The Astrophysical Journal* 663 (1): 407. http://stacks.iop.org/0004-637X/663/i=1/a=407.

Cacciari, Carla, and Gisella Clementini. 2003. "Globular cluster distances from RR Lyrae stars." In *Stellar Candles for the Extragalactic Distance Scale,* 105–122. Springer.

Chambers, K. C., E. A. Magnier, N. Metcalfe, H. A. Flewelling, M. E. Huber, C. Z. Waters, L. Denneau, et al. 2016. "The Pan-STARRS1 Surveys." *arXiv e-prints,* arXiv:1612.05560 (December): arXiv:1612.05560. arXiv: 1612.05560 [astro-ph.IM].

Chandrasekhar, S. 1934. "Stellar configurations with degenerate cores." *The Observatory* 57 (December): 373–377.

Charbonneau, David, Timothy M. Brown, Robert W. Noyes, and Ronald L. Gilliland. 2002. "Detection of an Extrasolar Planet Atmosphere." *The Astrophysical Journal* 568, no. 1 (March): 377–384. doi:10.1086/338770.

Chen, Hsiao-Wen, Jason X. Prochaska, and Josh S. Bloom. 2006. "GRB Afterglows as a New Probe of the ISM and IGM at High Redshift." *arXiv e-prints,* astro-ph/0602144 (February): astro–ph/0602144. arXiv: astro-ph/0602144 [astro-ph].

Chincarini, G., A. Moretti, P. Romano, A. D. Falcone, D. Morris, J. Racusin, S. Campana, et al. 2007. "The First Survey of X-Ray Flares from Gamma-Ray Bursts Observed by Swift: Temporal Properties and Morphology." *The Astrophysical Journal* 671 (December): 1903–1920. doi:10.1086/521591. arXiv: astro-ph/0702371 [astro-ph].

Choi, Changsu, Myungshin Im, Yiseul Jeon, and Mansur Ibrahimov. 2012. "A Y-Band Look of the Sky with 1-m Class Telescopes." *Journal of Korean Astronomical Society* 45 (February): 7–17. doi:10.5303/JKAS.2012.45.1.007. arXiv: 1202.5079 [astro-ph.CO].

Chornock, Ryan, Edo Berger, Derek B. Fox, Ragnhild Lunnan, Maria R. Drout, Wen-fai Fong, Tanmoy Laskar, and Katherine C. Roth. 2013. "GRB 130606A AS A PROBE OF THE INTERGALACTIC MEDIUM AND THE INTERSTELLAR MEDIUM IN A STAR-FORMING GALAXY IN THE FIRST Gyr AFTER THE BIG BANG." *The Astrophysical Journal* 774, no. 1 (August): 26. doi:10.1088/0004-637x/774/1/26.

Christopher R. Klein, Petr Kubánek, Nathaniel R. Butler, Ori D. Fox, Alexander S. Kutyrev, David A. Rapchun, Joshua S. Bloom, et al. 2012. "Software solution for autonomous observations with H2RG detectors and SIDECAR ASICs for the RATIR camera," vol. 8453. doi:10.1117/12.925817.

Clayton, Donald D. 1983. *Principles of stellar evolution and nucleosynthesis.* University of Chicago press.

Coward, D. M., E. J. Howell, T. Piran, G. Stratta, M. Branchesi, O. Bromberg, B. Gendre, R. R. Burman, and D. Guetta. 2012. "The Swift short gamma-ray burst rate density: implications for binary neutron star merger rates." *Monthly Notices of the Royal Astronomical Society* 425, no. 4 (October): 2668–2673. doi:10.1111/j.1365-2966.2012.21604.x. eprint: http://oup.prod.sis.lan/mnras/article-pdf/425/4/2668/4895856/425-4-2668.pdf.

Cox, John P. 1980. *Theory of stellar pulsation* [in eng]. Princeton, N.J.: Princeton University Press.

Curran, P. A., R. L. C. Starling, P. T. O'Brien, O. Godet, A. J. van der Horst, and R. A. M. J. Wijers. 2008. "On the nature of late X-ray flares in Swift gamma-ray bursts." *Astronomy & Astrophysics* 487 (August): 533–538. doi:10.1051/0004-6361:200809652. arXiv: 0802.3803 [astro-ph].

David, Arnett W., and Donald D. Clayton. 1970. "Explosive Nucleosynthesis in Stars." *Nature* 227 (5260): 780–784. doi:10.1038/227780a0.

Deffayet, Cédric, and Kristen Menou. 2007. "Probing Gravity with Spacetime Sirens." *The Astrophysical Journal* 668 (October): L143–L146. doi:10.1086/522931. arXiv: 0709.0003 [astro-ph].

D'Elia, V., A. Melandri, and D. Malesani. 2016. *GCN CIRCULAR 19601, GRB 160625B: TNG redshift confirmation.* https://gcn.gsfc.nasa.gov/other/160625B.gcn3.

Dirirsa, F., J. Racusin, J. McEnery, and R. Desiante. 2016. *GCN CIRCULAR 19580, GRB 160625B: Fermi-LAT detection of a bright burst,* June. https://gcn.gsfc.nasa.gov/other/160625B.gcn3.

Domagal-Goldman, Shawn D., Victoria S. Meadows, Mark W. Claire, and James F. Kasting. 2011. "Using biogenic sulfur gases as remotely detectable biosignatures on anoxic planets." PMC3133782[pmcid], *Astrobiology* 11, no. 5 (June): 419–441. doi:10.1089/ast.2010.0509.

Dong, Subo, B. J. Shappee, J. L. Prieto, S. W. Jha, K. Z. Stanek, T. W.-S. Holoien, C. S. Kochanek, et al. 2016. "ASASSN-15lh: A highly super-luminous supernova." *Science* 351 (6270): 257–260. doi:10.1126/science.aac9613. eprint: http://science.sciencemag.org/content/351/6270/257.full.pdf.

Eddington, A. S. 1920. "The Internal Constitution of the Stars." *Nature* 106 (September): 14 EP. https://doi.org/10.1038/106014a0.

Eerten, Hendrik J. van, and Andrew I. MacFadyen. 2012. "Observational Implications of Gamma-Ray Burst Afterglow Jet Simulations and Numerical Light Curve Calculations." *The Astrophysical Journal* 751 (2): 155. http://stacks.iop.org/0004-637X/751/i=2/a=155.

Einstein, A. 1905. "Über einen die Erzeugung und Verwandlung des Lichtes betreffenden heuristischen Gesichtspunkt." *Annalen der Physik* 322 (6): 132–148.

doi:10.1002/andp.19053220607. eprint: https://onlinelibrary.wiley.com/doi/pdf/10.1002/andp.19053220607.

Esin, Ann A., and Roger Blandford. 2000. "Dust Echoes from Gamma-Ray Bursts." *The Astrophysical Journal Letters* 534 (2): L151. http://stacks.iop.org/1538-4357/534/i=2/a=L151.

Falcone, A. D., D. N. Burrows, D. Lazzati, S. Campana, S. Kobayashi, B. Zhang, P. Mészáros, et al. 2006. "The Giant X-Ray Flare of GRB 050502B: Evidence for Late-Time Internal Engine Activity." *The Astrophysical Journal* 641 (2): 1010. http://stacks.iop.org/0004-637X/641/i=2/a=1010.

Fenimore, E. E., and E. Ramirez-Ruiz. 2000. "Redshifts For 220 BATSE Gamma-Ray Bursts Determined by Variability and the Cosmological Consequences." *arXiv Astrophysics e-prints* (April). eprint: astro-ph/0004176.

Feroz, F., S. T. Balan, and M. P. Hobson. 2011. "Detecting extrasolar planets from stellar radial velocities using Bayesian evidence." *Monthly Notices of the Royal Astronomical Society* 415 (August): 3462–3472. doi:10.1111/j.1365-2966.2011.18962.x. arXiv: 1012.5129 [astro-ph.EP].

Fischer, Debra A, Megan E Schwamb, Kevin Schawinski, Chris Lintott, John Brewer, Matt Giguere, Stuart Lynn, Michael Parrish, Thibault Sartori, Robert Simpson, et al. 2012. "Planet Hunters: the first two planet candidates identified by the public using the Kepler public archive data." *Monthly Notices of the Royal Astronomical Society* 419 (4): 2900–2911.

Frail, D. A., S. R. Kulkarni, R. Sari, S. G. Djorgovski, J. S. Bloom, T. J. Galama, D. E. Reichart, et al. 2001. "Beaming in Gamma-Ray Bursts: Evidence for a Standard Energy Reservoir." *The Astrophysical Journal Letters* 562 (1): L55. http://stacks.iop.org/1538-4357/562/i=1/a=L55.

Freedman, Deborah L., and Eli Waxman. 2001. "On the Energy of Gamma-Ray Bursts." *The Astrophysical Journal* 547 (2): 922. http://stacks.iop.org/0004-637X/547/i=2/a=922.

Freiburghaus, C., S. Rosswog, and F.-K. Thielemann. 1999. "[CLC][ITAL]r[/ITAL][/CLC]-Process in Neutron Star Mergers." *The Astrophysical Journal* 525, no. 2 (November): L121–L124. doi:10.1086/312343.

Friedman, Andrew S., W. M. Wood-Vasey, G. H. Marion, Peter Challis, Kaisey S. Mandel, Joshua S. Bloom, Maryam Modjaz, et al. 2015. "CfAIR2: Near-infrared Light Curves of 94 Type Ia Supernovae." *The Astrophysical Journal Supplement*

Series 220, 9 (September): 9. doi:10.1088/0067-0049/220/1/9. arXiv: 1408.0465 [astro-ph.HE].

Frontera, F., Costa, E., Dal Fiume, D., Feroci, M., Nicastro, L., Orlandini, M., Palazzi, E., and Zavattini, G. 1997. "The high energy instrument PDS on-board the BeppoSAX X-ray astronomy satellite." *Astron. Astrophys. Suppl. Ser.* 122 (2): 357–369. doi:10.1051/aas:1997140.

Fujii, Yuka, Daniel Angerhausen, Russell Deitrick, Shawn Domagal-Goldman, John Lee Grenfell, Yasunori Hori, Stephen R. Kane, et al. 2018. "Exoplanet Biosignatures: Observational Prospects." PMID: 29938537, *Astrobiology* 18 (6): 739–778. doi:10.1089/ast.2017.1733. eprint: https://doi.org/10.1089/ast.2017.1733.

Fuller, G. M., and B. S. Meyer. 1995. "Neutrino Capture and Supernova Nucleosynthesis." *The Astrophysical Journal* 453 (November): 792. doi:10.1086/176442.

Galama, T. J., P. J. Groot, J. van Paradijs, C. Kouveliotou, R. G. Strom, R. A. M. J. Wijers, N. Tanvir, et al. 1998. "Optical Follow-Up of GRB 970508." *The Astrophysical Journal Letters* 497 (1): L13. http://stacks.iop.org/1538-4357/497/i=1/a=L13.

Gallagher, JS, and S Starrfield. 1978. "Theory and observations of classical novae." *Annual review of astronomy and astrophysics* 16 (1): 171–214.

Gehrels, N., C. L. Sarazin, P. T. O'Brien, B. Zhang, L. Barbier, S. D. Barthelmy, A. Blustin, et al. 2005. "A short γ-ray burst apparently associated with an elliptical galaxy at redshift z = 0.225." *Nature* 437 (October): 851–854. doi:10.1038/nature04142. eprint: astro-ph/0505630.

Ghirlanda, G., G. Ghisellini, and C. Firmani. 2006. "Gamma-ray bursts as standard candles to constrain the cosmological parameters." *New Journal of Physics* 8 (July): 123. doi:10.1088/1367-2630/8/7/123. arXiv: astro-ph/0610248 [astro-ph].

Ghirlanda, G., G. Ghisellini, R. Salvaterra, L. Nava, D. Burlon, G. Tagliaferri, S. Campana, P. D'Avanzo, and A. Melandri. 2013. "The faster the narrower: characteristic bulk velocities and jet opening angles of gamma-ray bursts." *Monthly Notices of the Royal Astronomical Society* 428 (2): 1410–1423. doi:10.1093/mnras/sts128. eprint: /oup/backfile/content_public/journal/mnras/428/2/10.1093/mnras/sts128/2/sts128.pdf.

Ghirlanda, Giancarlo, Gabriele Ghisellini, and Davide Lazzati. 2004. "The Collimation-corrected Gamma-Ray Burst Energies Correlate with the Peak Energy of Their F

Spectrum." *The Astrophysical Journal* 616 (1): 331. http://stacks.iop.org/0004-637X/616/i=1/a=331.

Gieren, Wolfgang P., Pascal Fouque, and Matias Gomez. 1998. "Cepheid Period-Radius and Period-Luminosity Relations and the Distance to the Large Magellanic Cloud." *The Astrophysical Journal* 496, no. 1 (March): 17–30. doi:10.1086/305374.

Glass, I. S. 1999. *Handbook of Infrared Astronomy,* edited by R. Ellis, J. Huchra, S. Kahn, G. Rieke, and P. B. Stetson. October.

Golkhou, V. Zach, Nathaniel R. Butler, Robert Strausbaugh, Eleonora Troja, Alexander Kutyrev, William H. Lee, Carlos G. Román-Zúñiga, and Alan M. Watson. 2018. "RATIR Follow-up of LIGO/Virgo Gravitational Wave Events." *The Astrophysical Journal* 857, 81 (April): 81. doi:10.3847/1538-4357/aab665. arXiv: 1706.03898 [astro-ph.HE].

Gomboc, Andreja, and Drejc Kopac. 2010. "Duration and hardness ratio of Swift GRBs." *arXiv e-prints,* arXiv:1006.5550 (June): arXiv:1006.5550. arXiv: 1006.5550 [astro-ph.HE].

Granot, J. 2007. "The Structure and Dynamics of GRB Jets." In *Revista Mexicana de Astronomia y Astrofisica, vol. 27,* 27:140–165. Revista Mexicana de Astronomia y Astrofisica Conference Series. March. arXiv: astro-ph/0610379 [astro-ph].

Granot, J., M. Miller, T. Piran, W. M. Suen, and P. A. Hughes. 2001. "Light Curves from an Expanding Relativistic Jet." In *Gamma-ray Bursts in the Afterglow Era,* edited by Enrico Costa, Filippo Frontera, and Jens Hjorth, 312. January. doi:10.1007/10853853_82. arXiv: astro-ph/0103038 [astro-ph].

Granot, Jonathan, and Pawan Kumar. 2003. "Constraining the Structure of Gamma-Ray Burst Jets through the Afterglow Light Curves." *The Astrophysical Journal* 591 (2): 1086. http://stacks.iop.org/0004-637X/591/i=2/a=1086.

Granot, Jonathan, and Tsvi Piran. 2012. "On the lateral expansion of gamma-ray burst jets." *Monthly Notices of the Royal Astronomical Society* 421 (1): 570–587. doi:10.1111/j.1365-2966.2011.20335.x. eprint: /oup/backfile/content_public/journal/mnras/421/1/10.1111/j.1365-2966.2011.20335.x/2/mnras0421-0570.pdf.

Greene, Thomas P, Michael R Line, Cezar Montero, Jonathan J Fortney, Jacob Lustig-Yaeger, and Kyle Luther. 2016. "Characterizing transiting exoplanet atmospheres with JWST." *The Astrophysical Journal* 817 (1): 17.

Greiner, J., Krühler, T., Klose, S., Afonso, P., Clemens, C., Filgas, R., Hartmann, D. H., et al. 2011. “The nature of "dark" gamma-ray bursts.” *A&A* 526:A30. doi:10.1051/0004-6361/201015458.

Greiner, J, W Bornemann, Ch Clemens, M Deuter, G Hasinger, M Honsberg, H Huber, S Huber, M Krauss, T Krühler, et al. 2008. “GROND—a 7-channel imager.” *Publications of the Astronomical Society of the Pacific* 120 (866): 405.

Griffiths, D.J. 2005. *Introduction to Quantum Mechanics.* Pearson international edition. Pearson Prentice Hall. https://books.google.com/books?id=z4fwAAAAMAAJ.

Guetta, D. and Piran, T. 2006. “The BATSE-Swift luminosity and redshift distributions of short-duration GRBs.” *A&A* 453 (3): 823–828. doi:10.1051/0004-6361:20054498.

Guetta, Dafne, Tsvi Piran, and Eli Waxman. 2005. “The luminosity and angular distributions of long-duration gamma-ray bursts.” *The Astrophysical Journal* 619 (1): 412.

Gunn, J. E., and B. A. Peterson. 1965. “On the Density of Neutral Hydrogen in Intergalactic Space.” *The Astrophysical Journal* 142 (November): 1633–1641. doi:10.1086/148444.

Hashimoto, M., K. Nomoto, T. Tsujimoto, and F.-K. Thielemann. 1996. “Supernova Nucleosynthesis in Massive Stars.” *International Astronomical Union Colloquium* 145:157–164. doi:10.1017/S0252921100008022.

Hirschi, R., G. Meynet, and A. Maeder. 2005. “Stellar evolution with rotation. XIII. Predicted GRB rates at various Z.” *Astronomy & Astrophysics* 443 (November): 581–591. doi:10.1051/0004-6361:20053329. arXiv: astro-ph/0507343 [astro-ph].

Hjorth, J., and J. S. Bloom. 2012. “The Gamma-Ray Burst - Supernova Connection.” In *Chapter 9 in “Gamma-Ray Bursts”, Cambridge Astrophysics Series 51, eds. C. Kouveliotou, R. A. M. J. Wijers and S. Woosley, Cambridge University Press (Cambridge), p. 169-190,* edited by C. Kouveliotou, R. A. M. J. Wijers, and S. Woosley, 169–190. November.

Howarth, Ian D. 2011a. “On stellar limb darkening and exoplanetary transits.” *Monthly Notices of the Royal Astronomical Society* 418 (December): 1165–1175. doi:10.1111/j.1365-2966.2011.19568.x. arXiv: 1106.4659 [astro-ph.SR].

———. 2011b. “On stellar limb darkening and exoplanetary transits.” *Monthly Notices of the Royal Astronomical Society* 418 (December): 1165–1175. doi:10.1111/j.1365-2966.2011.19568.x. arXiv: 1106.4659 [astro-ph.SR].

Hoyle, F. 1946. " The Synthesis of the Elements from Hydrogen." *Monthly Notices of the Royal Astronomical Society* 106, no. 5 (October): 343–383. doi:10.1093/mnras/106.5.343. eprint: http://oup.prod.sis.lan/mnras/article-pdf/106/5/343/8073655/mnras106-0343.pdf.

———. 1954. "On Nuclear Reactions Occuring in Very Hot STARS.I. the Synthesis of Elements from Carbon to Nickel." *The Astrophysical Journal, Supplement* 1 (September): 121. doi:10.1086/190005.

Hubble, E. 1929. "A Relation between Distance and Radial Velocity among Extra-Galactic Nebulae." *Proceedings of the National Academy of Science* 15 (March): 168–173. doi:10.1073/pnas.15.3.168.

Hulse, R. A., and J. H. Taylor. 1975. "Discovery of a pulsar in a binary system." *The Astrophysical Journal Letters* 195 (January): L51–L53. doi:10.1086/181708.

Janka, H.-Th., K. Langanke, A. Marek, G. Martínez-Pinedo, and B. Müller. 2007. "Theory of core-collapse supernovae." The Hans Bethe Centennial Volume 1906-2006, *Physics Reports* 442 (1): 38–74. doi:https://doi.org/10.1016/j.physrep.2007.02.002.

Jimenez, Raul, and Tsvi Piran. 2013. "Reconciling the Gamma-Ray Burst Rate and Star Formation Histories." *The Astrophysical Journal* 773 (2): 126. http://stacks.iop.org/0004-637X/773/i=2/a=126.

Joergens, V., and A. Müller. 2007. "16-20 M_{Jup} Radial Velocity Companion Orbiting the Brown Dwarf Candidate Cha Hα 8." *The Astrophysical Journal* 666 (September): L113–L116. doi:10.1086/521825. arXiv: 0707.3744 [astro-ph].

Kaiser, Nicholas, Herve Aussel, Barry E. Burke, Hans Boesgaard, Ken Chambers, Mark Richard Chun, James N. Heasley, et al. 2002. "Pan-STARRS: a large synoptic survey telescope array," vol. 4836. doi:10.1117/12.457365.

Kasliwal, Mansi M., Shri R. Kulkarni, Iair Arcavi, Robert M. Quimby, Eran O. Ofek, Peter Nugent, Janet Jacobsen, et al. 2011. "PTF 10fqs: A LUMINOUS RED NOVA IN THE SPIRAL GALAXY MESSIER 99." *The Astrophysical Journal* 730, no. 2 (March): 134. doi:10.1088/0004-637x/730/2/134.

Klebesadel, R. W., I. B. Strong, and R. A. Olson. 1973. "Observations of Gamma-Ray Bursts of Cosmic Origin." *The Astrophysical Journal Letters* 182 (June): L85. doi:10.1086/181225.

Kocevski, Daniel, and Nathaniel Butler. 2008. "Gamma-Ray Burst Energetics in the Swift Era." *The Astrophysical Journal* 680 (1): 531. http://stacks.iop.org/0004-637X/680/i=1/a=531.

Kochanek, C. S., and T. Piran. 1993. "Gravitational Waves and gamma -Ray Bursts." *The Astrophysical Journal Letters* 417 (November): L17. doi:10.1086/187083. eprint: astro-ph/9305015.

König, B., K. Fuhrmann, R. Neuhäuser, D. Charbonneau, and R. Jayawardhana. 2002. "Direct detection of the companion of chi [1] Orionis." *Astronomy & Astrophysics* 394 (November): L43–L46. doi:10.1051/0004-6361:20021377. arXiv: astro-ph/0209404 [astro-ph].

Kouveliotou, C., C. A. Meegan, G. J. Fishman, N. P. Bhat, M. S. Briggs, T. M. Koshut, W. S. Paciesas, and G. N. Pendleton. 1993. "Identification of two classes of gamma-ray bursts." *The Astrophysical Journal Letters* 413 (August): L101–L104. doi:10.1086/186969.

Kreidberg, Laura, Jacob L. Bean, Jean-Michel Désert, Björn Benneke, Drake Deming, Kevin B. Stevenson, Sara Seager, Zachory Berta-Thompson, Andreas Seifahrt, and Derek Homeier. 2014. "Clouds in the atmosphere of the super-Earth exoplanet GJ 1214b." *Nature* 505 (January): 69 EP. https://doi.org/10.1038/nature12888.

Krühler, T., P. Schady, J. Greiner, P. Afonso, E. Bottacini, C. Clemens, R. Filgas, et al. 2011. "Photometric redshifts for gamma-ray burst afterglows from GROND and Swift/UVOT." *Astronomy & Astrophysics* 526, A153 (February): A153. doi:10.1051/0004-6361/201015327. arXiv: 1011.1205 [astro-ph.HE].

Kulkarni, S. R., E. O. Ofek, A. Rau, S. B. Cenko, A. M. Soderberg, D. B. Fox, A. Gal-Yam, et al. 2007. "An unusually brilliant transient in the galaxy M85." *Nature* 447 (May): 458 EP. https://doi.org/10.1038/nature05822.

Kumar, Pawan, and Jonathan Granot. 2003. "The Evolution of a Structured Relativistic Jet and Gamma-Ray Burst Afterglow Light Curves." *The Astrophysical Journal* 591 (2): 1075. http://stacks.iop.org/0004-637X/591/i=2/a=1075.

Lafler, J, and TD Kinman. 1965. "An RR Lyrae Star Survey with Ihe Lick 20-INCH Astrograph II. The Calculation of RR Lyrae Periods by Electronic Computer." *The Astrophysical Journal Supplement Series* 11:216.

Lambrechts, M., and A. Johansen. 2012. "Rapid growth of gas-giant cores by pebble accretion." *Astronomy & Astrophysics* 544, A32 (August): A32. doi:10.1051/0004-6361/201219127. arXiv: 1205.3030 [astro-ph.EP].

Lang, Dustin, David W. Hogg, Keir Mierle, Michael Blanton, and Sam Roweis. 2010. "Astrometry.net: Blind Astrometric Calibration of Arbitrary Astronomical Images." *The Astronomical Journal* 139 (May): 1782–1800. doi:10.1088/0004-6256/139/5/1782. arXiv: 0910.2233 [astro-ph.IM].

Lattimer, J. M., and D. N. Schramm. 1974. "Black-hole-neutron-star collisions." *The Astrophysical Journal Letters* 192 (September): L145–L147. doi:10.1086/181612.

———. 1976. "The tidal disruption of neutron stars by black holes in close binaries." *The Astrophysical Journal* 210 (December): 549–567. doi:10.1086/154860.

Law, C. J., B. M. Gaensler, B. D. Metzger, E. O. Ofek, and L. Sironi. 2018. "Discovery of the Luminous, Decades-long, Extragalactic Radio Transient FIRST J141918.9+394036." *The Astrophysical Journal* 866, L22 (October): L22. doi:10.3847/2041-8213/aae5f3. arXiv: 1808.08964 [astro-ph.HE].

Law, Nicholas M., Shrinivas R. Kulkarni, Richard G. Dekany, Eran O. Ofek, Robert M. Quimby, Peter E. Nugent, Jason Surace, et al. 2009. "The Palomar Transient Factory: System Overview, Performance, and First Results." *Publications of the Astronomical Society of the Pacific* 121 (December): 1395. doi:10.1086/648598. arXiv: 0906.5350 [astro-ph.IM].

Lawson, W.D., S. Nielsen, E.H. Putley, and A.S. Young. 1959. "Preparation and properties of HgTe and mixed crystals of HgTe-CdTe." *Journal of Physics and Chemistry of Solids* 9 (3): 325–329. doi:https://doi.org/10.1016/0022-3697(59)90110-6.

Le, Truong, and Vedant Mehta. 2017. "Revisiting the Redshift Distribution of Gamma-Ray Bursts in the Swift Era." *The Astrophysical Journal* 837, 17 (March): 17. doi:10.3847/1538-4357/aa5fa7. arXiv: 1702.03338 [astro-ph.HE].

Lewin, Walter H. G., Jan van Paradijs, and Edward P.J. van den Heuvel. 1997. *X-Ray Binaries (Cambridge Astrophysics).* Cambridge University Press, January. https://www.xarg.org/ref/a/0521599342/.

Li, Liang, En-Wei Liang, Qing-Wen Tang, Jie-Min Chen, Shao-Qiang Xi, Hou-Jun Lü, He Gao, et al. 2012. "A Comprehensive Study of Gamma-Ray Burst Optical Emission. I. Flares and Early Shallow-decay Component." *The Astrophysical Journal* 758 (1): 27. http://stacks.iop.org/0004-637X/758/i=1/a=27.

Li, Li-Xin, and Bohdan Paczyński. 1998a. "Transient Events from Neutron Star Mergers." *The Astrophysical Journal* 507 (November): L59–L62. doi:10.1086/311680. arXiv: astro-ph/9807272 [astro-ph].

Li, Li-Xin, and Bohdan Paczyński. 1998b. "Transient Events from Neutron Star Mergers." *The Astrophysical Journal* 507, no. 1 (November): L59–L62. doi:10.1086/311680.

Lipunov, V. M., K. A. Postnov, and M. E. Prokhorov. 1997. "Formation and coalescence of relativistic binary stars: the effect of kick velocity." *Monthly Notices of the Royal Astronomical Society* 288 (June): 245–259. doi:10.1093/mnras/288.1.245. arXiv: astro-ph/9702060 [astro-ph].

———. 2001. "Gamma-Ray Bursts as Standard-Energy Explosions." *Astronomy Reports* 45 (March): 236–240. doi:10.1134/1.1353364. arXiv: astro-ph/9908136 [astro-ph].

Lipunov, Vladimir, Victor Kornilov, Evgeny Gorbovskoy, Nikolaj Shatskij, Dmitry Kuvshinov, Nataly Tyurina, Alexander Belinski, et al. 2010. "Master Robotic Net." *Advances in Astronomy* 2010, 349171 (January): 349171. doi:10.1155/2010/349171. arXiv: 0907.0827 [astro-ph.HE].

Littlejohns, O. M., N. R. Butler, A. Cucchiara, A. M. Watson, O. D. Fox, W. H. Lee, A. S. Kutyrev, et al. 2015. "A detailed study of the optical attenuation of gamma-ray bursts in the Swift era." *Monthly Notices of the Royal Astronomical Society* 449 (May): 2919–2936. doi:10.1093/mnras/stv479. arXiv: 1412.6530 [astro-ph.HE].

Littlejohns, O. M., N. R. Butler, A. Cucchiara, A. M. Watson, A. S. Kutyrev, W. H. Lee, M. G. Richer, et al. 2014. "Identifying High-redshift Gamma-Ray Bursts with RATIR." *The Astronomical Journal* 148, 2 (July): 2. doi:10.1088/0004-6256/148/1/2. arXiv: 1312.3967 [astro-ph.HE].

Logue, J., C. D. Ott, I. S. Heng, P. Kalmus, and J. H. C. Scargill. 2012. "Inferring core-collapse supernova physics with gravitational waves." *Physical Review D* 86 (4): 044023. doi:10.1103/PhysRevD.86.044023.

Lorimer, D. R., M. Bailes, M. A. McLaughlin, D. J. Narkevic, and F. Crawford. 2007. "A Bright Millisecond Radio Burst of Extragalactic Origin." *Science* 318 (November): 777. doi:10.1126/science.1147532. arXiv: 0709.4301 [astro-ph].

Lynds, R. 1971. "The Absorption-Line Spectrum of 4c 05.34." *The Astrophysical Journal Letters* 164 (March): L73. doi:10.1086/180695.

Mackay, Craig D. 1986. "Charge-coupled devices in astronomy." *Annual review of astronomy and astrophysics* 24 (1): 255–283.

Macleod, H Angus, and H Angus Macleod. 2010. *Thin-film optical filters.* CRC press.

Madore, Barry F, and Wendy L Freedman. 1991. "The Cepheid distance scale." *Publications of the Astronomical Society of the Pacific* 103 (667): 933.

Maeder, André. 2009. *Physics, Formation and Evolution of Rotating Stars* [in eng]. Astronomy and Astrophysics Library. Berlin, Heidelberg: Springer Berlin Heidelberg.

Mahabal, AA, SG Djorgovski, AJ Drake, C Donalek, MJ Graham, RD Williams, Y Chen, B Moghaddam, M Turmon, E Beshore, et al. 2011. "Discovery, classification, and scientific exploration of transient events from the Catalina Real-time Transient Survey." *arXiv preprint arXiv:1111.0313.*

Mandel, Kaisey S., Gautham Narayan, and Robert P. Kirshner. 2011. "Type Ia Supernova Light Curve Inference: Hierarchical Models in the Optical and Near-infrared." *The Astrophysical Journal* 731, 120 (April): 120. doi:10.1088/0004-637X/731/2/120. arXiv: 1011.5910 [astro-ph.CO].

Mann, Andrew W., Eric Gaidos, and Greg Aldering. 2011. "Ground-Based Submillimagnitude CCD Photometry of Bright Stars Using Snapshot Observations." *Publications of the Astronomical Society of the Pacific* 123 (November): 1273. doi:10.1086/662640. arXiv: 1109.1358 [astro-ph.EP].

Mao, Ji-Rong, and Jian-Cheng Wang. 2001. "Hydrodynamic Evolution of GRB Afterglow." *Chinese Journal of Astronomy and Astrophysics* 1 (4): 349. http://stacks.iop.org/1009-9271/1/i=4/a=349.

Marples, P., G. Bock, and S. Parker. 2016. *ATel #8651: Bright PSN in NGC5128 (Centaurus A) Discovered By Backyard Observatory Supernova Search (BOSS).* http://www.astronomerstelegram.org/?read=8651.

Mayor, M., and D. Queloz. 1995. "A Jupiter-mass companion to a solar-type star." *Nature* 378 (November): 355–359. doi:10.1038/378355a0.

Mazzali, Paolo A., Friedrich K. Röpke, Stefano Benetti, and Wolfgang Hillebrandt. 2007. "A Common Explosion Mechanism for Type Ia Supernovae." *Science* 315 (February): 825. doi:10.1126/science.1136259. arXiv: astro-ph/0702351 [astro-ph].

Meade, Bernard, Christopher Fluke, Jeff Cooke, Igor Andreoni, Tyler Pritchard, Christopher Curtin, Stephanie R. Bernard, et al. 2017. "Collaborative Workspaces to Accelerate Discovery." *Publications of the Astronomical Society of Australia* 34, e023 (May): e023. doi:10.1017/pasa.2017.15. arXiv: 1704.01281 [astro-ph.IM].

Meegan, Charles, Giselher Lichti, P. N. Bhat, Elisabetta Bissaldi, Michael S. Briggs, Valerie Connaughton, Roland Diehl, et al. 2009. "THE fermi gamma-ray burst monitor." *The Astrophysical Journal* 702 (1): 791. http://stacks.iop.org/0004-637X/702/i=1/a=791.

Mészáros, P., and M. J. Rees. 1997. "Optical and Long-Wavelength Afterglow from Gamma-Ray Bursts." *The Astrophysical Journal* 476 (February): 232–237. doi:10.1086/303625. eprint: astro-ph/9606043.

Meszaros, P., M. J. Rees, and H. Papathanassiou. 1994. "Spectral properties of blast-wave models of gamma-ray burst sources." *The Astrophysical Journal* 432 (September): 181–193. doi:10.1086/174559. eprint: astro-ph/9311071.

Metzger, B. D., G. Martınez-Pinedo, S. Darbha, E. Quataert, A. Arcones, D. Kasen, R. Thomas, P. Nugent, I. V. Panov, and N. T. Zinner. 2010. "Electromagnetic counterparts of compact object mergers powered by the radioactive decay of r-process nuclei." *Monthly Notices of the Royal Astronomical Society* 406 (August): 2650–2662. doi:10.1111/j.1365-2966.2010.16864.x. arXiv: 1001.5029 [astro-ph.HE].

Metzger, Brian D. 2017. "Kilonovae." *Living Reviews in Relativity* 20, no. 1 (May): 3. doi:10.1007/s41114-017-0006-z.

Mink, S. E. de, and A. King. 2017. "Electromagnetic Signals Following Stellar-mass Black Hole Mergers." *The Astrophysical Journal Letters* 839, no. 1 (April): L7. doi:10.3847/2041-8213/aa67f3.

Monet, D., B. Canzian, H. Harris, N. Reid, A. Rhodes, and S. Sell. 1998. "VizieR Online Data Catalog: The PMM USNO-A1.0 Catalogue (Monet 1997)." *VizieR Online Data Catalog* 1243 (July).

Morganson, E., R. A. Gruendl, F. Menanteau, M. Carrasco Kind, Y.-C. Chen, G. Daues, A. Drlica-Wagner, et al. 2018. "The Dark Energy Survey Image Processing Pipeline." *Publications of the Astronomical Society of the Pacific* 130, no. 989 (May): 074501. doi:10.1088/1538-3873/aab4ef.

Nagayama, Takahiro, Nami Takeuchi, Takuma Kokusho, Asa Yamanaka, Miho Nishiyama, and Hidehiro Kaneda. 2014. "Evaluation of InGaAs 640x512 detector array manufactured by Chunghwa Leading Photonics Tech," vol. 9154. doi:10.1117/12.2055084.

Nakar, Ehud. 2007. “Short-hard gamma-ray bursts.” The Hans Bethe Centennial Volume 1906-2006, *Physics Reports* 442 (1): 166–236. doi:https://doi.org/10.1016/j.physrep.2007.02.005.

Narayan, Gautham, Tayeb Zaidi, Monika D. Soraisam, Zhe Wang, Michelle Lochner, Thomas Matheson, Abhijit Saha, et al. 2018. “Machine-learning-based Brokers for Real-time Classification of the LSST Alert Stream.” *The Astrophysical Journal Supplement Series* 236, no. 1 (May): 9. doi:10.3847/1538-4365/aab781.

Narayan, R., T. Piran, and A. Shemi. 1991. “Neutron star and black hole binaries in the Galaxy.” *The Astrophysical Journal Letters* 379 (September): L17–L20. doi:10.1086/186143.

Neilson, H. R., and J. B. Lester. 2011a. “Limb darkening in spherical stellar atmospheres.” *Astronomy & Astrophysics* 530, A65 (June): A65. doi:10.1051/0004-6361/201116623. arXiv: 1105.0197 `[astro-ph.SR]`.

———. 2011b. “Limb darkening in spherical stellar atmospheres.” *Astronomy & Astrophysics* 530, A65 (June): A65. doi:10.1051/0004-6361/201116623. arXiv: 1105.0197 `[astro-ph.SR]`.

Nishimura, H, M Sakata, T Tsujimoto, and M Nakayama. 1995. “Origin of the 4.1-eV luminescence in pure CsI scintillator.” *Physical Review B* 51 (4): 2167.

Norton, P. 2002. “HgCdTe Infrared Detectors.” *Opto-Electronics Review* 10:159. https://ci.nii.ac.jp/naid/10013323278/en/.

Osterman, Steve, Gabriel G. Ycas, Scott A. Diddams, Franklyn Quinlan, Suvrath Mahadevan, Lawrence Ramsey, Chad F. Bender, et al. 2012. “A near-infrared frequency comb for Y+J band astronomical spectroscopy.” In *Modern Technologies in Space- and Ground-based Telescopes and Instrumentation II,* 8450:84501I. Society of Photo-Optical Instrumentation Engineers (SPIE) Conference Series. September. doi:10.1117/12.926868. arXiv: 1209.3295 `[astro-ph.IM]`.

Ott, C. D., C. Reisswig, E. Schnetter, E. O’Connor, U. Sperhake, F. Löffler, P. Diener, E. Abdikamalov, I. Hawke, and A. Burrows. 2011. “Dynamics and Gravitational Wave Signature of Collapsar Formation.” *Physical Review Letters* 106, 161103 (April): 161103. doi:10.1103/PhysRevLett.106.161103. arXiv: 1012.1853 `[astro-ph.HE]`.

Paczynski, Bohdan, and James E. Rhoads. 1993. “Radio Transients from Gamma-Ray Bursters.” *The Astrophysical Journal* 418 (November): L5. doi:10.1086/187102. arXiv: astro-ph/9307024 `[astro-ph]`.

Panaitescu, A. 2007. “Jet breaks in the X-ray light-curves of Swift gamma-ray burst afterglows.” *Monthly Notices of the Royal Astronomical Society* 380 (1): 374–380. doi:10.1111/j.1365-2966.2007.12084.x. eprint: /oup/backfile/content_public/journal/mnras/380/1/10.1111/j.1365-2966.2007.12084.x/2/mnras0380-0374.pdf.

Panaitescu, A., P. Mészáros, and M. J. Rees. 1998. “Multiwavelength Afterglows in Gamma-Ray Bursts: Refreshed Shock and Jet Effects.” *The Astrophysical Journal* 503 (1): 314. http://stacks.iop.org/0004-637X/503/i=1/a=314.

Paradijs, J. van, P. J. Groot, T. Galama, C. Kouveliotou, R. G. Strom, J. Telting, R. G. M. Rutten, et al. 1997. “Transient optical emission from the error box of the g-ray burst of 28 February 1997.” *Nature* 386 (6626): 686–689. doi:10.1038/386686a0.

Pashchenko, Ilya N., Kirill V. Sokolovsky, and Panagiotis Gavras. 2018. “Machine learning search for variable stars.” *Monthly Notices of the Royal Astronomical Society* 475 (April): 2326–2343. doi:10.1093/mnras/stx3222. arXiv: 1710.07290 [astro-ph.IM].

Pearsall, T. P., and R. W. Hopson. 1977. “Growth and characterization of lattice-matched epitaxial films of GaxIn1xAs/InP by liquidphase epitaxy.” *Journal of Applied Physics* 48 (10): 4407–4409. doi:10.1063/1.323399. eprint: https://doi.org/10.1063/1.323399.

Pearsall, T. P., M. Quillec, and M. A. Pollack. 1979. “The effect of substrate orientation on the liquidsolid distribution coefficients for GaxIn1xAs in the temperature range 600–700°C.” *Applied Physics Letters* 35 (4): 342–344. doi:10.1063/1.91115. eprint: https://doi.org/10.1063/1.91115.

Pei, Y. C. 1992. “Interstellar dust from the Milky Way to the Magellanic Clouds.” *The Astrophysical Journal* 395 (August): 130–139. doi:10.1086/171637.

Peng, Fang, Arieh Königl, and Jonathan Granot. 2005. “Two-Component Jet Models of Gamma-Ray Burst Sources.” *The Astrophysical Journal* 626 (2): 966. http://stacks.iop.org/0004-637X/626/i=2/a=966.

Perley, Daniel A., Yuu Niino, Nial R. Tanvir, Susanna D. Vergani, and Johan P. U. Fynbo. 2016. “Long-Duration Gamma-Ray Burst Host Galaxies in Emission and Absorption.” *Space SCience Reviews* 202 (December): 111–142. doi:10.1007/s11214-016-0237-4. arXiv: 1602.00770 [astro-ph.HE].

Perley, R. A., F. R. Schwab, and A. H. Bridle, eds. 1989. “Synthesis imaging in radio astronomy.” In *Synthesis Imaging in Radio Astronomy,* vol. 6. Astronomical Society of the Pacific Conference Series.

Persson, S. E., D. C. Murphy, S. M. Gunnels, C. Birk, A. Bagish, and E. Koch. 2002. “The Las Campanas Infrared Survey Camera.” *The Astronomical Journal* 124 (1): 619. http://stacks.iop.org/1538-3881/124/i=1/a=619.

Petrov, RG, F Malbet, G Weigelt, P Antonelli, U Beckmann, Y Bresson, A Chelli, M Dugué, G Duvert, S Gennari, et al. 2007. “AMBER, the near-infrared spectro-interferometric three-telescope VLTI instrument.” *Astronomy & Astrophysics* 464 (1): 1–12.

Pierce, Michael J., Douglas L. Welch, Robert D. McClure, Sidney van den Bergh, Renè Racine, and Peter B. Stetson. 1994. “The Hubble constant and Virgo cluster distance from observations of Cepheid variables.” *Nature* 371 (6496): 385–389. doi:10.1038/371385a0.

Piran, Tsvi. 2005. “Magnetic Fields in Gamma-Ray Bursts: A Short Overview.” In *Magnetic Fields in the Universe: From Laboratory and Stars to Primordial Structures.* Edited by Elisabete M. de Gouveia dal Pino, Germán Lugones, and Alexander Lazarian, 784:164–174. American Institute of Physics Conference Series. September. doi:10.1063/1.2077181. arXiv: astro-ph/0503060 [astro-ph].

Piran, Tsvi, Doron Grossman, Oleg Korobkin, and Stephan Rosswog. 2014. “The long-term evolution of neutron star merger remnants – II. Radioactively powered transients.” *Monthly Notices of the Royal Astronomical Society* 439, no. 1 (January): 757–770. doi:10.1093/mnras/stt2503. eprint: http://oup.prod.sis.lan/mnras/article-pdf/439/1/757/5605854/stt2503.pdf.

Powell, Jade, Sarah E. Gossan, Joshua Logue, and Ik Siong Heng. 2016. “Inferring the core-collapse supernova explosion mechanism with gravitational waves.” *Physical Review D* 94, 123012 (December): 123012. doi:10.1103/PhysRevD.94.123012. arXiv: 1610.05573 [astro-ph.HE].

Priddey, Robert S., Robert Chapman, Nial R. Tanvir, and Andrew J. Levan. 2007. “How common are long gamma-ray bursts in the local Universe?” *Monthly Notices of the Royal Astronomical Society: Letters* 382, no. 1 (November): L21–L25. doi:10.1111/j.1745-3933.2007.00381.x. eprint: http://oup.prod.sis.lan/mnrasl/article-pdf/382/1/L21/6181677/382-1-L21.pdf.

Puig-Suari, Jordi, Clark Turner, and William Ahlgren. 2001. "Development of the standard CubeSat deployer and a CubeSat class PicoSatellite." In *2001 IEEE Aerospace Conference Proceedings (Cat. No. 01TH8542),* 1:1–347. IEEE.

Racusin, J. L., S. V. Karpov, M. Sokolowski, J. Granot, X. F. Wu, V. Pal'Shin, S. Covino, et al. 2008. "Broadband observations of the naked-eye γ-ray burst GRB080319B." *Nature* 455 (September): 183–188. doi:10.1038/nature07270. arXiv: 0805.1557.

Racusin, J. L., J. S. Perkins, M. S. Briggs, G. De Nolfo, J. Krizmanic, V. Connaughton, and J. E. McEnery. 2016. "BurstCube: A CubeSat for Gravitational Wave Counterparts." In *American Astronomical Society Meeting Abstracts #227,* 227:147.26. American Astronomical Society Meeting Abstracts. January.

Rafikov, Roman R. 2008. "Cooling of Young Stars Growing by Disk Accretion." *The Astrophysical Journal* 682 (July): 527–541. doi:10.1086/588420. arXiv: 0707.3636 `[astro-ph]`.

Rau, A., J. Greiner, S. Klose, J. Castro Cerón, A. Fruchter, A. Küpcü Yoldaș, J. Gorosabel, A. Levan, J. Rhoads, and N. Tanvir. 2004. "Discovery of the Faint Near-IR Afterglow of GRB 030528." In *Gamma-Ray Bursts: 30 Years of Discovery,* edited by E. Fenimore and M. Galassi, 727:439–442. American Institute of Physics Conference Series. September. doi:10.1063/1.1810882. arXiv: astro-ph/0312102 `[astro-ph]`.

Rau, A., S. R. Kulkarni, E. O. Ofek, and L. Yan. 2007. "SpitzerObservations of the New Luminous Red Nova M85 OT2006-1." *The Astrophysical Journal* 659, no. 2 (April): 1536–1540. doi:10.1086/512672.

Rees, M. J., and P. Meszaros. 1994. "Unsteady outflow models for cosmological gamma-ray bursts." *The Astrophysical Journal Letters* 430 (August): L93–L96. doi:10.1086/187446. eprint: astro-ph/9404038.

Reiners, A., D. Homeier, P. H. Hauschildt, and F. Allard. 2007. "A high resolution spectral atlas of brown dwarfs." *Astronomy & Astrophysics* 473 (October): 245–255. doi:10.1051/0004-6361:20077963. arXiv: 0707.2652 `[astro-ph]`.

Remillard, Ronald A., and Jeffrey E. McClintock. 2006. "X-Ray Properties of Black-Hole Binaries." *Annual Review of Astronomy and Astrophysics* 44 (1): 49–92. doi:10.1146/annurev.astro.44.051905.092532. eprint: https://doi.org/10.1146/annurev.astro.44.051905.092532.

Rhoads, James E. 1997. "How to Tell a Jet from a Balloon: A Proposed Test for Beaming in Gamma-Ray Bursts." *The Astrophysical Journal Letters* 487 (1): L1. http://stacks.iop.org/1538-4357/487/i=1/a=L1.

———. 1999. "The Dynamics and Light Curves of Beamed Gamma-Ray Burst Afterglows." *The Astrophysical Journal* 525 (2): 737. http://stacks.iop.org/0004-637X/525/i=2/a=737.

Ricker, George R, DW Latham, RK Vanderspek, KA Ennico, G Bakos, TM Brown, AJ Burgasser, D Charbonneau, M Clampin, LD Deming, et al. 2010. "Transiting Exoplanet Survey Satellite (TESS)." In *Bulletin of the American Astronomical Society,* 42:459.

Ricker, George R., Joshua N. Winn, Roland Vanderspek, David W. Latham, Gáspár Á. Bakos, Jacob L. Bean, Zachory K. Berta-Thompson, et al. 2014. "Transiting Exoplanet Survey Satellite." *Journal of Astronomical Telescopes, Instruments, and Systems* 1 (1): 1–10. doi:10.1117/1.JATIS.1.1.014003.

Riess, Adam G., Alexei V. Filippenko, Peter Challis, Alejandro Clocchiatti, Alan Diercks, Peter M. Garnavich, Ron L. Gilliland, et al. 1998. "Observational Evidence from Supernovae for an Accelerating Universe and a Cosmological Constant." *Astronomical Journal* 116 (September): 1009–1038. doi:10.1086/300499. arXiv: astro-ph/9805201 `[astro-ph]`.

Roming, Peter W. A., Thomas E. Kennedy, Keith O. Mason, John A. Nousek, Lindy Ahr, Richard E. Bingham, Patrick S. Broos, et al. 2005. "The Swift Ultra-Violet/Optical Telescope." *Space Science Reviews* 120, no. 3 (October): 95–142. doi:10.1007/s11214-005-5095-4.

Rossi, E., D. Lazzati, J. D. Salmonson, and G. Ghisellini. 2002. "Polarization curves of GRB afterglows predicted by the universal jet structure." In *Beaming and Jets in Gamma Ray Bursts,* edited by Rachid Ouyed, 88. January. arXiv: astro-ph/0211020 `[astro-ph]`.

Rosswog, S. 2005. "Mergers of Neutron Star–Black Hole Binaries with Small Mass Ratios: Nucleosynthesis, Gamma-Ray Bursts, and Electromagnetic Transients." *The Astrophysical Journal* 634, no. 2 (December): 1202–1213. doi:10.1086/497062.

Rybicki, G. B., and A. P. Lightman. 1986. *Radiative Processes in Astrophysics,* 400. June.

Sagert, I., T. Fischer, M. Hempel, G. Pagliara, J. Schaffner-Bielich, A. Mezzacappa, F. -K. Thielemann, and M. Liebendörfer. 2009. "Signals of the QCD Phase

Transition in Core-Collapse Supernovae.” *Physicla Review Letters* 102, 081101 (February): 081101. doi:10.1103/PhysRevLett.102.081101. arXiv: 0809.4225 `[astro-ph]`.

Sari, Re’em, Tsvi Piran, and J. P. Halpern. 1999. “Jets in Gamma-Ray Bursts.” *The Astrophysical Journal Letters* 519 (1): L17. http://stacks.iop.org/1538-4357/519/i=1/a=L17.

Sari, Re’em, Tsvi Piran, and Ramesh Narayan. 1998. “Spectra and Light Curves of Gamma-Ray Burst Afterglows.” *The Astrophysical Journal Letters* 497 (1): L17. http://stacks.iop.org/1538-4357/497/i=1/a=L17.

Schaefer, Bradley E. 2010. “Comprehensive photometric histories of all known Galactic recurrent novae.” *The Astrophysical Journal Supplement Series* 187 (2): 275.

Schwieterman, Edward W., Nancy Y. Kiang, Mary N. Parenteau, Chester E. Harman, Shiladitya DasSarma, Theresa M. Fisher, Giada N. Arney, et al. 2018. “Exoplanet Biosignatures: A Review of Remotely Detectable Signs of Life.” *Astrobiology* 18 (June): 663–708. doi:10.1089/ast.2017.1729. arXiv: 1705.05791 `[astro-ph.EP]`.

Sivanandam, Suresh, James R. Graham, Roberto Abraham, Anthony Tekatch, Eric Steinbring, Wayne Ngan, Doug L. Welch, and Nicholas M. Law. 2012. “Characterizing near-infrared sky brightness in the Canadian high arctic.” In *Ground-based and Airborne Instrumentation for Astronomy IV,* 8446:844643. Society of Photo-Optical Instrumentation Engineers (SPIE) Conference Series. September. doi:10.1117/12.926251. arXiv: 1206.6901 `[astro-ph.IM]`.

Skrutskie, M. F., R. M. Cutri, R. Stiening, M. D. Weinberg, S. Schneider, J. M. Carpenter, C. Beichman, et al. 2006. “The Two Micron All Sky Survey (2MASS).” *The Astronomical Journal* 131 (February): 1163–1183. doi:10.1086/498708.

Smith, Horace A. 2004. *RR Lyrae stars.* Vol. 27. Cambridge University Press.

Snytnikov, V. N., and O. P. Stoyanovskaya. 2013. “Clump formation due to the gravitational instability of a multiphase medium in a massive protoplanetary disc.” *Monthly Notices of the Royal Astronomical Society* 428 (January): 2–12. doi:10.1093/mnras/sts002. arXiv: 1210.0971 `[astro-ph.EP]`.

Strausbaugh, Robert, Nathaniel Butler, William H. Lee, Eleonora Troja, and Alan M. Watson. 2019. “Evidence for a Bright-edged Jet in the Optical/Near-infrared Afterglow of GRB 160625B.” *The Astrophysical Journal* 873, no. 1 (March): L6. doi:10.3847/2041-8213/ab07c0.

Strausbaugh, Robert, Rebecca Jackson, and Nathaniel Butler. 2018. "Night Vision for Small Telescopes." *Publications of the Astronomical Society of the Pacific* 130 (September): 095001. doi:10.1088/1538-3873/aaca2a. arXiv: 1806.04221 [astro-ph.IM].

Sullivan, M., A. Conley, D. A. Howell, J. D. Neill, P. Astier, C. Balland, S. Basa, et al. 2010. "The dependence of Type Ia Supernovae luminosities on their host galaxies." *Monthly Notices of the Royal Astronomical Society* 406 (August): 782–802. doi:10.1111/j.1365-2966.2010.16731.x. arXiv: 1003.5119 [astro-ph.CO].

Sullivan, Peter W., Bryce Croll, and Robert A. Simcoe. 2013. "Precision of a Low-Cost InGaAs Detector for Near Infrared Photometry." *Publications of the Astronomical Society of the Pacific* 125 (September): 1021. doi:10.1086/672573. arXiv: 1307.1469 [astro-ph.IM].

Sullivan, Peter W., and Robert A. Simcoe. 2012. "A Calibrated Measurement of the Near-IR Continuum Sky Brightness Using Magellan/FIRE." *Publications of the Astronomical Society of the Pacific* 124 (December): 1336. doi:10.1086/668849. arXiv: 1207.0817 [astro-ph.IM].

Summerscales, T. Z., Adam Burrows, Lee Samuel Finn, and Christian D. Ott. 2008. "Maximum Entropy for Gravitational Wave Data Analysis: Inferring the Physical Parameters of Core-Collapse Supernovae." *The Astrophysical Journal* 678, no. 2 (May): 1142–1157. doi:10.1086/528362.

Tanvir, N. R., A. J. Levan, A. S. Fruchter, J. Hjorth, R. A. Hounsell, K. Wiersema, and R. L. Tunnicliffe. 2013. "A 'kilonova' associated with the short-duration γ-ray burst GRB 130603B." *Nature* 500 (August): 547–549. doi:10.1038/nature12505. arXiv: 1306.4971 [astro-ph.HE].

Thebault, P., Q. Kral, and S. Ertel. 2012. "Planet signatures in collisionally active debris discs: scattered light images." *Astronomy & Astrophysics* 547, A92 (November): A92. doi:10.1051/0004-6361/201219962. arXiv: 1209.3969 [astro-ph.EP].

Thompson, Anthony Richard, James M Moran, George Warner Swenson, et al. 1986. *Interferometry and synthesis in radio astronomy.* Wiley New York et al.

Totani, Tomonori, and Alin Panaitescu. 2002. "Orphan Afterglows of Collimated Gamma-Ray Bursts: Rate Predictions and Prospects for Detection." *The Astrophysical Journal* 576 (September): 120–134. doi:10.1086/341738. arXiv: astro-ph/0204258 [astro-ph].

Troja, E., V. M. Lipunov, C. G. Mundell, N. R. Butler, A. M. Watson, S. Kobayashi, S. B. Cenko, et al. 2017. "Significant and variable linear polarization during the prompt optical flash of GRB 160625B." *Nature* 547 (July): 425. https://doi.org/10.1038/nature23289.

Turner, D. G. 1996. "The Progenitors of Classical Cepheid Variables." *Journal of the RAS of Canada* 90 (April): 82.

van Eerten, Hendrik. 2013. "Gamma-ray burst afterglow theory." *arXiv e-prints,* arXiv:1309.3869 (September): arXiv:1309.3869. arXiv: 1309.3869 [astro-ph.HE].

Vohl, Dany, Tyler Pritchard, Igor Andreoni, Jeffrey Cooke, and Bernard Meade. 2017. "Enabling Near Real-Time Remote Search for Fast Transient Events with Lossy Data Compression." *Publications of the Astronomical Society of Australia* 34, e038 (September): e038. doi:10.1017/pasa.2017.34. arXiv: 1708.04605 [astro-ph.IM].

Wagoner, Robert V. 1973. "Big-bang nucleosynthesis revisited." *The Astrophysical Journal* 179:343–360.

Wanderman, David, and Tsvi Piran. 2010. "The luminosity function and the rate of Swift's gamma-ray bursts." *Monthly Notices of the Royal Astronomical Society* 406 (3): 1944–1958. doi:10.1111/j.1365-2966.2010.16787.x. eprint: /oup/backfile/content_public/journal/mnras/406/3/10.1111/j.1365-2966.2010.16787.x/2/mnras0406-1944.pdf.

Warren, S. J., D. J. Mortlock, S. K. Leggett, D. J. Pinfield, D. Homeier, S. Dye, R. F. Jameson, et al. 2007. "A very cool brown dwarf in UKIDSS DR1." *Monthly Notices of the Royal Astronomical Society* 381 (November): 1400–1412. doi:10.1111/j.1365-2966.2007.12348.x. arXiv: 0708.0655 [astro-ph].

Watson, Alan M., William H. Lee, Eleonora Troja, Carlos G. Román-Zúñiga, Nathaniel R. Butler, Alexander S. Kutyrev, Neil A. Gehrels, et al. 2016. "DDOTI: the deca-degree optical transient imager." In *Observatory Operations: Strategies, Processes, and Systems VI,* vol. 9910, 99100G. Society of Photo-Optical Instrumentation Engineers (SPIE) Conference Series. July. doi:10.1117/12.2232898. arXiv: 1606.00695 [astro-ph.IM].

Waxman, E., and B. T. Draine. 2000. "Dust Sublimation by Gamma-ray Bursts and Its Implications." *The Astrophysical Journal* 537 (July): 796–802. doi:10.1086/309053. eprint: astro-ph/9909020.

Webbink, Ronald F, Mario Livio, James W Truran, and Marina Orio. 1987. "The nature of recurrent novae." In *International Astronomical Union Colloquium,* 93:493–495. Cambridge University Press.

Winn, Joshua N. 2010. "Transits and Occultations." *arXiv e-prints,* arXiv:1001.2010 (January): arXiv:1001.2010. arXiv: 1001.2010 `[astro-ph.EP]`.

Woods, Eric, and Abraham Loeb. 1999. "Constraints on Off-Axis X-Ray Emission from Beamed Gamma-Ray Bursts." *The Astrophysical Journal* 523 (1): 187. http://stacks.iop.org/0004-637X/523/i=1/a=187.

Woosley, S. E. 1993. "Gamma-ray bursts from stellar mass accretion disks around black holes." *The Astrophysical Journal* 405 (March): 273–277. doi:10.1086/172359.

Wygoda, N., D. Guetta, M. A. Mandich, and E. Waxman. 2016. "The Energy Budget of GRBs Based on a Large Sample of Prompt and Afterglow Observations." *The Astrophysical Journal* 824 (2): 127. http://stacks.iop.org/0004-637X/824/i=2/a=127.

Wygoda, N., E. Waxman, and D. A. Frail. 2011. "Relativistic Jet Dynamics and Calorimetry of Gamma-ray Bursts." *The Astrophysical Journal Letters* 738 (2): L23. http://stacks.iop.org/2041-8205/738/i=2/a=L23.

Xu, D., D. Malesani, J. P. U. Fynbo, N. R. Tanvir, A. J. Levan, and D. A. Perley. 2016. *GCN CIRCULAR 19600, GRB 160625B: VLT/X-shooter redshift.* https://gcn.gsfc.nasa.gov/other/160625B.gcn3.

Yoon, S-C, N Langer, and C Norman. 2006. "Single star progenitors of long gamma-ray bursts-I. Model grids and redshift dependent GRB rate." *Astronomy & Astrophysics* 460 (1): 199–208.

Zhang, Bing, Y. Z. Fan, Jaroslaw Dyks, Shiho Kobayashi, Peter Mészáros, David N. Burrows, John A. Nousek, and Neil Gehrels. 2006. "Physical Processes Shaping Gamma-Ray Burst X-Ray Afterglow Light Curves: Theoretical Implications from the Swift X-Ray Telescope Observations." *The Astrophysical Journal* 642 (1): 354. http://stacks.iop.org/0004-637X/642/i=1/a=354.

Zhang, Weiqun, and Andrew MacFadyen. 2009. "The Dynamics and Afterglow Radiation of Gamma-Ray Bursts. I. Constant Density Medium." *The Astrophysical Journal* 698 (2): 1261. http://stacks.iop.org/0004-637X/698/i=2/a=1261.

Zhang, Z. -B., and C. -S. Choi. 2008. "An analysis of the durations of Swift gamma-ray bursts." *Astronomy & Astrophysics* 484 (June): 293–297. doi:10.1051/0004-6361:20079210. arXiv: 0708.4049 [astro-ph].

APPENDIX A

GRB 160625B RATIR DATA

Table 4. RATIR GRB 160625B Data

Days after GRB	Exposure (minutes)	r	i	Z	Y	J	H
0.37	1.2	18.24 ± 0.01	18.05 ± 0.01	17.99 ± 0.01	17.90 ± 0.01	17.79 ± 0.01	17.65 ± 0.02
0.39	1.2	18.29 ± 0.01	18.11 ± 0.01	18.03 ± 0.01	17.96 ± 0.01	17.85 ± 0.01	17.69 ± 0.02
0.41	1.2	18.35 ± 0.01	18.17 ± 0.01	18.08 ± 0.01	18.01 ± 0.01	17.87 ± 0.01	17.71 ± 0.02
0.43	1.2	18.43 ± 0.01	18.23 ± 0.01	18.16 ± 0.01	18.07 ± 0.02	17.92 ± 0.01	17.82 ± 0.01
0.45	1.2	18.46 ± 0.01	18.28 ± 0.01	18.20 ± 0.01	18.14 ± 0.02	17.99 ± 0.01	17.83 ± 0.01
0.48	1.2	18.52 ± 0.01	18.33 ± 0.01	18.23 ± 0.01	18.15 ± 0.01	17.97 ± 0.01	17.85 ± 0.01
0.50	1.2	18.55 ± 0.01	18.36 ± 0.01	18.30 ± 0.01	18.22 ± 0.01	18.04 ± 0.01	17.92 ± 0.01
1.47	6.6	19.70 ± 0.01	19.51 ± 0.01	19.41 ± 0.02	19.28 ± 0.02	19.11 ± 0.02	18.96 ± 0.03
2.39	15.0	20.26 ± 0.03	19.99 ± 0.01	19.91 ± 0.01	19.79 ± 0.02	19.62 ± 0.02	19.45 ± 0.02
3.41	13.8	20.58 ± 0.01	20.38 ± 0.01	20.28 ± 0.02	20.15 ± 0.03	19.95 ± 0.03	19.80 ± 0.04
4.39	16.8	20.87 ± 0.01	20.66 ± 0.01	20.56 ± 0.02	20.44 ± 0.03	20.32 ± 0.04	20.00 ± 0.04
5.38	8.4	21.11 ± 0.02	20.89 ± 0.02	20.81 ± 0.04	20.59 ± 0.04	20.39 ± 0.05	20.12 ± 0.06
6.39	8.4	21.27 ± 0.02	21.06 ± 0.02	20.95 ± 0.05	20.72 ± 0.06	20.50 ± 0.07	20.35 ± 0.09
7.38	9.0	21.38 ± 0.02	21.17 ± 0.02	21.08 ± 0.04	20.96 ± 0.05	20.73 ± 0.06	20.50 ± 0.07
8.37	8.4	21.52 ± 0.04	21.39 ± 0.04	21.43 ± 0.11	20.95 ± 0.08	20.75 ± 0.12	20.41 ± 0.11
9.37	8.4	21.54 ± 0.02	21.37 ± 0.02	21.22 ± 0.05	21.10 ± 0.06	20.89 ± 0.08	20.55 ± 0.08
10.36	6.0	21.61 ± 0.03	21.47 ± 0.03	21.42 ± 0.07	21.23 ± 0.09	20.83 ± 0.09	20.64 ± 0.11
11.35	8.4	21.71 ± 0.02	21.50 ± 0.02	21.31 ± 0.05	21.15 ± 0.07	20.92 ± 0.08	20.91 ± 0.12
12.35	7.8	21.78 ± 0.03	21.57 ± 0.03	21.48 ± 0.07	21.35 ± 0.10	21.38 ± 0.16	20.91 ± 0.15
13.36	8.4	21.93 ± 0.03	21.69 ± 0.02	21.60 ± 0.06	21.49 ± 0.08	21.16 ± 0.08	21.02 ± 0.10
14.41	14.4	22.01 ± 0.03	21.83 ± 0.02	21.81 ± 0.07	21.63 ± 0.08	21.40 ± 0.11	21.10 ± 0.12
15.36	8.4	22.24 ± 0.05	22.00 ± 0.04	21.76 ± 0.09	21.92 ± 0.14	21.85 ± 0.18	21.11 ± 0.14
16.34	8.4	22.33 ± 0.05	22.12 ± 0.04	21.83 ± 0.09	21.78 ± 0.14	21.39 ± 0.14	21.33 ± 0.19
19.32	8.4	22.58 ± 0.07	22.34 ± 0.07	22.18 ± 0.15	22.51 ± 0.36	21.50 ± 0.22	21.04 ± 0.23
20.32	7.8	22.82 ± 0.11	22.51 ± 0.09	22.41 ± 0.18	22.14 ± 0.18	22.03 ± 0.23	21.77 ± 0.24
21.39	16.8	22.61 ± 0.13	22.54 ± 0.14	> 22.54	> 22.23	> 21.80	21.05 ± 0.28
22.32	8.4	22.81 ± 0.12	22.56 ± 0.11	22.61 ± 0.22	22.39 ± 0.24	22.34 ± 0.31	22.05 ± 0.34
23.38	15.6	22.84 ± 0.11	22.91 ± 0.13	22.48 ± 0.11	-	21.87 ± 0.10	-
24.38	16.2	22.90 ± 0.16	22.87 ± 0.17	23.14 ± 0.27	-	21.98 ± 0.12	-
25.39	18.0	22.85 ± 0.13	22.70 ± 0.13	22.66 ± 0.15	-	22.43 ± 0.18	-
26.37	16.2	23.03 ± 0.11	22.91 ± 0.11	22.86 ± 0.15	-	22.43 ± 0.17	-
39.39	8.4	24.10 ± 0.23	23.75 ± 0.19	-	-	-	-
40.39	7.2	23.71 ± 0.17	23.75 ± 0.20	-	-	-	-
41.39	7.2	23.98 ± 0.22	23.60 ± 0.17	-	-	-	-
41.89	5.4	-	-	23.57 ± 0.32	> 23.32	> 22.89	> 22.49
43.31	12.0	> 24.33	23.64 ± 0.21	-	-	-	-
44.36	70.8	24.01 ± 0.22	23.72 ± 0.18	-	-	-	-
52.92	190.2	> 23.54	-	-	-	-	-
53.92	307.8	-	24.08 ± 0.27	23.86 ± 0.33	-	> 23.36	-

Magnitudes are in AB system and are not corrected for galactic extinction.

APPENDIX B

GRB JET DERIVATIONS

The following derivation is for the emissivity of a GRB jet over time; the formulae below were used to model the afterglow emission of GRB 160625B, as plotted in Figure 27. The flux from a source with emissivity $j_\nu(t, \Omega)$ is:

$$f_\nu(t) = 2\pi D\Gamma^{-2} \int \varphi^2 d\varphi \int \frac{j'_\nu(t', \Omega')d\mu}{(1-\beta\mu)^2(1-\mu^2)^{3/2}} \tag{B.1}$$

where D is the distance from the source to the observer and φ is the angle to the jet edge as viewed by the observer.

We assume a spherical blast wave and a thin emitting shell with zero emissivity beyond the jet angle $\theta_{\text{jet}}/2$ and that the jet is viewed perfectly on axis. With these condition, the jet emissivity, j, is

$$j = A_0 t'^{-\alpha} \nu'^{-b} \delta(r - \beta ct) H(\theta_{\text{jet}}/2 - \theta) \tag{B.2}$$

Here, α is the power-law temporal index and b is the power-law spectral index. The rest-frame time, t', and the lab-frame time, t, are related by $t' = t + r\mu/c$, and r is the radius of the blast wave. The function H is the Heaviside function. The δ function is for a thin emitting shell. The Heaviside function states that flux is only originating inside the jet.

By making some substitutions, we can make the delta function apply to the parameter φ. First we replace t' with t.

$$\begin{aligned} \delta(r - \beta ct') &= \delta(r(1-\beta\mu) - \beta ct) \\ &= \delta(r - \beta c(t + \mu r/c)) \\ &= \delta(r - \beta ct + \beta\mu r) \\ &= \delta(r(1-\beta\mu) - \beta ct) \end{aligned} \tag{B.3}$$

Then we make use of the geometry of the system to inject φ using the following relationship; $D\varphi = r\sin(\theta)$. So,

$$
\begin{aligned}
\delta(r-\beta ct') &= \delta(r(1-\beta\mu)-\beta ct) \\
&= \delta\left(\varphi\left(\frac{D(1-\beta\mu)}{\sin(\theta)}\right)-\beta ct\right) \\
&= \delta\left(\frac{D(1-\beta\mu)}{\sin(\theta)}\left(\varphi-\frac{\sin(\theta)\beta ct}{D(1-\beta\mu}\right)\right) \\
&= \frac{\sin(\theta)}{D(1-\beta\mu)}\delta\left(\varphi-\frac{\sin(\theta)\beta ct}{D(1-\beta\mu)}\right)
\end{aligned}
\tag{B.4}
$$

We could pull that factor out of the δ by factoring it out of both terms.

Now, we integrate Equation B.1 over φ:

$$
\begin{aligned}
f_\nu(t) &= \frac{2\pi D}{\Gamma^2}\int\varphi^2 d\varphi\int A_0 t'^{-\alpha}\nu'^{-b}\frac{\delta(r-\beta ct)H(\theta_j/2-\theta)d\mu}{(1-\beta\mu)^2(1-\mu^2)^{3/2}} \\
&= \frac{2\pi D}{\Gamma^2}\int\varphi^2 d\varphi\int A_0 t'^{-\alpha}\nu'^{-b}\frac{\sin(\theta)}{D(1-\beta\mu)}\delta\left(\varphi-\frac{\sin(\theta)\beta ct}{D(1-\beta\mu)}\right)\frac{H(\theta_j/2-\theta)d\mu}{(1-\beta\mu)^2(1-\mu^2)^{3/2}} \\
&= \frac{2\pi}{\Gamma^2}\int d\mu\frac{\sin^2(\theta)\beta^2t^2c^2}{D^2(1-\beta\mu)^2}\frac{\sin(\theta)}{(1-\beta\mu)}A_0 t'^{-\alpha}\nu'^{-b}\frac{H(\theta_j/2-\theta)}{(1-\beta\mu)^2(1-\mu^2)^{3/2}} \\
&= 2\pi\left(\frac{\beta ct}{D\Gamma}\right)^2 A_0\int d\mu\frac{\sin^3(\theta)H(\theta_j/2-\theta)}{(1-\beta\mu)^3(1-\beta\mu)^2(1-\mu^2)^{3/2}}t'^{-\alpha}\nu'^{-b}
\end{aligned}
\tag{B.5}
$$

The $\sin^3(\theta)$ and $(1-\mu^2)^{3/2}$ terms cancel out using $\mu=\cos(\theta)$ and $1-\cos^2(\theta)=\sin^2(\theta)$.

Now we get ready to integrate over μ.

$$
f_\nu(t) = 2\pi\left(\frac{\beta ct}{D\Gamma}\right)^2 A_0\int\frac{d\mu t'^{-\alpha}\nu'^{-b}H(\theta_{\rm jet}/2-\theta)}{(1-\beta\mu)^5}
\tag{B.6}
$$

We have $\nu' = \nu\Gamma(1-\beta\mu)$ and $t' = t/(1-\beta\mu)$, so the integral goes to

$$\begin{aligned}
f_\nu(t) &= 2\pi\left(\frac{\beta ct}{D\Gamma}\right)^2 A_0 \int \frac{d\mu t^{-\alpha}\nu^{-b}\Gamma^{-b}(1-\beta\mu)^{-b}H(\theta_{\rm jet}/2-\theta)}{(1-\beta\mu)^{-\alpha}(1-\beta\mu)^5} \\
&= 2\pi(\beta ct/D)^2\Gamma^{-2-b}A_0 t^{-\alpha}\nu^{-b}\int_1^{\mu_{\rm min}} d\mu H(\theta_{\rm jet}/2-\theta)(1-\beta\mu)^{\alpha-b-5} \\
&= 2\pi(\beta ct/D)^2\Gamma^{-2-b}A_0 t^{-\alpha}\nu^{-b}\frac{-1}{(4-\alpha+b)(1-\beta\mu)^{4-\alpha+b}\beta}\Big|_1^{\mu_{\rm min}} \\
&= 2\pi\beta(ct/D)^2\Gamma^{-2-b}A_0 t^{-\alpha}\nu^{-b}\frac{-1}{\beta(4-\alpha+b)}\left((1-\beta\mu_{\rm min})^{\alpha-b-4}-(1-\beta)^{\alpha-b-4}\right) \\
&= 2\pi\beta(ct/D)^2\Gamma^{-2-b}A_0 t^{-\alpha}\nu^{-b}\frac{1}{\beta(4-\alpha+b)}\left((1-\beta)^{\alpha-b-4}-(1-\beta\mu_{\rm min})^{\alpha-b-4}\right) \\
&= 2\pi\beta(ct/D)^2\Gamma^{-2-b}A_0 t^{-\alpha}\nu^{-b}\frac{(1-\beta)^{\alpha-b-4}}{\beta(4-\alpha+b)}\left(1-\left[\frac{(1-\beta\mu_{\rm min}}{(1-\beta)}]\right)^{\alpha-b-4}\right) \\
&= 2\pi\beta(ct/D)^2\Gamma^{-2-b}A_0 t^{-\alpha}\nu^{-b}\frac{(1-\beta)^{\alpha-b-4}}{\beta(4-\alpha+b)}\left(1-\left[\frac{(1-\beta)}{(1-\beta\mu_{\rm min}}\right]^{4+b-\alpha}\right) \\
&= 2\pi\beta\left(\frac{c}{D}\right)^2\frac{t^{2-\alpha}\nu^{-b}}{\Gamma^{2+b}}\frac{(1-\beta)^{\alpha-4-b}}{(4-\alpha+b)}\left(1-\left[\frac{(1-\beta)}{(1-\beta\mu_{\rm min})}\right]^{4-\alpha+b}\right)
\end{aligned} \tag{B.7}$$

with $\mu_{\rm min} = cos(\theta_{\rm jet}/2)$.

The term in the square brackets goes to zero at early time, and the pre-factor is the flux due to a spherical, non-jetted blast wave, $f_{\nu,\,\rm sphere}$. We can ignore the lone β in the pre-factor in the ultra-relativistic limit ($\beta \approx 1$).

Defining, $F = f_\nu/f_{\nu,\,\rm sphere}$, we have:

$$F = 1 - [(1-\beta)/(1-\beta\mu_{\rm min})]^{4-\alpha+b} \approx 1-(1+(\Gamma\theta_{\rm jet}/2)^2)^{-n} \tag{B.8}$$

where we have taken the small angle limit. This simplification is non-trivial and is shown below:

$$
\begin{aligned}
1-[(1-\beta)/(1-\beta\mu_{\min})] &= \frac{1-\beta\mu}{1-\beta\mu}-\frac{1-\beta}{1-\beta\mu} \\
&= \frac{1-\beta\mu-1+\beta}{1-\beta\mu} \\
&= \frac{\beta-\beta\mu}{1-\beta\mu} \\
&= \frac{\beta-\beta\cos(\theta)}{1-\beta\cos(\theta)} \\
&\approx \frac{\beta-\beta(1-\theta^2/2)}{1-\beta(1-\theta^2/2} \\
&\approx \frac{\beta-\beta+\beta\theta^2/2}{1-\beta+\beta\theta^2/2} \\
&\approx \frac{\beta\theta^2/2}{1-\beta+\beta\theta^2/2} \\
&\approx \frac{2}{2}\frac{\beta\theta^2/2}{1-\beta+\beta\theta^2/2} \\
&\approx \frac{\beta\theta^2}{2(1-\beta)+\beta\theta^2} \\
&\approx \frac{1/(\beta\theta^2)}{1/(\beta\theta^2)}\frac{\beta\theta^2}{2(1-\beta)+\beta\theta^2} \\
&\approx \frac{1}{2(1-\beta)/(\beta\theta^2)+1} \\
&\approx \left[1+\frac{2(1-\beta)}{\beta\theta^2}\right]^{-1}
\end{aligned} \tag{B.9}
$$

Using the fact that $\beta \approx 1$, then $2(1-\beta) \approx (1-\beta)(1+\beta)$; we can also ignore the lone β term in the denominator. Plugging that in, we get

$$
\begin{aligned}
1-[(1-\beta)/(1-\beta\mu_{\min})] &\approx \left[1+\frac{2(1-\beta)}{\beta\theta^2}\right]^{-1} \\
&\approx \left[1+\frac{(1+\beta)(1-\beta)}{\theta^2}\right]^{-1} \\
&\approx \left[1+\frac{1-\beta^2}{\theta^2}\right]^{-1}
\end{aligned} \tag{B.10}
$$

Now we replace $1-\beta^2$ with Γ^2 using the definition of $\Gamma = 1/\sqrt{1-\beta^2}$, and use the ultra-relativistic limit ($\beta \approx 1$) to ignore any lone β terms.

$$\begin{aligned} 1-[(1-\beta)/(1-\beta\mu_{\min})] &\approx \left[1+\frac{1-\beta^2}{\beta\theta^2}\right]^{-1} \\ &\approx \left[1+\frac{1}{\Gamma^2\theta^2}\right]^{-1} \end{aligned} \tag{B.11}$$

If we raise all of this to the power n, we arrive at the Equation B.8.

So the final result for the flux is

$$f_\nu = 2\pi\beta\left(\frac{c}{D}\right)^2 \frac{t^{2-\alpha}\nu^{-b}}{\Gamma^{2+b}} \frac{(1-\beta)^n}{n} \left(1-(1+(\Gamma\theta_{\rm jet}/2)^2)^{-n}\right) \tag{B.12}$$

where $n = 4-\alpha+b$. We call the pre-factor, $Z = 2\pi\beta\left(\frac{c}{D}\right)^2 \frac{t^{2-\alpha}\nu^{-b}}{\Gamma^{2+b}} \frac{(1-\beta)^n}{n}$. This gives us the correct early and late-time behavior; it does not however explain the bump. To do that we modify our jet emissivity in Equation B.2 by adding an instantaneous emission at a time t'_0 resulting in

$$j = A_0 t'^{-\alpha}\nu'^{-b}\delta(r-\beta ct)(H(\theta_{\rm jet}/2-\theta) + j_e(\theta)\delta(t'-t'_0)t'_0) \tag{B.13}$$

Now our flux will have an extra component after time t'_0 The first part of the new jet emissivity j gives us the answer we derived showed in Equation B.12. Now lets treat the second part of the j separately and call its flux $f_e(t)$.

$$f_e(t) = \frac{2\pi D}{\Gamma^2}\int \varphi^2 d\varphi \int A_0 t'^{-\alpha}\nu'^{-b}\frac{\delta(r-\beta ct)j_e(\theta)\delta(t'-t'_0)t'_0 d\mu}{(1-\beta\mu)^2(1-\mu^2)^{3/2}} \tag{B.14}$$

Following the same procedure as Equations 3-5, we arrive at

$$f_e(t) = 2\pi\left(\frac{\beta c}{D}\right)^2 t^{2-\alpha}\nu^{-b}\Gamma^{-2-b}\int d\mu(1-\beta\mu)^{\alpha-5-b}j_e(\theta)\delta(t'-t'_0)t'_0 \tag{B.15}$$

Now we recast the δ into a function of θ, starting with the following relationships: $t' = t/(1-\beta\mu)$ and $t'_0 = t_0/(1-\beta)$.

$$
\begin{aligned}
\delta(t'-t'_0) &= \delta\left(\frac{t}{1-\beta\mu} - \frac{t_0}{1-\beta}\right) \\
&= \delta\left(\frac{t}{(1-\beta)(1+(\Gamma\theta)^2)} - \frac{t_0}{1-\beta}\right) \\
&= \delta\left(\frac{t-t_0-t_0\Gamma^2\theta^2}{(1-\beta)(1+(\Gamma\theta)^2)}\right) \\
&= \delta\left(\frac{1/(t_0\Gamma^2)}{1/(t_0\Gamma^2)}\frac{t-t_0-t_0\Gamma^2\theta^2}{(1-\beta)(1+(\Gamma\theta)^2)}\right) \\
&= \delta\left(\frac{(t-t_0)/(t_0\Gamma^2)-\theta^2}{(1/(t_0\Gamma^2))(1-\beta)(1+(\Gamma\theta)^2)}\right) \\
&= \frac{(1-\beta)(1+(\Gamma\theta)^2)}{t_0\Gamma^2}\delta\left(\frac{t-t_0}{t_0\Gamma^2}-\theta^2\right) \\
&= \frac{(1-\beta)(1+(\Gamma\theta)^2)}{t_0\Gamma^2}\delta\left(\theta^2-\frac{t-t_0}{t_0\Gamma^2}\right)
\end{aligned}
\tag{B.16}
$$

We plug this δ-function into Equation B.15, then do some substitutions to make the integral easier.

$$
\begin{aligned}
f_e(t) &= 2\pi\left(\frac{\beta c}{D}\right)^2 t^{2-\alpha}\nu^{-b}\Gamma^{-2-b}\int d\mu(1-\beta\mu)^{\alpha-5-b}j_e(\theta)\delta(t'-t'_0)t'_0 \\
&= 2\pi\left(\frac{\beta c}{D}\right)^2 t^{2-\alpha}\nu^{-b}\Gamma^{-2-b}\int d\cos(\theta)(1-\beta\mu)^{\alpha-5-b}j_e(\theta)\frac{(1-\beta)(1+(\Gamma\theta)^2)}{t_0\Gamma^2}\delta\left(\theta^2-\frac{t-t_0}{t_0\Gamma^2}\right)t'_0 \\
&= 2\pi\left(\frac{\beta c}{D}\right)^2 t^{2-\alpha}\nu^{-b}\Gamma^{-2-b}\int \sin(\theta)d\theta(1-\beta\mu)^{\alpha-5-b}j_e(\theta)\frac{(1-\beta)(1+(\Gamma\theta)^2)}{t_0\Gamma^2}\delta\left(\theta^2-\frac{t-t_0}{t_0\Gamma^2}\right)\frac{t_0}{1-\beta} \\
&= 2\pi\left(\frac{\beta c}{D}\right)^2 t^{2-\alpha}\nu^{-b}\Gamma^{-2-b}\int \theta d\theta((1-\beta)(1+\Gamma^2\theta^2))^{\alpha-5-b}j_e(\theta)\frac{(1+(\Gamma\theta)^2)}{\Gamma^2}\delta\left(\theta^2-\frac{t-t_0}{t_0\Gamma^2}\right) \\
&= 2\pi\left(\frac{\beta c}{D}\right)^2 t^{2-\alpha}\nu^{-b}\Gamma^{-2-b}(1-\beta)^{\alpha-5-b}\int \frac{d(\theta^2)}{2}(1+\Gamma^2\theta^2)^{\alpha-5-b}j_e(\theta)\frac{(1+(\Gamma\theta)^2)}{\Gamma^2}\delta\left(\theta^2-\frac{t-t_0}{t_0\Gamma^2}\right) \\
&= 2\pi\left(\frac{\beta c}{D}\right)^2 t^{2-\alpha}\nu^{-b}\Gamma^{-2-b}(1-\beta)^{\alpha-5-b}\frac{1}{2\Gamma^2}\int d(\theta^2)(1+\Gamma^2\theta^2)^{\alpha-4-b}j_e(\theta)\delta\left(\theta^2-\frac{t-t_0}{t_0\Gamma^2}\right) \\
&= 2\pi\left(\frac{\beta c}{D}\right)^2 t^{2-\alpha}\nu^{-b}\Gamma^{-2-b}(1-\beta)^{\alpha-5-b}\frac{2(1-\beta)}{2}\int d(\theta^2)(1+\Gamma^2\theta^2)^{\alpha-4-b}j_e(\theta)\delta\left(\theta^2-\frac{t-t_0}{t_0\Gamma^2}\right) \\
&= 2\pi\left(\frac{\beta c}{D}\right)^2 t^{2-\alpha}\nu^{-b}\Gamma^{-2-b}(1-\beta)^{\alpha-4-b}\int d(\theta^2)(1+\Gamma^2\theta^2)^{\alpha-4-b}j_e(\theta)\delta\left(\theta^2-\frac{t-t_0}{t_0\Gamma^2}\right)
\end{aligned}
\tag{B.17}
$$

Now we do the integral where the δ-function sets $\theta^2 = \frac{t-t_0}{t_0\Gamma^2}$ and $\theta = \Gamma^{-1}\sqrt{\frac{t-t_0}{t_0}}$

$$\begin{aligned}
f_e(t) &= 2\pi\left(\frac{\beta c}{D}\right)^2 t^{2-\alpha}\nu^{-b}\Gamma^{-2-b}(1-\beta)^{\alpha-4-b}\left(1+\Gamma^2\left(\frac{t-t_0}{t_0\Gamma^2}\right)\right)^{\alpha-4-b} j_e\left(\Gamma^{-1}\sqrt{\frac{t-t_0}{t_0}}\right) \\
&= 2\pi\left(\frac{\beta c}{D}\right)^2 t^{2-\alpha}\nu^{-b}\Gamma^{-2-b}(1-\beta)^{\alpha-4-b}\left(1+\frac{t-t_0}{t_0}\right)^{\alpha-4-b} j_e\left(\Gamma^{-1}\sqrt{\frac{t-t_0}{t_0}}\right) \\
&= 2\pi\left(\frac{\beta c}{D}\right)^2 t^{2-\alpha}\nu^{-b}\Gamma^{-2-b}(1-\beta)^{\alpha-4-b}\left(1+\frac{t}{t_0}\right)^{\alpha-4-b} j_e\left(\Gamma^{-1}\sqrt{\frac{t-t_0}{t_0}}\right) \\
&= 2\pi\left(\frac{\beta c}{D}\right)^2 t^{2-\alpha}\nu^{-b}\Gamma^{-2-b}(1-\beta)^{\alpha-4-b}\left(\frac{t}{t_0}\right)^{\alpha-4-b} j_e\left(\Gamma^{-1}\sqrt{\frac{t-t_0}{t_0}}\right)
\end{aligned} \tag{B.18}$$

Taking the ultra-relativistic limit ($\beta \approx 1$) to ignore any lone β terms leaves

$$f_e(t) = 2\pi\left(\frac{c}{D}\right)^2 t^{2-\alpha}\nu^{-b}\Gamma^{-2-b}(1-\beta)^{\alpha-4-b}\left(\frac{t}{t_0}\right)^{\alpha-4-b} j_e\left(\Gamma^{-1}\sqrt{\frac{t-t_0}{t_0}}\right) \tag{B.19}$$

Comparing the pre-factor, Z, in Equation B.12 and Equation B.19 we see that

$$f_e(t) = nZ\left(\frac{t}{t_0}\right)^{-n} j_e\left(\Gamma^{-1}\sqrt{\frac{t-t_0}{t_0}}\right) \tag{B.20}$$

where $n = 4-\alpha+b$; f_e and f_ν have almost the same pre-factor.

Finally recombining f_ν and f_e we get an extra term in F when $t \geq t_0$;

$$F = 1-(1+(\Gamma\theta_{\text{jet}}/2)^2)^{-n} + n\left(\frac{t}{t_0}\right)^{-n} j_e\left(\Gamma^{-1}\sqrt{\frac{t-t_0}{t_0}}\right) \tag{B.21}$$

The function F is constant (F=1) at early time and then falls like $(\Gamma\theta_{\text{jet}})^2 \sim t^{-3/4}$ at late time. The index $n \approx 4$ affects the sharpness of the break (sharper for larger n). The pre-factor behaves like $t^{2-\alpha}\Gamma^{6-2\alpha+b}\nu^{-b} \approx t^{-1/4-\alpha/4-3b/8}\nu^{-b}$ because $\Gamma \sim t^{-3/8}$. We can see that in the following:

$$
\begin{aligned}
t^2 t^{-\alpha}\Gamma^{6-2\alpha+b} &= t^2 t^{-\alpha}(\Gamma^{6-2\alpha+b})^{-3/8} \\
&= t^2 t^{-\alpha} t^{-9/4+3\alpha/4-3b/8} \\
&= t^{-1/4-\alpha/4-3b/8}
\end{aligned}
\tag{B.22}
$$

Since the flux decays as $t^{-\alpha}\nu^{-b}$, $\alpha = 1/4+\alpha/4+3b/8$ and $n = 5-4\alpha+5b/2$. The indices above and below the cooling break are constrained by closure relations and, in terms of the electron power law index p, $n = 11/2-p/2$ and $n = 7(1-p/4)$ below and above the cooling break, respectively. Hence, for p=2, we expect a slightly sharper break below the cooling break ($n = 4.5$) than above the cooling break ($n = 3.5$).

$$
f_\nu(t) = 2\pi\left(\frac{\beta ct}{D\Gamma}\right)^2 A_0 \int \frac{d\mu t'^{-\alpha}\nu'^{-b}H(\theta_{\mathrm{jet}}/2-\theta)}{(1-\beta\mu)^5}
\tag{B.23}
$$

Replace $H(\theta_/2-\theta)$ with $j_e(\theta)$ and $t'^{-\alpha}$ with $\delta(t'-t'_0)$. We have $\nu' = \nu\Gamma(1-\beta\mu)$, so the integral goes to

$$
\begin{aligned}
f_e(t) &= 2\pi\left(\frac{\beta ct}{D\Gamma}\right)^2 A_0 \int \frac{d\mu\nu^{-b}\Gamma^{-b}(1-\beta\mu)^{-b}j_e(\theta)\delta(t'-t'_0)}{(1-\beta\mu)^5} \\
&= 2\pi\left(\frac{\beta ct}{D}\right)^2 \Gamma^{-2-b}\nu^{-b}A_0 \int d\mu(1-\beta\mu)^{-b-5}j_e(\theta)\delta(t'-t'_0) \\
&= 2\pi\left(\frac{\beta ct}{D}\right)^2 \Gamma^{-2-b}\nu^{-b}(1-\beta)^{-5-b}A_0 \int d\mu(1+(\Gamma\theta)^2)^{-5-b}j_e(\theta)\delta(t'-t'_0)
\end{aligned}
\tag{B.24}
$$

In the last step of the previous equation, we have replaced $(1-\beta\mu) = (1-\beta)(1+(\Gamma\theta)^2)$, which has been previously shown.

Next we will rework the δ such that it contains θ. We will use the following substitutions: $t' = t/(1-\beta\mu)$ and $t'_0 = t_0/(1-\beta)$.

$$
\begin{aligned}
\delta(t'-t'_0) &= \delta\left(\frac{t}{1-\beta\mu} - \frac{t_0}{1-\beta}\right) \\
&= \delta\left(\frac{t}{(1-\beta)(1+(\Gamma\theta)^2)} - \frac{t_0}{1-\beta}\right) \\
&= \delta\left(\frac{t-t_0(1+\Gamma^2\theta^2)}{(1-\beta)(1+(\Gamma\theta)^2)}\right) \\
&= \delta\left(\frac{t-t_0+t_0\Gamma^2\theta^2}{(1-\beta)(1+(\Gamma\theta)^2)}\right) \\
&= \delta\left(\frac{1/(t_0\Gamma^2)}{1/(t_0\Gamma^2)}\frac{t-t_0+t_0\Gamma^2\theta^2}{(1-\beta)(1+(\Gamma\theta)^2)}\right) \\
&= \delta\left(\frac{(t-1)/(t_0\Gamma^2)-\theta^2}{(1/(t_0\Gamma^2))(1-\beta)(1+(\Gamma\theta)^2)}\right) \\
&= \frac{(1-\beta)(1+(\Gamma\theta)^2)}{t_0\Gamma^2}\delta\left(\frac{t-1}{t_0\Gamma^2}-\theta^2\right)
\end{aligned}
\tag{B.25}
$$

Now we will substitute this delta function in for the previous one.

$$
f_e(t) = 2\pi\left(\frac{\beta ct}{D}\right)^2\Gamma^{-2-b}\nu^{-b}(1-\beta)^{-5-b}A_0\int d\mu(1+(\Gamma\theta)^2)^{-5-b}j_e(\theta)\frac{(1-\beta)(1+(\Gamma\theta)^2)}{t_0\Gamma^2}\delta\left(\frac{t-1}{t_0\Gamma^2}-\theta^2\right)
\tag{B.26}
$$

Doing some simplifying:

$$
f_e(t) = 2\pi\left(\frac{\beta ct}{D}\right)^2\Gamma^{-2-b}\nu^{-b}(1-\beta)^{-3-b}\frac{2}{t_0\beta}A_0\int d\mu(1+(\Gamma\theta)^2)^{-4-b}j_e(\theta)\delta\left(\frac{(t-t_0)}{t_0\Gamma^2}-\theta^2\right)
\tag{B.27}
$$

$$
\begin{aligned}
f_e(t) &= 2\pi\left(\frac{\beta c}{D}\right)^2\Gamma^{-2-b}\nu^{-b}(1-\beta)^{-3-b}\frac{2}{t_0\beta}A_0 t\int d\mu(1+(\Gamma\theta)^2)^{-4-b}j_e(\theta)\delta\left(\frac{(t-t_0)}{t_0\Gamma^2}-\theta^2\right) \\
&= 2\pi\left(\frac{\beta c}{D}\right)^2\Gamma^{-2-b}\nu^{-b}(1-\beta)^{-3-b}\frac{2}{t_0\beta}A_0 t_0^2(1+(\Gamma\theta)^2)\int d\mu(1+(\Gamma\theta)^2)^{-4-b}j_e(\theta)\delta\left(\frac{(t-t_0)}{t_0\Gamma^2}-\theta^2\right) \\
&= 2\pi\left(\frac{\beta c}{D}\right)^2\Gamma^{-2-b}\nu^{-b}(1-\beta)^{-3-b}\frac{2}{t_0\beta}t_0^2 A_0\int d\mu(1+(\Gamma\theta)^2)(1+(\Gamma\theta)^2)^{-4-b}j_e(\theta)\delta\left(\frac{(t-t_0)}{t_0\Gamma^2}-\theta^2\right) \\
&= 4\pi\beta\left(\frac{c}{D}\right)^2\Gamma^{-2-b}\nu^{-b}(1-\beta)^{-3-b}t_0 A_0\int d\mu(1+(\Gamma\theta)^2)^{-2-b}j_e(\theta)\delta\left(\frac{(t-t_0)}{t_0\Gamma^2}-\theta^2\right)
\end{aligned}
\tag{B.28}
$$

Now treating the integral separately. The δ makes all the $\theta^2 = \Gamma^{-2}\left(\frac{t-t_0}{t}\right)$ and $\theta = \Gamma^{-1}\sqrt{\frac{t-t_0}{t}}$.

$$\begin{aligned}
&\int d\mu(1+(\Gamma\theta)^2)^{-2-b} j_e(\theta)\delta\left(\frac{(t-t_0)}{t_0\Gamma^2}-\theta^2\right)\\
&=\int d\theta\sin(\theta)(1+(\Gamma\theta)^2)^{-2-b} j_e(\theta)\delta\left(\frac{(t-t_0)}{t_0\Gamma^2}-\theta^2\right)\\
&=\int d\theta\theta(1+(\Gamma\theta)^2)^{-2-b} j_e(\theta)\delta\left(\frac{(t-t_0)}{t_0\Gamma^2}-\theta^2\right)\\
&=\int \frac{d(\theta^2)}{2}(1+(\Gamma\theta)^2)^{-2-b} j_e(\theta)\delta\left(\frac{(t-t_0)}{t_0\Gamma^2}-\theta^2\right)\\
&=\int \frac{d(\theta^2)}{2}(1+(\Gamma\theta)^2)^{-2-b} j_e(\theta)\delta\left(\frac{(t-t_0)}{t_0\Gamma^2}-\theta^2\right)\\
&=\frac{1}{2}\left(1+\Gamma^2\Gamma^{-2}\left(\frac{t-t_0}{t}\right)\right)^{-2-b} j_e\left(\Gamma^{-1}\sqrt{\frac{t-t_0}{t}}\right)\\
&=\frac{1}{2}\left(1+\left(\frac{t-t_0}{t}\right)\right)^{-2-b} j_e\left(\Gamma^{-1}\sqrt{\frac{t-t_0}{t}}\right)\\
&=\frac{1}{2}\left(1+\frac{t}{t_0}-1\right)^{-2-b} j_e\left(\Gamma^{-1}\sqrt{\frac{t-t_0}{t}}\right)\\
&=\frac{1}{2}\left(\frac{t}{t_0}\right)^{-2-b} j_e\left(\Gamma^{-1}\sqrt{\frac{t-t_0}{t}}\right)
\end{aligned} \tag{B.29}$$

Now we plug that answer in for the integral. And do a little more simplifying

$$\begin{aligned}
f_e(t) &= 4\pi\beta\left(\frac{c}{D}\right)^2\Gamma^{-2-b}\nu^{-b}(1-\beta)^{-3-b}t_0A_0\frac{1}{2}\left(\frac{t}{t_0}\right)^{-2-b} j_e\left(\Gamma^{-1}\sqrt{\frac{t-t_0}{t}}\right)\\
f_e(t) &= 2\pi\beta\left(\frac{c}{D}\right)^2\Gamma^{-3-b}\nu^{-b}(1-\beta)^{-3-b}t_0A_0\left(\frac{t}{t_0}\right)^{-2-b} j_e\left(\Gamma^{-1}\sqrt{\frac{t-t_0}{t_0}}\right)
\end{aligned} \tag{B.30}$$

APPENDIX C

DATA FOR RATIR GRB FOLLOW-UP

Table 5. Data for RATIR GRB follow-ups.

Burst	Exp. Time [hours]		Time After GRB [hours]		r	i	Z	Y	J	H
	ri	$ZYJH$	Start	Stop						
GRB121209A	1.0	1.0	3.72	-	>21.7	>22.1	>20.5	>20.0	>19.8	>19.5
GRB121211A	1.8	0.67	21.8	24.1	22.9±0.2	23.2±0.2	22.1±0.4	>21.3	>21.9	>21.1
GRB130122A	0.75	0.75	7.6	12.7	>20.7	21.1±0.2	>20.3	>20.2	>18.2	-
GRB130131A	2.83	1.07	16.0	20.0	>23.8	>23.3	>22.2	>21.8	>21.9	>21.5
GRB130131B	1.96	0.73	14.86	17.70	>23.8	>23.1	>22.1	>21.7	>21.8	>21.4
GRB130215A*	0.42	0.32	1.58	2.88	17.86±0.05	17.10±0.04	-	16.86±0.04	16.67±0.04	-
GRB130305A	0.31	-	15.11	15.50	>23.4	>23.1	-	-	-	-
GRB130310A†	-	-	31.44	35.28	23.6±0.1	23.6±0.2	$\gtrsim$22	$\gtrsim$22	$\gtrsim$22	$\gtrsim$22
GRB130313A	3.5	1.5	14.96	20.25	>23.6	>23.3	>22.3	>22.0	>21.8	>21.3
GRB130327A*	0.82	0.35	1.16	2.17	21.22±0.10	21.17±0.09	20.09±0.14	19.98±0.17	19.98±0.23	>20.08
GRB130418A*	1.07	0.45	8.24	9.54	18.87±0.02	18.77±0.02	18.30±0.02	18.07±0.02	18.06±0.02	17.53±0.02
GRB130420A*	0.36	0.14	2.48	3.38	19.81±0.02	19.41±0.02	19.37±0.06	18.89±0.07	19.16±0.07	18.87±0.11
GRB130420B	1.32	0.55	14.54	18.10	>23.19	22.99	21.87	21.39	21.20	20.53
GRB130427A*	1.07	0.45	0.25	1.67	-	14.46±0.01	14.13±0.03	14.02±0.03	14.05±0.02	13.77±0.03
GRB130427B	0.71	0.29	21.26	22.19	>22.08	>22.06	>21.28	>20.77	>20.57	>19.84
GRB130502A	0.71	0.30	9.48	10.34	>22.82	>22.66	>21.65	>21.45	>21.16	>20.99
GRB130505A	0.36	0.14	42.84	44.87	21.20±0.27	20.98±0.23	>21.17	>19.15	>18.38	>17.15
GRB130508A	1.42	0.60	15.45	17.54	>23.81	>23.53	>21.95	>21.66	>21.00	>20.42
GRB130513A	0.18	0.07	19.97	20.30	>22.64	>22.65	>21.34	>20.65	>20.26	>19.71
GRB130514A	2.49	1.04	0.08	3.90	>23.51	>23.39	>22.07	>21.62	>21.43	>21.13
GRB130514B	0.20	0.08	14.12	14.55	>22.49	>21.95	>20.53	>20.54	>19.66	>19.72

continued on next page

Burst	Exp. Time [hours]		Time After GRB [hours]		r	i	Z	Y	J	H
	ri	$ZYJH$	Start	Stop						
GRB130518A*	0.64	0.27	20.54	21.49	19.38±0.02	19.10±0.02	18.83±0.04	18.65±0.04	18.28±0.07	18.47±0.11
GRB130527A	1.97	0.73	18.13	20.91	>21.9	>22.3	>20.7	>20.6	>20.6	>20.3
GRB130603B	1.93	0.81	12.0	14.78	20.78±0.03	20.52±0.03	20.20±0.05	19.94±0.05	19.97±0.06	19.55±0.06
GRB130606A*	0.36	0.15	7.38	7.79	>23.02	21.16±0.06	18.79±0.03	18.40±0.03	18.31±0.03	17.92±0.03
GRB130606B	0.36	0.30	15.97	18.08	>23.59	>23.61	-	>21.52	-	>20.73
GRB130608A	0.20	0.08	11.70	12.00	>21.90	>22.27	>21.21	>20.64	>20.12	>19.80
GRB130609A	1.24	0.60	0.56	2.52	>23.34	>23.27	>22.39	>21.91	>21.72	>21.06
GRB130612A	0.71	-	0.41	1.31	21.23±0.07	21.05±0.06	-	-	-	-
GRB130626A†	0.02	-	0.06	-	18.69±0.07	17.40±0.05	-	-	-	-
GRB130702A*	1.42	0.60	51.79	53.82	19.22±0.01	19.06±0.02	18.85±0.03	18.70±0.03	18.72±0.03	18.56±0.03
GRB130722A	2.33	-	21.24	25.00	>19.58±0.02	-	-	-	-	-
GRB130803A	1.53	0.63	17.51	19.98	>23.29	>23.34	>22.27	>21.70	>20.90	>20.24
GRB130831A*	5.16	2.09	14.65	22.73	20.64±0.03	20.38±0.03	20.20±0.07	19.69±0.07	19.87±0.09	19.88±0.14
GRB130907A*	0.36	0.15	5.57	6.03	20.01±0.03	19.30±0.02	18.78±0.05	18.48±0.06	18.13±0.06	17.63±0.05
GRB130912A	5.33	2.24	22.58	27.11	>23.89	>23.79	>22.86	>22.38	>22.30	>21.78
GRB130925A*	0.36	0.15	2.30	7.81	22.26±0.11	21.75±0.10	20.25±0.06	20.77±0.14	19.98±0.07	19.85±0.12
GRB131004A	2.17	0.94	5.12	9.44	>23.91	>23.33	>22.56	>21.86	>21.81	>21.26
GRB131014A*†	1.19	1.09	27.45	31.41	23.42±0.21	22.76±0.17	23.1±0.4	21.20±0.27	21.9±0.6	21.8±0.7
GRB131018A	2.58	1.09	19.36	23.83	>23.30	>23.18	>22.43	>22.05	>21.70	>21.27
GRB131018B*	2.8	1.3	33.94	38.36	-	-	>22.6	-	>21.6	-
GRB131024B	1.78	0.74	12.28	14.87	>23.68	>23.35	>22.44	>22.01	>21.75	>21.49
GRB131030A*	4.26	1.69	4.91	11.97	19.14±0.01	18.92±0.01	18.76±0.02	18.61±0.02	18.62±0.02	18.40±0.02

continued on next page

Burst	Exp. Time [hours]		Time After GRB [hours]		r	i	Z	Y	J	H
	ri	$ZYJH$	Start	Stop						
GRB131031A*	4.47	1.81	17.44	23.99	22.38±0.07	22.34±0.09	21.89±0.14	>21.81	>21.36	>20.69
GRB131108A*	2.11	0.76	13.06	16.11	19.91±0.02	19.70±0.02	19.57±0.04	19.23±0.05	19.34±0.07	19.09±0.08
GRB131127A*	2.49	1.04	16.42	19.94	>24.19	>23.53	>22.78	>22.16	>22.04	>21.48
GRB131202A	1.04	0.44	10.81	12.32	>22.99	>22.56	>21.50	>20.68	>20.43	>20.05
GRB140114A*	0.98	0.43	0.16	1.51	21.92±0.10	21.21±0.07	21.14±0.12	20.75±0.15	20.56±0.12	20.28±0.15
GRB140118A	0.13	0.07	0.66	0.89	>19.93	>19.37	>19.06	>18.99	>18.32	-
GRB140129A*	0.21	0.21	0	0.21	18.05±0.01	17.85±0.02	17.72±0.03	17.82±0.04	17.65±0.05	17.68±0.07
GRB140215A*	0.36	0.15	0.65	1.13	17.45±0.01	17.08±0.01	16.82±0.01	16.55±0.02	16.34±0.01	16.05±0.01
GRB140226A* iPTF14yb	3.91	1.64	20.53	26.68	22.28±0.09	22.02±0.09	21.98±0.24	22.12±0.35	21.88±0.35	>21.59
GRB140304A*	0.26(r) 0.53(i)	0.3	13.50	14.40	21.78±0.13	20.66±0.06	19.45±0.05	19.19±0.06	19.11±0.07	18.71±0.08
GRB140311A	2.10	0.89	8.75	11.51	22.33±0.13	21.56±0.08	20.58±0.08	20.09±0.08	-	-
GRB140311B	2.84	1.19	11.52	15.25	>23.99	>23.82	>22.85	>22.26	-	-
GRB140318A*	0.99	0.60	3.36	7.40	21.88±0.33	21.37±0.18	20.67±0.20	20.76±0.29	20.60±0.21	20.29±0.19
GRB140320A	1.40	0.56	31.77	33.94	>22.70	>22.38	>21.23	>21.27	>20.81	>20.24
GRB140331A*	1.04	0.44	0.35	1.87	22.02±0.11	20.79±0.04	20.14±0.06	19.81±0.07	19.75±0.08	19.76±0.12
GRB140408A	1.42	-	20.52	22.37	>22.84	22.53	-	-	-	-
GRB140419A*	0.36	0.15	0.15	0.67	16.22±0.01	15.81±0.01	15.66±0.01	15.46±0.02	15.31±0.01	15.26±0.02
GRB140423A*	2.56	1.07	22.48	27.13	21.90±0.08	21.79±0.07	21.65±0.19	21.39±0.17	20.98±0.20	21.33±0.26
GRB140508A*	4.27	1.79	25.61	32.04	19.65±0.02	19.52±0.02	19.36±0.03	19.20±0.03	19.18±0.03	18.98±0.03
GRB140516A	2.13	0.89	11.41	14.56	>23.57	>23.39	>21.70	>21.52	>22.00	>21.48
GRB140518A*	1.75	0.71	0.60	1.75	20.50±0.04	19.00±0.02	18.59±0.03	18.19±0.03	18.13±0.02	17.80±0.02
GRB140610A	0.16	0.07	12.06	12.26	>20.22	>19.15	>16.99	>17.40	>16.68	>17.62

continued on next page

Burst	Exp. Time [hours]		Time After GRB [hours]		r	i	Z	Y	J	H
	ri	$ZYJH$	Start	Stop						
GRB140614B	0.71	0.30	0.11	4.62	>22.70	>22.53	>21.64	>21.08	>21.04	>20.51
GRB140622A	1.20	0.51	0.02	1.70	>23.64	>23.49	>19.41	>18.73	-	-
GRB140703A	0.71	0.29	9.74	10.68	20.32±0.03	19.72±0.03	18.53±0.05	18.31±0.05	19.60±0.17	18.98±0.09
GRB140709A*	4.98	2.09	2.76	9.93	24.28±0.45	23.05±0.16	>22.92	>22.40	>22.30	>21.94
GRB140710A	0.71	0.31	0.06	1.12	21.36±0.08	21.20±0.07	20.77±0.14	20.42±0.16	20.31±0.14	19.75±0.13
GRB141004A*	1.07	-	7.82	9.15	22.35±0.13	22.11±0.12	-	-	-	-
GRB141005A	1.07	-	0.05	1.34						
GRB141015A	2.44	-	0.05	3.59	>23.07	>22.48	-	-	-	-
GRB141026A*	2.49	2.49	0.54	3.58	21.74±0.07	21.54±0.06	>20.5	-	-	-
GRB141028A*	1.07	1.07	13.62	14.82	20.09±0.02	19.85±0.02	19.50±0.10	-	-	-
GRB141031B	0.36	0.36	11.34	11.75	>22.98	>22.81	>19.91	-	-	-
GRB141121A*	3.78	3.78	4.00	8.84	19.62±0.02	19.45±0.02	19.76±0.12	-	-	-
GRB150120B	3.91	3.91	18.73	23.64	23.4±0.2	22.6±0.1	>20.72	-	-	-
GRB150203A	1.28	1.28	0.50	2.14	>23.1	>23.3	>20.1	-	-	-
GRB150211A	1.07	1.07	0.05	1.29	>23.34	>23.71	>20.21	-	-	-
GRB150212A	0.89	0.89	1.29	2.31	>23.1	>23.3	>19.6	-	-	-
GRB150213B	2.58	2.58	11.27	14.27	22.4±0.6	22.1±0.1	>20.50	-	-	-
GRB150317A	3.0	3.0	0.05	5.9	20.5±0.1	21.5±0.1	>20.8	-	-	-
GRB150323A	0.71	-	0.16	0.98	21.16±0.11	20.39±0.05	>19.30	-	-	-
GRB150323C	2.49	2.49	10.20	13.42	23.00±0.15	22.63±0.11	>20.60	-	-	-
GRB150402A	3.16	-	26.39	34.29	>22.75	>22.68	-	-	-	-
GRB150423A*	1.42	1.42	3.30	5.01	23.77±0.23	23.62±0.26	>20.33	-	-	-

continued on next page

Burst	Exp. Time [hours]		Time After GRB [hours]		r	i	Z	Y	J	H
	ri	$ZYJH$	Start	Stop						
GRB150424A	2.4	2.4	19.54	23.05	21.92±0.11	21.65±0.09	>20.17	-	-	-
GRB150428A	2.49	2.49	1.80	4.88	>23.94	>23.90	>19.56	-	-	-
GRB150518A*	1.78	1.78	29.94	32.08	21.26±0.04	21.04±0.04	>20.08	-	-	-
GRB150527A*†	0.58	0.58	0.22	0.91	21.17±0.10	20.83±0.14	>19.50	-	-	-
GRB150530A	2.49	2.49	20.08	23.21	>24.42	>24.18	>20.44	-	-	-
GRB150710A	0.71	0.71	3.47	4.31	>23.4	>23.2	>19.4	-	-	-
GRB150716A†	2.21	-	0.06	3.61	20.34±0.02	19.23±0.02	-	-	-	-
GRB150724B*	2.39	-	36.02	40.86	23.24±0.34	22.39±0.15	-	-	-	-
GRB150727A*	1.07	1.07	8.65	9.95	21.13±0.19	21.40±0.13	>19.57	-	-	-
GRB150728A*†	5.29	5.29	15.73	22.75	21.37±0.04	20.89±0.04	19.54±0.13	-	-	-
GRB150811A*	0.36	0.36	0.04	0.47	17.51±0.01	17.22±0.01	16.76±0.04	-	-	-
GRB150817A*	2.13	2.13	1.29	3.93	22.06±0.09	21.49±0.07	>20.33	-	-	-
GRB150819A	2.80	-	7.08	10.60	>23.60	>23.91	-	-	-	-
GRB150910A*†	0.99	0.99	66.44	69.21	22.44±0.13	22.31±0.11	>20.29	-	-	-
GRB151022A	0.36	0.36	13.77	14.17	>23.11	>23.04	>19.84	-	-	-
GRB151023A	1.07	1.07	12.35	13.66	20.27±0.04	19.10±0.02	18.29±0.09	-	-	-
LIGO/Virgo G194575*	Observed 26 galaxies in LIGO/Virgo 1-σ confidence interval with 0.13 hours of exposure per field no detections reported, reaching typical depths of r and i = 21 mag, and z = 17 mag (10-sigma)									
GRB151027B*	3.51	3.51	7.46	13.55	20.83±0.05	20.18±0.04	19.49±0.21	-	-	-
GRB160117B*	2.76	2.76	38.57	42.63	22.30±0.11	21.96±0.08	>19.97	-	-	-
GRB160119A	3.20	3.20	5.61	9.76	23.78±0.28	23.26±0.17	>20.78	-	-	-
GRB160121A*	2.92	2.92	13.28	17.14	21.73±0.13	21.10±0.08	>19.80	-	-	-

continued on next page

Burst	Exp. Time [hours]		Time After GRB [hours]		r	i	Z	Y	J	H
	ri	$ZYJH$	Start	Stop						
GRB160127A*	2.68	2.68	0.73	4.43	20.64±0.03	220.66±0.03	20.14±0.32	-	-	-
GRB160131A*	0.18	0.18	0.07	0.50	13.35±0.04	13.01±0.02	12.67±0.04	-	-	-
GRB160203A*	3.27	3.27	30.42	34.94	23.35±0.21	22.90±0.13	>20.55	-	-	-
GRB160223A*	5.04	2.26	3.65	11.79	18.13±0.01	17.43±0.01	17.37±0.01	17.20±0.01	17.08±0.01	16.81±0.01
GRB160225A*	6.38	2.68	12.72	21.97	23.84±0.18	23.13±0.11	22.71±0.18	22.40±0.22	±22.44±0.26	22.04±0.26
GRB160228A	4.27	1.79	9.23	15.50	>24.46	>24.39	>23.21	>22.76	>22.43	>22.10
GRB160303A*	1.02	0.44	0.03	1.50	22.95±0.31	22.65±0.23	>21.98	21.83±0.36	>21.30	>21.01
GRB160310A	1.78	0.75	27.46	31.25	22.48±0.09	21.82±0.05	-	-	20.62±0.10	20.03±0.08
GRB160313A	1.42	0.52	0.63	2.67	>23.49	>23.21	>22.08	>21.48	>20.11	>20.60
GRB160314A*	3.56	1.49	15.59	21.16	22.83±0.10	22.37±0.06	22.27±0.15	22.40±0.21	21.93±0.19	>22.38
GRB160321A	2.47	0.82	11.32	15.08	>23.84	22.32±0.11	22.49±0.34	>22.19	>21.53	>21.27
GRB160327A*	0.36	0.15	0.06	0.58	21.78±0.13	19.68±0.02	18.55±0.02	17.75±0.01	17.56±0.01	16.74±0.01
GRB160501A	1.73	0.66	7.23	10.70	>22.94	>22.76	>21.69	>21.22	>20.81	>19.90
GRB160504A	2.49	1.04	19.64	23.11	>23.70	23.62±0.36	>22.38	>22.08	>21.73	>21.35
GRB160623A	0.56	0.23	29.48	30.31	21.12±0.05	19.77±0.02	18.73±0.02	18.41±0.02	17.46±0.01	16.93±0.01
GRB160625B*	0.36	0.15	8.53	9.02	18.28±0.01	18.08±0.01	17.95±0.01	17.78±0.01	17.77±0.02	17.65±0.02
GRB160705B	0.66	0.30	7.04	8.05	22.89±0.15	22.12±0.09	22.34±0.33	21.73±0.32	>21.54	20.98±0.34
GRB160712A	3.56	1.45	9.05	14.30	22.77±0.08	21.55±0.03	20.93±0.05	20.44±0.05	20.27±0.06	20.15±0.08
GRB160804A	1.78	0.75	26.33	29.04	21.29±0.02	20.90±0.02	21.12±0.19	21.04±0.29	20.52±0.23	>20.51
GRB160816A*	0.71	0.30	12.8	14.2	21.05±0.05	20.79±0.04	20.61±0.07	20.32±0.08	20.16±0.09	19.95±0.10
GRB160912A	1.76	0.74	11.20	13.52	23.05±0.10	22.73±0.13	22.62±0.31	22.13±0.29	>21.91	>21.72
GRB160917A	3.72	1.63	15.39	21.08	>24.31	>24.28	>23.20	>22.90	>22.57	>22.20

continued on next page

Burst	Exp. Time [hours]		Time After GRB [hours]		r	i	Z	Y	J	H
	ri	$ZYJH$	Start	Stop						
GRB161004A	1.73	0.65	13.49	16.23	>23.3	>23.2	>22.4	>21.8	>21.3	>19.4
GRB161011A	0.69	0.27	44.66	45.69	>23.4	>22.7	>21.7	>21.4	>21.0	>20.7
GRB161014A*	2.72	1.22	16.17	20.80	22.89±0.12	22.24±0.10	22.01±0.15	>21.60	22.19±0.15	>20.48
GRB161022A	2.49	1.04	6.23	9.89	>24.24	>24.04	>22.96	>22.50	>22.18	>21.87
GRB161108A	1.03	0.40	7.87	9.34	21.97±0.12	21.36±0.06	20.88±0.11	20.57±0.14	20.05±0.27	>18.12
GRB161113A	0.71	0.14	17.94	19.01	>22.41	>22.18	>21.21	>20.72	-	>18.83
GRB161202A	3.34	1.45	26.70	32.11	>24.0	>23.9	>23.1	>22.8	>22.4	>22.0
GRB161214B	0.26	0.15	8.60	9.05	18.87±0.01	18.56±0.01	18.34±0.01	18.23±0.03	18.23±0.03	18.05±
GRB170112A	0.76	0.32	1.58	2.95	$\gtrsim$19	$\gtrsim$19	$\gtrsim$19	$\gtrsim$19	$\gtrsim$19	$\gtrsim$19
LIGO/Virgo G268556	Observed several candidate galaxies in LIGO/Virgo 1-σ confidence interval. GRB not detected; see Table 6 for data.									
GRB170202A	3.98	1.68	9.92	19.17	20.68±0.01	20.83±0.02	20.84±0.07	20.50±0.06	-	-
GRB170205A	0.61	0.29	0.04	1.25	18.31±0.01	17.90±0.01	18.06±0.01	19.26±0.07	-	-
GRB170208B	6.02	2.52	3.98	12.65	>23.56	>23.43	>22.64	>22.55	-	-
GRB170214A*	0.40	0.32	10.58	11.99	21.06±0.11	20.89±0.13	20.54±0.18	20.34±0.32	-	-
GRB170317A*	2.84	1.19	17.37	21.38	22.85±0.05	22.86±0.09	22.92±0.30	22.34±0.26	22.41±0.35	>21.95
GRB170318A	0.24	0.11	0.05	0.46	>23.39	>22.82	>21.72	>21.56	>21.12	>20.73
GRB170318B	0.71	0.30	19.76	20.76	>25.64	>24.39	>22.65	>22.43	>21.38	>20.98
GRB170405A	3.84	1.62	10.93	16.85	22.67±0.05	21.83±0.04	21.26±0.07	21.14±0.07	20.75±0.07	20.56±0.08
GRB Swift Trigger 748858	2.49	1.04	0.04	4.10	>24.41	>23.95	>22.59	>22.44	>22.03	>21.79
GRB170428A	0.90	0.35	24.69	26.25	>22.3	22.1±0.4	>20.9	>20.6	>20.1	>19.9
GRB170519A*	1.41	0.60	0.03	2.44	16.72±0.01	16.50±0.01	16.34±0.01	16.25±0.01	16.15±0.01	15.87±0.01

continued on next page

Burst	Exp. Time [hours]		Time After GRB [hours]		r	i	Z	Y	J	H
	ri	$ZYJH$	Start	Stop						
GRB170524A*	1.06	0.36	13.79	15.29	>24.45	>23.25	>21.72	>21.26	>18.16	>17.83
GRB170604A	0.84	0.42	14.19	15.70	20.42±0.06	20.65±0.07	20.45±0.13	20.40±0.30	-	-
GRB170705A*	1.42	0.59	1.34	3.41	18.60±0.01	18.30±0.01	18.03±0.01	17.79±0.01	17.79±0.01	17.56±0.01
GRB170711A	0.33	0.14	12.68	13.13	>22.94	>22.86>	>21.61	>21.45	>21.08	>20.83
GRB170813A	0.36	0.15	2.48	3.06	>22.46	>22.08	>20.23	>19.82	>19.38	>19.13
GRB170822A	0.69	0.30	25.45	26.38	>23.37	>22.87	>21.99	>21.56	>21.28	>20.82
GRB170921A	5.29	2.22	13.82	21.76	24.45±0.34	24.38±0.34	>23.05	>22.83	>22.47	>22.19
GRB171001A	5.31	2.24	9.63	17.69	>24.15	>23.98	>22.96	>22.77	>22.43	>22.03
GRB171004A	1.07	0.45	2.97	4.45	21.91±0.11	21.32±0.07	21.13±0.15	20.43±0.12	20.45±0.15	19.98±0.13
GRB171007A	0.31	0.14	0.05	0.57	>22.05	>21.94	>21.24	>21.02	>20.65	>20.34
GRB171010A	2.72	1.13	60.79	65.05	19.88±0.02	19.59±0.02	19.25±0.02	19.19±0.02	18.97±0.03	18.80±0.03
GRB171020A*	5.30	2.20	4.60	12.98	22.91±0.12	22.76±0.11	>21.44	21.72±0.35	21.54±0.23	21.69±0.35
GRB171027A*	0.36	0.15	0.04	0.51	>23.17	>23.12	>20.66	>21.09	20.95±0.26	19.12±0.06
GRB171102B	0.98	0.42	11.99	13.55	>22.51	>22.59	>21.14	>21.53	>21.36	>20.97
GRB171115A	1.07	0.38	7.14	8.66	>23.05	>23.19	>21.86	>21.66	>21.13	>20.71
GRB171123A	1.07	0.45	21.06	22.77	>23.60	>23.39	>22.23	>21.69	>21.43	>21.02
GRB171205A	1.44	0.71	2.15	5.36	18.30±0.05	18.13±0.02	18.35±0.05	18.13±0.05	-	-
GRB180111A	5.31	2.22	12.35	20.68	20.90±0.10	20.41±0.10	20.61±0.15	20.41±0.15	-	-
GRB180224A†	3.91	-	7.24	14.42	22.94±0.13	22.08±0.06	-	-	-	-
GRB180305A*	1.36	-	17.28	19.45	21.95±0.12	21.48±0.08	-	-	-	-
GRB180314B	1.07	-	12.55	13.99	>23.29	>22.90	-	-	-	-
GRB180316A*	2.29	-	4.34	7.49	20.07±0.02	19.87±0.02	-	-	-	-

continued on next page

Burst	Exp. Time [hours]		Time After GRB [hours]		r	i	Z	Y	J	H
	ri	$ZYJH$	Start	Stop						
GRB180324A	0.66	-	0.04	0.96	>22.08	>22.04	-	-	-	-
GRB180325A	1.47	-	1.02	3.67	19.79±0.02	19.38±0.01	-	-	-	-
GRB180329B	0.96	-	12.92	14.22	20.29±0.09	20.32±0.10	-	-	-	-
GRB180402A	1.76	-	0.03	2.33	>23.3	>23.3	-	-	-	-
GRB180410A	2.13	-	19.10	21.87	>24.20	>23.90	-	-	-	-
GRB180418A*	2.57	-	0.03	3.64	19.95±0.01	-	-	-	-	-
GRB180512A	5.22	-	5.75	12.58	>24.30	>24.23	-	-	-	-
GRB180620A	0.36	-	0.03	0.47	18.01±0.01	17.71±0.01	-	-	-	-
GRB180624A	3.91	-	16.42	21.45	21.03±0.02	20.45±0.01	-	-	-	-
GRB180626A*	0.36	-	1.61	2.06	21.57±0.22	20.91±0.13	-	-	-	-
GRB180705A	1.74	-	12.19	14.82	>23.20	>23.07	-	-	-	-
GRB180806A	0.71	-	12.69	13.71	20.21±0.02	19.92±0.01	-	-	-	-
GRB180809B	1.42	-	8.2	10.6	>23.6	>23.5	-	-	-	-
GRB180823A	0.40	0.29	8.40	9.45	>22.20	>22.05	>20.84	>19.72	>20.45	>19.12
GRB180828A	1.73	0.79	8.29	11.70	-	-	-	-	>21.4	20.8±0.3
GRB180904A	2.91	1.33	5.66	10.26	22.61±0.08	22.06±0.05	22.13±0.16	21.64±0.18	21.72±0.21	>21.86
GRB180905A	1.17	0.57	20.07	22.23	>23.26	>23.10	>22.21	>22.06	>21.60	>21.25
GRB180914A	3.00	1.24	18.54	23.57	>24.2	>24.1	>22.7	>22.5	>22.0	>21.6
GRB180914B*	0.36	0.15	32.90	33.43	19.51±0.01	19.20±0.01	18.93±0.03	18.75±0.03	18.60±0.05	18.28±0.04
GRB181003A	1.41	0.58	26.59	29.89	>23.40	>23.15	>22.01	>21.53	>21.19	>20.73
GRB181010A	0.50	0.24	0.07	1.10	20.30±0.20	21.03±0.10	20.67±0.24	20.24±0.21	19.87±0.24	19.16±0.17

RATIR data for all GRB follow-ups during its operation. The first AB magnitude detected (and uncertainty) or upper limits (3σ unless otherwise stated) obtained for each event is provided (* denotes bursts with additional GCN postings and data, † indicates dubious detections, e.g., a non-fading source in the search region). Magnitudes are not corrected for galactic extinction.

APPENDIX D

RATIR FOLLOW-UP OF GRAVITATIONAL WAVE TRIGGERS

Table 6. RATIR Gravitational Wave Follow-Up for aLIGO/Virgo Trigger G268556

Target Galaxy	Exp. Time [hours]		r	i	Z	Y
	ri	*ZY*				
iPTF17ce	0.36	0.07	19.84±0.04	18.92±0.02	18.37±0.02	18.35±0.03
iPTF17ck	0.71	0.15	18.17±0.01	17.59±0.01	17.63±0.01	17.33±0.01
iPTF17dz	0.51	0.22	-	19.09±0.01	19.30±0.03	19.23±0.04
iPTF17ef	1.07	0.22	19.18±0.02	18.92±0.02	18.86±0.03	18.59±0.02
iPTF17ei	1.38	0.29	16.77±0.01	16.37±0.01	16.17±0.01	15.97±0.01

Potential host galaxies for the gravitational wave source aLIGO/Virgo Trigger G268556 were studied using RATIR. Here listed are the exposure time and magnitudes for those galaxies; no new sources were detected in these galaxies over the course of several nights of observation. The magnitudes listed are in AB and are not corrected for galactic extinction.

APPENDIX E

CO-AUTHORS PERMISSION STATEMENT

Permission to use the published works in Chapter 2 (Strausbaugh, Jackson, and Butler 2018) and Chapter 3 (Strausbaugh et al. 2019) as part of this thesis was granted by all co-authors.